Unsteady characteristics of three-dimensional turbulent flow with separation in an asymmetric diffuser

by

Mohammad Mahdi Elyasi

A thesis submitted in partial fulfillment of the requirements for the degree of

Master of Science

Department of Mechanical Engineering
University of Alberta

Abstract

A great number of studies have been undertaken to understand separated turbulent boundary layers (TBLs) due to its importance in the performance, design and control of many engineering systems (Hal 2000). Flow separation has a complicated three-dimensional nature in many flow configurations including wings, flow intakes and swept edges emanating from an apex (Simpson 1981). The three-dimensional nature of flow separation adds to its more complexity (Simpson et al. 1977), and its complicated nature remains unknown (Tobak and Peake 1982; Délery et al. 2001).

In this study, a TBL is subjected to adverse pressure gradient (APG) by an increase in the cross section area of the flow in a diffuser-like section, although the upstream flow is not fully developed. The free-stream velocity drops from 0.45 m/s upstream of the diffuser section to 0.36 m/s at the downstream region. The TBL separates from the diverging wall of the diffuser. Advanced particle image velocimetry (PIV) techniques are applied to provide new insight into statistical understanding and turbulent structures involved in turbulent flow separation. The velocity fields captured by multiple planar PIV cameras are stitched together to provide a large field of view (FOV) with high dynamic rang. Tomographic PIV (Tomo-PIV) provides three-dimensional velocity fields at the location of flow detachment in a small volume near the wall to reveal the three-dimensional characteristics of the flow. The three-dimensional average flow field shows a vortex structure with the rotation axis of the wall-normal direction.

All Reynolds stresses show a similar pattern in the FOV of planar PIV, and they are almost consistent with the distributions provided in the previous research literature on two-dimensional flow separation. The presence of attached or separated flow is characterized by monitoring the direction of streamwise velocity close to the wall. The structure of the instantaneous flow fields that contain a coherent recirculation region is characterized using conditional averaging. For

these flow fields, a region with strong forward streamwise fluctuation appears upstream of the detachment line. Quadrant analysis also shows the frequent occurrence of strong positive streamwise fluctuations upstream of flow detachments. The turbulent statistics of the conditionally selected flow fields reveal a low turbulence region appeared at the detachment point and a strong turbulence at the upstream of flow detachments.

Proper orthogonal decomposition (POD) technique was used to identify the flow motions with large turbulent kinetic energy. The energetic POD modes represent the movement of the shear layer (breathing motion) and the strength of velocity gradient of the shear layer (the strength of vortex shedding) as the motions with large kinetic energy in the flow. The three-dimensional POD analysis reveals also other high energy three-dimensional structures, including vortices with wall-normal axis of rotation (similar to the mean flow structure) and saddle-point structures. Similarities between POD modes and flow structures captured by conditionally averaging analysis are found, which associates these dominant flow motions with the structure of flow detachment. Reconstructed flow fields using the first four POD modes visualize the flow development at the instant of single-detachment flow fields, which illustrates the movement of the center of a large vortex with wall-normal axis from the downstream to the upstream of the FOV. This dislocation of the vortex supplies strong forward and backward motion before and after the instant of flow separation.

Preface

This research study is performed under the supervision of Dr. Sina Ghaemi from the department of Mechanical Engineering at University of Alberta.

The experimental setup described in chapter 3 in addition to the measurements, the analyses and discussions presented in this thesis were developed by the author under supervision of Dr. Sina Ghaemi.

Acknowledgement

I would like to express my gratitude to my supervisor, Dr. Sina Ghaemi, for his support and guidance during this study.

I would like to thank my research group members including Sen Wang, Sina Rafati, Babak Vajdi, Wagih Abu Rowin, Sadek Shaban, Masoud Ebrahimian, Mohammad Mohammadtabar, Farzad Ahmadi Jokani, Drew Gingras, Bradley Gibeau, Felix Weis, Rafat Jami, Desiree Reholon Inojosa, David Serrano, Daren Wilkinson and many others for their great help and kindness.

Finally, I express my great appreciation for my parents for their constant care and consideration.

Table of Contents

Abstract ii
Preface iv
Acknowledgement v
Table of Contents vi
List of Figures viii
List of Tables xviii
Chapter 1 Introduction 1
Chapter 2 Literature review 6
2.1 Turbulent separated flow 6
2.2 Governing equations 8
2.3 Mean velocity profile 10
2.4 Curvature effects 12
2.5 Turbulent statistics 13
2.6 Turbulent structures 15
2.6.1 Coherent structures in adverse-pressure-gradient 15
2.6.2 Unsteady structures of flow separation 16
2.6.3 Large motions of the separated flow 17
2.6.4 Three-dimensional flow separation 18
2.7 Methods of investigation of unsteady turbulent structures 19
2.8 Conclusion 20
Chapter 3 Experimental Setup 21
3.1 Flow Facility 21
3.2 Planar PIV setup 24
3.2.1 Measurement uncertainties 29
3.3 Tomographic PIV setup 34
3.3.1 Measurement uncertainties 36
3.4 Conclusion 38
Chapter 4 Data analysis 39
4.1 Vector Stitching Procedure 39
4.1.1 Image Correction using Target Images 39
4.1.2 Velocity field stitching 42
4.1.3 Validation of stitching and errors 49

4.2 Conditional averaging 54
4.2.1 Mathematical description 54
4.2.2 Categorizing vector fields based on detachment status 57
4.3 The Proper Orthogonal Decomposition 60
4.3 Conclusion.. 61
Chapter 5 Planar field 62
5.1 Mean flow field 62
5.1.1 Mean velocity field 62
5.1.2 Reynolds stresses 66
5.1.3 Third-order moments 67
5.1.4 Turbulence production 70
5.2 Coherent structures at the separation instants 72
5.2.1 Instantaneous flow fields with strong single-detachments 72
5.3 Quadrant analysis 78
5.4 Proper orthogonal decomposition analysis 87
5.5 Conclusion.. 92
Chapter 6 Three-dimensional flow field 93
6.1 Mean flow field 93
6.2 Three-dimensional characterization of structures at separation instants 97
6.2.1 Single-detachment vector fields 97
6.2.2 Flow fields captured at $t_0-\Delta t$ 101
6.2.3 Flow field captured at $(t_0 - 2\Delta t)$ 106
6.3 POD results 111
6.4 Reconstruction based on conditionally averaged POD coefficients 122
6.5 Conclusion... 125
Chapter 7 Conclusion.. 126
References 129
Appendix A 137
Appendix B 146

List of Figures

Figure 2.1 A flow separation model with the turbulent structures supplying small mean backflow. ID denotes incipient detachment, ITD denotes intermittent transitory detachment; D denotes detachment. The dashed line denotes $\langle U \rangle = 0$ locations; the solid line denotes maximum turbulent shear $\langle -uv \rangle_{\max}$ location; V_{re} denotes the mean re-entrainment velocity along $\langle U \rangle = 0$ contour (Simpson 1981).. 7

Figure 3.1 The specifications of the setup and free-stream velocity and pressure measurements. (a) The top view of the water channel showing the leading edge, flat section and the diffuser plate. (b) zoomed-in view of the diffuser section including the deflected mid plate and two coordinate systems (X, Y) and (X', Y') assigned to the deflected wall and the centerline of the measurement channel respectively. (c) The streamwise velocity, $\langle U \rangle$, and pressure coefficient, C_p, plotted versus streamwise locations (X') along Y'=0 line.. 23

Figure 3.2 Planar and Tomo-PIV Camera setup parts: (a) Planar setup including a breadboard, mirror mounts, and cameras installed under the water channel (b) Tomo-PIV setup including collimator, mirror, and cameras installed at the side of the channel window.............................. 27

Figure 3.3: The convergence analysis of mean streamwise and wall-normal velocities at X=0 and Y=0.05. (a) convergence plot of mean streamwise velocity for 7000 images, (b): convergence plot of mean streamwise velocity at last 1000 images, (c) convergence plot of mean wall-normal velocity for 7000 images, (b): convergence plot of mean wall-normal velocity at last 1000 images. 32

Figure 3.4: The convergence analysis of mean streamwise and wall-normal velocities at X=0 and Y=0.35. (a) convergence plot of mean streamwise velocity for 7000 images, (b): convergence plot of mean streamwise velocity at last 1000 images, (c) convergence plot of mean wall-normal velocity for 7000 images, (b): convergence plot of mean wall-normal velocity at last 1000 images. 33

Figure 3.5 The convergence analysis of mean streamwise, wall-normal and spanwise velocities. (a) convergence plot of mean streamwise velocity for 7000 flow fields at X=0.1, Y=0.01 and Z=0.1. (b) convergence plot of mean spanwise velocity at X=0.1, Y=0.01 and Z=0.1 for 7000 flow fields. (c) convergence plot of mean wall-normal velocity at X=0.1, Y=0.01 and Z=0.1.(d) convergence plot of mean wall-normal velocity at X=0.1, Y=0.06 and Z=0.1. 37

Figure 4.1 The correction process of a target image (a) The original image of the target plate (b) Mark detection (c) The corrected image. The corrected image has slightly rotated counter clockwise (as the dark region in the top-right corner of figure (c) shows it) in a way that the horizontal and vertical axes of the image align with the coordinate of the marks....................... 41

Figure 4.2 The image of the entire target is made by stitching of four images captured by four cameras. The images have a good alignment at the overlap regions. 42

Figure 4.3Velocity field captured by camera 1 after applying perspective and coordinate corrections.. 42

Figure 4.4 Initial stitching of velocity field for (a) one instantaneous velocity field and (b) average flow field with background contours of $|\boldsymbol{U}|$. 44

Figure 4.5 Interrogation windows selected for applying NCC functions are shown in the velocity filed of (a) Camera 1, and (b) Camera 2. 45

Figure 4.6 Average NCC maps for (a) window 1 (b) window 2 before applying corrections for camera fields 1 and 2. 46

Figure 4.7 The selected interrogation window centers in the flow field of camera 2 (red crosses) and the ones match the interrogation windows selected in the flow field of camera 1 according to NCC (blue crosses). The misalignment between the lines is exaggerated for better visibility. ... 47

Figure 4.8 Velocity Magnitude after correction using the cross-correlation method. The red arrows show the boundary lines for (a) instantaneous velocity field, and (b) average field with background contours of $|\boldsymbol{U}|$. 48

Figure 4.9 Average NCC maps after applying corrections explained in the previous section and tabulated in Table 4.1 for (a) window 1 and (b) window 2. 49

Figure 4.10 The velocity difference, ΔV_d, in the overlap regions of neighbor cameras calculated (a) before and (b) after applying corrections using NCC functions.. 51

Figure 4.11 Locations selected in the overlap regions to investigate the fluctuations of velocity difference, ΔV_d. 52

Figure 4.12 Magnitude of average velocity, $|\boldsymbol{U}|$, is plotted versus streamwise location along 5 lines passing different wall-normal locations. 53

Figure 4.13 Streamwise velocity variation for one instantaneous velocity field as shown by (a) the original data points and the smoothed ones calculated by averaging over nearby data points at

Y=1.8×10^{-3} (0.295 mm) along streamwise direction; and (b) the contours of zero velocity of the vector field plotted to be compared to the extracted velocity profiles. The vector field is spatially down-sampled for better visualization. 57

Figure 4.14 Distribution of vector fields in the defined bins for (a) planar data and (b) Tomo-PIV data. Bin 1 (single detachment) contains the maximum number of vector fields for both sets of data. 59

Figure 5.1 Mean velocity vector field with background colormap of velocity magnitude $|\boldsymbol{U}|$ (m/s). The vector field has been spatially decimating by the factor of 3 along Y direction and 50 along X direction for better visualization in this figure. 63

Figure 5.2 Streamwise mean velocity, <*U*> (m/s). The streamwise velocity decreases along streamwise direction, and a recirculation region appears downstream of the FOV. 63

Figure 5.3 Wall-normal mean velocity, <*V*> (m/s). Downstream of the FOV, the V component is smaller in magnitude compared with the upstream, and in the separation region its magnitude is almost zero compared to <*U*> component. 64

Figure 5.4 The configuration of streamlines in the freestream and close to the recalculation zone. The streamlines are deflected close to the detachment point. The background color shows <*U*> normalized by U_c. 64

Figure 5.5 Distribution of γ (%). γ is between 35% to 92% at the wall in this FOV, which includes ITD (80%) and TD (50 %) points. 65

Figure 5.6 Probability distribution of U at X=0 and Y= 0.0036H. 66

Figure 5.7 Distribution of Reynolds stresses (a) $<u^2>/Uc^2$, (b) $<v^2>/Uc^2$ and (c) $-<uv>/Uc^2$. The similar patterns of the stresses represent a high turbulence region above the recirculation zone. The dashed line shows the loci of the peak of $-<uv>$ at each streamwise location..................... 67

Figure 5.8 Distribution of third order moments including (a) $<u^3>$ (b) $<v^3>$ (c) $<u^2v>$ and (d) $<uv^2>$. Strong u and v fluctuations and their sign appear in these distributions. 69

Figure 5.9 Turbulence production terms are plotted normalized with $U^3{}_c$ including (a) $I = -<u^2> \partial<U>/\partial X / U^3{}_c$ (b) $II = -<uv> \partial<V>/\partial X / U^3{}_c$ (c) $III = -<v^2> \partial<V>/\partial Y / U^3{}_c$ and (d) $IV = -<uv> \partial<V>/\partial Y / U^3{}_c$. 71

Figure 5.10 Conditional averaging over strong single-detachment vector fields. (a) Vector field with background colormap of the magnitude of velocity, $|\boldsymbol{U_c}|$ (m/s), (b) streamwise velocity, $<U_c>$, and (c) wall-normal velocity, $<V_c>$. 73

Figure 5.11 Conditional average of Reynolds stresses including (a) $-<uv_c>$, (b) $<u_c{}^2>$ and (c) $<v_c{}^2>$. The distributions show different patterns compared with original Reynolds stresses....... 75

Figure 5.12 Conditional average of third-order moments including (a) $<u_c{}^3>$ (b) $< uv_c{}^2>$ (c) $< u^2v_c>$ and (d) $<v_c{}^3>$. Different patterns of the third moment suggest regions with strong u fluctuations... 77

Figure 5.13 Positions of points 1 to 16 at different streamwise and normal-wise locations (Y=0.0303H and Y=0.182H). 78

Figure 5.14 Quadrant analysis for all flow fields at points 1 (a) to 8 (h) located at Y=0.0303H. 81

Figure 5.15 Quadrant analysis for all flow fields at points 9 (a) to 16 (h) located at Y=0.182H. 82

Figure 5.16 Quadrant analysis for flow fields with single detachments at points 1 (a) to 8 (h) located at Y=0.0303H. 83

Figure 5.17 Quadrant analysis for flow fields with single detachments at points 9 (a) to 16 (h) located at Y=0.182H. 84

Figure 5.18 Quadrant analysis for the flow fields captured at $t_0-\Delta t$ with respect to single-detachment flow fields at points 1 (a) to 8 (h) located at Y=0.0303H. 85

Figure 5.19 Quadrant analysis for the flow fields captured at $t_0-\Delta t$ with respect to single-detachment flow fields at points 9 (a) to 16 (h) located at Y=0.182H. 86

Figure 5.20. Energy distribution of planar PIV and Tomo-PIV POD modes normalized by total kinetic energy. 87

Figure 5.21 The normalized POD (a) first, (b) second, (c) third, modes with energy portions of 22%, 11% and 5%, respectively. 90

Figure 5.22 The normalized POD, (a) fourth, (b) fifth and (c) sixth modes with energy portions of 4%, 3.8% and 3% respectively. 91

Figure 6.1 Magnitude of velocity, $|\boldsymbol{U}|$ (m/s) averaged over $Z=-0.01H$ to $0.01H$. The streamwise velocity decreases along streamwise direction, and close to the wall, it reaches almost zero and backward flow appears more downstream. 94

Figure 6.2 Mean velocity vector field with background colormap of streamwise velocity $<U>$ (m/s) averaged over $Z=-0.01H$ to $0.01H$. The vector field is spatially decimating by the factor of 2 in streamwise direction for better visualization. 94

Figure 6.3 Tomo-PIV FOV with contours of $|\boldsymbol{U}|$=0.025 m/s (blue), $|\boldsymbol{U}|$=0.015 m/s (green) and $|\boldsymbol{U}|$=0.005 m/s (yellow). 95

Figure 6.4 Mean velocity vector field with background colormap of streamwise velocity, $<U>$ (m/s) at (a) Y=0.01H (XZ plane) and (b) Y=0.03H (XZ plane). The vector field is spatially down sampled by the factor of 2 for better visualization. 95

Figure 6.5 Distribution of γ (%) averaged along Z direction. The γ values at the wall appears between 52% to 62% in the FOV. The detachment point located upstream of γ=50%. 96

Figure 6.6 Conditional average of instantaneous flow field for single-detachment velocity fields shown in (a) XY (Z=0) plane with background map of $<U_c>$ and (b) XZ plane (Y=0.03). 98

Figure 6.7 Conditional average of instantaneous flow field for single-detachment velocity fields shown in three-dimensional contours of streamwise velocity. Detachment is located at X=0. Red contour shows iso-surface of streamwise velocity of $<U_c>$=0.02 m/s, green shows $<U_c>$=0, and blue shows $<U_c>$=−0.02 m/s. 99

Figure 6.8 Conditional average of fluctuation velocity field for single-detachment vector fields shown in (a) XY plane (Z=0) with background map of u_c and (b) XZ plane (Y=0.03H). 100

Figure 6.9 Conditional averaged fluctuation velocity, $\boldsymbol{u_c}$, for single-detachment vector fields shown in three-dimensional contours of streamwise fluctuation component. Red contour shows iso-surface of u_c=0.02 m/s, green shows u_c=0 and blue shows u_c = −0.02 m/s. 101

Figure 6.10 Conditional averaged of instantaneous velocity vector field, $\boldsymbol{U}_c$ at $t_0-\Delta t$ shown in (a) XY plane (Z=0) with background map of $<U_c>$ and (b) XZ plane (Y=0.03H). Red contour shows iso-surface of streamwise velocity of $<U_c>=0.02$ m/s, green contour shows $<U_c>=0$ contour, and blue contour shows $<U_c>= -0.02$ m/s. 103

Figure 6.11 Conditional averaged of instantaneous velocity vector field at $t_0-\Delta t$ shown in three-dimensional contours of streamwise fluctuation component. Red contour shows iso-surface of streamwise velocity of $<U_c>=0.02$ m/s, green contour shows $<U_c>=0$ contour, and blue contour shows $<U_c>=-0.02$ m/s. 104

Figure 6.12 Conditional average of fluctuation velocity flow field, $\boldsymbol{u}_\mathrm{c}$ at $t_0-\mathit{\Delta} t$ shown in (a) XY plane (Z=0) with background map of u_c, and (b) XZ plane (Y=0.03). 105

Figure 6.13 Conditional average of fluctuation velocity flow field, $\boldsymbol{u}_\mathrm{c}$ at $t_0-\mathit{\Delta} t$ shown in three-dimensional contours of streamwise fluctuation component, red contour shows iso-surface of u_c=0.01 m/s, green shows u_c=0, and blue shows u_c =−0.01 m/s. 106

Figure 6.14 Conditional average of instantaneous velocity flow $\boldsymbol{U}_\mathrm{c}$ field at $t_0-2\Delta t$ shown in (a) XY plane (Z=0) with background map of u_c and (b) XZ plane (Y=0.03H). Primary separation occurred at X=0. 107

Figure 6.15 Conditional average of instantaneous velocity flow field $\boldsymbol{U}_\mathrm{c}$ at $t_0-2\Delta t$ shown in three-dimensional contours of u_c. Red contour shows iso-surface of streamwise velocity of $<U_c>=0.02$ m/s, green contour shows $<U_c>=0$, and blue contour shows $<U_c>=-0.02$ m/s. 108

Figure 6.16 Conditional average of fluctuation velocity flow field $\boldsymbol{u}_\mathrm{c}$ at $t_0-2\Delta t$ shown in (a) XY plane (Z=0) with background map of u_c and (b) XZ plane (Y=0.03H). Primary separation occurred at X=0. 109

Figure 6.17 Conditional average of fluctuation velocity flow field $\boldsymbol{u}_c$ at $t_0-2\Delta t$ shown in three-dimensional contours of u_c. Red contour shows iso-surface of u_c=0.01 m/s, green contour shows u_c=0, and blue contour shows $u_c = -0.01$ m/s. 110

Figure 6.18 First POD mode (ϕ^1) shown in (a) XY plane at Z=0 and (b) XZ plane at Y=0.03H. A uniform vector field represents breathing motion. Background map shows the magnitude of vectors. 112

Figure 6.19 First POD mode (ϕ^1) shown in streamlines and contours of $|\boldsymbol{\phi}^1|$=0.0035U_c (blue), $|\boldsymbol{\phi}^1|$=0.003U_c (green) and $|\boldsymbol{\phi}^1|$=0.0025U_c (yellow). 113

Figure 6.20 Second POD mode (ϕ^2) shown in (a) XY plane at Z=0 and (b) XZ plane at Y=0.03H. A uniform vector field represents breathing motion. Background map shows the magnitude of vectors. 114

Figure 6.21 Second POD mode (ϕ^2) shown in three-dimensional streamlines and contours of $|\boldsymbol{\phi}^2|$=0.0033 U_c (blue), $|\boldsymbol{\phi}^2|$=0.003 U_c (green) and $|\boldsymbol{\phi}^2|$=0.0025 U_c (yellow). Background map shows the magnitude of vectors. 115

Figure 6.22 Third POD mode (ϕ^3) shown in (a) xy plane at Z=0 and (b) xz plane at Y=0.03. A large vortex with the axis of rotation directed towards Y has appeared. Background map shows the magnitude of vectors. 116

Figure 6.23 Third POD mode (ϕ^3) shown in three dimensional stream liens and contours of $|\boldsymbol{\phi}^3|$=0.003 U_c (blue), $|\boldsymbol{\phi}^3|$=0.0015 U_c (green) and $|\boldsymbol{\phi}^3|$=0.0008 U_c (yellow). 117

Figure 6.24 Fourth POD mode (ϕ^4) shown in (a) *XY* plane at *Z*=0 and (b) *XZ* plane at *Y*=0.03*H*. A three-dimensional shedding motion has appeared. Background maps shows the magnitude of vectors. 118

Figure 6.25 Fourth POD mode (ϕ^4) shown in three-dimensional streamlines and contours of $|\boldsymbol{\phi}^4|$=0.003 U_c (blue), $|\boldsymbol{\phi}^4|$=0.0015 U_c (green) and $|\boldsymbol{\phi}^4|$=0.0008 U_c (yellow). 119

Figure 6.26 Fifth POD mode (ϕ^5) shown in (a) *XY* plane at *Z*=0 and (b) *XZ* plane at *Y*=0.03*H*. Background maps show the vector length. 120

Figure 6.27 Sixth POD mode (ϕ^6) shown in (a) *XY* plane at *Z*=0 and (b) *xz* plane at *Y*=0.03*H*. A saddle point appears with stagnation located at around *Z*=0 and *X*=0.05*H*. Background map shows the vector length. 121

Figure 6.28 Conditional averaging over POD coefficients (a_n) before and after the instant of single-detachments. 122

Figure 6.29. Reconstructed flow structures before and after the instants of single detachments (*T*=0) captured at (a) *T*=−3 with contours of $|\boldsymbol{U}|$=0.067U_c (blue) and 0.044U_c (yellow) (b) *T*=−2 with contours of $|\boldsymbol{U}|$=0.044U_c (blue) 0.0156U_c (yellow) (c) *T*=−1 with contours of $|\boldsymbol{U}|$=0.067U_c (blue) and 0.044U_c (yellow) (d) *T*=0 with contours of $|\boldsymbol{U}|$=0.067U_c (blue) and 0.044U_c (yellow) (e) *T*=1 with contours of $|\boldsymbol{U}|$=0.044U_c (blue) and 0.011U_c (yellow) (f) *T*=2 with contours of $|\boldsymbol{U}|$=0.044U_c (blue) and 0.0156U_c (yellow). 124

List of Tables

Table 3.1 Magnifications and digital resolutions of cameras. 25

Table 3.2. Specifications of PIV measurement for both planar and tomographic PIV. 28

Table 4.1 Rotation and scaling values applied to velocity fields 2, 3, and 4 based on displacements calculated using NCC functions and the procedure explained in Figure 4.7. Positive values of rotation refer to counter clockwise rotations. 48

Table 4.2 Relative distances calculated based on NCC functions before and after corrections for interrogation windows at three overlap regions. The relative distances are normalized by the size of interrogation windows, e=0.30 mm. Positive values of Δx show that window 2 located downstream of window 1, and positive values of Δy show window 2 located farther away from the wall compared to window 1. 50

Table 4.3 Locations of the monitored points selected in the overlap region of field 1 and 2 with respect to the separation point... 52

Chapter 1 Introduction

Flow separation is a well-known phenomenon in many engineering applications and it has been widely investigated (Simpson 1996). Separation of a boundary layer from a surface can occur due to a sharp geometric edge or an adverse pressure gradient (APG). A sharp edge causes a fixed separation front at the geometric singularity. This phenomenon has been extensively investigated using classical configurations such as flow over a backward-facing step (e.g., Troutt et al. 1984 and Le et al. 1997) or a blunt leading-edge (e.g., Kiya and Sasaki 1983 and Sigurdson 1995). The later flow separation has been investigated by Fairlie (1973) as they studied turbulent separation bubble over a flat surface generated by a diverging-converging upper wall. Similarly, Simpson et al. (1977, 1981, 1987, 1989 and 1996) performed research on pressure-induced turbulent boundary layer (TBL) separation on a flat plate in a wind tunnel and characterized flow properties upstream and downstream of the flow detachment using pitot tube, hot-wire and laser anemometer techniques. However, due to the complexity of the separated flow, PIV techniques can provide better understanding of this phenomenon and contribute to numerical studies (Cuvier et al. 2014 and Mohammed-Taifour and Weiss 2016).

Other two-dimensional cases include the study of TBL separation over the trailing-edge flap by Thompson and Whitelaw (1995). They applied passive control vanes on the side walls to reduce the growth of corner flows and also added layers of screens in between the pressure side of the flat plate and the tunnel wall to enforce a potential flow. Although most of the experiments have applied complicated and carefully adjusted setups to enforce an idealized two-dimensional mean flow with separation, flow separation in industrial applications are commonly three-dimensional even in the mean flow (Cherry et al. 2008). In addition, a flow setup, which is symmetric and 2D within manufacturing tolerances, does not necessarily lead to a 2D separated mean flow. These corner structures affect the entire flow field and cause three-dimensional features in the mean flow even far from the corners and create significant secondary flow motions (Malm et al. 2012).

The 3D separated flows are more challenging for numerical simulations as most common turbulence closure models fail to correctly predict the flow (Malm et al. 2012).

In flows with 2D separation, detachment is typically identified where wall shear stress is zero. The transient behavior of the separation point is characterized using the amount of time the backward flow exists, as defined by Simpson et al. (1977). The classical inner layer scaling of wall flows does not hold close to the separation region since wall shear stress diminishes. Simpson (1983) proposed a scaling law based on the intensity and location of maximum backflow velocity. A general scaling of the velocity profile in the separation and backflow region with small wall shear stress is still an open question (Skote and Henningson 2002).

The quadrant analysis categorizes the streamwise and wall-normal components of fluctuation velocity (u and v) into four categories: Q1 ($+u$, $+v$), Q2 ($-u$, $+v$), Q3 ($-u$, $-v$) and Q4 ($+u$, $-v$) (Wallace et al. 1972). This analysis helps understand the distribution of the flow events and the contributions of each quadrant (Q) to the Reynolds shear stress (Wallace 2016). The quadrant decompostion of Krogstad and Skåre (1995) in APG boundary layer showed attenuation of ejection events (Q2) and apearance of near wall motions in Q1 associated with the wall reflection of large-scale outer layer inrushs (i.e., sweeps or Q4). Krogstad and Skåre 1995 also reported that strong APG reverses turbulent transport from an outward direction in zero pressure gradient boundary layer to an inward transport, which supports the quadrant distributions. The experiment of Song and Eaton (2002) also demonstrated stronger sweep motions relative to ejections below the inflection point of the mean velocity profile over a separation bubble.

Thompson and Whitelaw (1985) observed an increase of normal Reynolds stresses at upstream and downstream of the separation bubble due to the curvature of streamlines. Cuvier et al. (2014) observed two isolated regions of large production of streamwise Reynolds stress in the beginning and the middle of the separation bubble due to flow deceleration and flapping motion of large-scale structures, respectively. An APG also increases the strength of vortical structures of the outer layer, which results in an increase of the Reynolds shear stress and a second peak in the turbulent energy (Lee and Sung, 2008).

Three-dimensional regions of the flow, over which specific parameter of the flow has time or spatial correlation, are defined as coherent structures (Robinson 1991). The evolution of the coherent structures of a TBL as a result of APG or separation has been investigated mostly through numerical simulations (Lee and Sung, 2008). The high turbulence region of the separation zone is dominated by large coherent structures with strong negative or positive streamwise velocity fluctuations reaching above 25% of mean velocity (Cuvier et al. 2014). The DNS of a TBL under APG by Lee and Sung (2009) demonstrated weakening of streaks and increase in their spanwise spacing up to four times of that in zero pressure gradient (ZPG). DNS of Lee and Sung (2009) in APG showed evidence of quasi-streamwise and hairpin vortices using linear estimates of the conditional eddies around ejection motions. The DNS of Marquillie et al. (2008) showed that low-speed streaks gradually disapearing upstream of the separtion due to formation of strong vortices. The streaks reappear downstream and new vortices are also generated downstream of the reatachment. However, the coherent structures which are specific to 2D or 3D separated flows have not been investigated in detail. Detailed characterization of these turbulent structures is required to understand the unsteady organization of separation and to develop turbulence models.

The separation front is always unsteady and irregular due to patches of local backflow instead of a line separating forward from backward flow (Simpson 1989; Na and Moin 1998). The unsteadiness in separation with 2D mean flow has been associated with two dominant large-scale motions of (a) shear layer flapping (also called breathing motion) and (b) roll-up or shedding of spanwise vortices in the shear layer (Kiya and Sasaki 1983; Cherry, Hillier and Latour 1984; Mohammed-Taifour et al. 2016). These two motions are common in both geometry-induced and pressure-induced flow separation (Mohammed-Taifour et al. 2016).

The Proper orthogonal decomposition (POD) analysis was first introduced by Lumley (1967) for fluid mechanics applications. This analysis provides better understanding of flow structures and their energy distribution and can be used to remove low-energy small-scale structures and noise of the measurement. This method extracts flow motions based on energy content and sort them based on their energy contribution to the flow (Sirovich 1987). The POD analysis of Mohammed-Taifour et al. (2016) using a planar particle image velocimetry (PIV) over a larger field-of-view showed that the first POD mode is associated with the breathing motion and contains 30% of the total turbulent kinetic energy. Mohammed-Taifour et al. (2016) reported about 90% variation of the bubble size in their flow configuration as a result of this mode. Weiss et al. (2015) observed a medium *St* of about 0.35 for the roll-up of vortices, which is in agreement with the range of values obtained in DNS of Na and Moin (1998). However, the importance of the flapping and shedding modes and possible presence of additional modes in 3D separated flows is still not clear.

The 3D separated flows have been traditionally investigated using surface visualization techniques such as oil-streaks to identify topological characteristics of the flow using the critical point theory (Werle 1973). This theory is based on the surface patterns of skin-friction lines around a critical point. The skin-friction lines are streamlines at the limit of zero wall-normal distance while a critical point is the locus of zero wall shear stress (Délery et al. 2001). The flow pattern surrounding the critical point can be of different types including a saddle, focus, and node point (Délery et al. 2001).

Conditional averaging is a powerful technique, which has been frequently used in turbulent flow studies as described by Adrian (1977). Adrian (1977) described several conditional averaging methods and their mathematical details. Duquesne et al. (2015) observed that the size and shape of the 3D separation zone in the bulb diffuser fluctuates without any periodicity. They identified a saddle point on the diffuser side-wall by conditional averaging while POD modes identified series of foci and saddle points at the separation instants. Malm et al. (2012) observed large-scale periodic coherent structures in DNS of the 3D diffuser of Cherry et al. (2008). They associated these structures with large streaks formed by sinusoidal oscillations within the diffuser. Therefore, as the previous surface visualizations and the limited number of modern flow measurements suggest, the dominant coherent structures depends on the confinement and boundary conditions of the flow configuration.

In this study, characteristics of three-dimensional turbulent flow separation have been investigated using PIV techniques. Turbulent statistics of three-dimensional flow separation have been analyzed and compared with characteristics of two-dimensional flow separation cases available in the literature. The turbulent structures that have the greatest contribution on the flow at the instant of flow separation are characterized and investigated using conditional averaging, quadrant analysis and POD techniques.

The chapters of this study are organized as follow:

Chapter 2: previous studies on three and two dimensional flow separation are presented in detail including numerical and experimental studies. They have focused on mean velocity field, turbulent statics and turbulent structures in the vicinity of flow separation for different flow configurations.

Chapter 3: the planar and tomographic experimental setups are explained here in addition to a description of the experimental uncertainties.

Chapter 4: Different analyses performed in this study are detailed including velocity vector stitching, conditional averaging, quadrant analysis and POD analysis.

Chapter 5: The two dimensional results captured by planar PIV measurements are presented.

Chapter 6: The three dimensional results captured by Tomo-PIV measurements are presented.

Chapter 7: Conclusions of the study are made and some suggestions are proposed for future studies.

Chapter 2 Literature review

2.1 Turbulent separated flow

As flow passes over a solid wall, due to no-slip boundary condition at solid walls and viscous forces, the flow close to the wall decelerates and a low speed region forms. This region is first explained and named as a "boundary layer" by Prandtl (1904). As a boundary layer develops over a long solid interface, the boundary layer becomes turbulent for Reynolds number ($R_e = U_\infty x / \nu$) greater than about 5×10^5, where U_∞ is free-steam velocity, x is the distance from the leading edge of the solid wall where the boundary layer starts forming, and v is kinematic viscosity. TBLs are complex phenomena, and they have been widely investigated. As a TBL proceeds in streamwise direction, the flow pressure close to the wall may vary due to change in the geometry of the wall or the curvature of streamlines. Sufficient APG or sudden change in the geometry of the wall (backward-facing step) cause the flow close to the wall to decelerate untill the velocity gradient at the wall ($\partial\langle U\rangle/\partial y$ for two-dimensional separation, where U is streamwise velocity and y is wall normal direction) becomes zero. Further downstream, the flow may move backward, and $\partial\langle U\rangle/\partial y$ becomes negative. In this case, the streamlines detach from the wall and a recirculation region forms (Figure 2.1), which is called flow separation. In another point of view, Simpson (1987) defined flow separation as thickening of the boundary layer or the rotational flow regions accompanying a strong wall-normal velocity component.

A great number of studies have been undertaken to understand and prevent separation of TBL in many engineering applications such as airfoils, diffusers, and propellers (Simpson 1996 and Burger 2007). Delaying or advancing flow detachment can enhance the performance of many flow systems (Gad-el-Hak 2000). In the case of airfoils at high angle of attack, APG causes flow separation and recirculating flow at the trailing-edge, which causes unfavorable effects on the performance of airfoils including sudden decrease in lift, drag increase, and vibration. Most of the studies on flow separation are focused on flow detachment due to sudden geometry change (Kiya and Sasaki 1983; Cherry et al. 1984). However; Simpson (1996) performed research on pressure-induced TBL separation on a flat plate and characterized flow properties upstream and downstream of the flow detachment as shown in Figure 2.1. In this type of flow separation, unlike the former case in which separation occurs at geometric singularities, separation occurs instantaneously at different streamwise locations. However, the probability of detachment occurrence varies upstream and downstream of the separation region. The present study is focused on the later type of flow detachment.

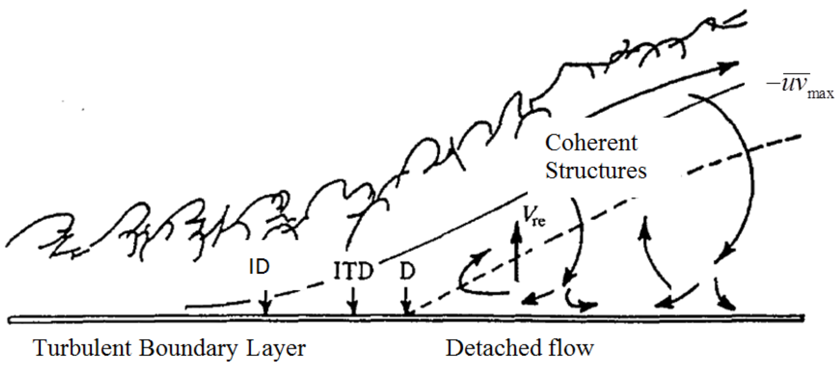

Figure 2.1 A flow separation model with the turbulent structures supplying small mean backflow. ID denotes incipient detachment, ITD denotes intermittent transitory detachment; D denotes detachment. The dashed line denotes $\langle U \rangle = 0$ locations; the solid line denotes maximum turbulent shear $\langle -uv \rangle_{max}$ location; V_{re} denotes the mean re-entrainment velocity along $\langle U \rangle = 0$ contour (Simpson 1981).

Simpson (1996) proposed a quantitative definition on unsteady properties of the separation line and the detachment state of the flow in the separation region based on the fraction of time in which flow moves downstream, γ. As shown in Figure 2.1, incipient detachment (ID) is the point where $\gamma = 0.99$, which means the flow changes its direction to upstream for 1% of the time. Intermittent transitory detachment (ITD) occurs where $\gamma = 0.80$. Transitory detachment (TD) occurs with instantaneous backflow 50% of the time ($\gamma = 0.50$), and detachment (D) occurs where the time-averaged wall shearing stress is zero. Experimental data shows that TD and D are at the same location (Simpson et al. 1996). The region just downstream of ID is the region that the thickness of the boundary layer significantly increases (Simpson 1995). It is suggested by Buckles et al. (1984) that shear-layer vortices transfer fluid toward the wall and the reversed-flow sends fluid upward into the shear layer (re-entrainment flow) as shown in Figure 2.1.

2.2 Governing equations

Due to the complexity of mathematical description of turbulent separation, some simplifying assumptions are made here to describe the general characteristics of flow separation. First, the boundary conditions of the flow are assumed to be two-dimensional and same for different spanwise locations. Therefore, the setup has the same boundary conditions at different spanwise locations and the statistical properties of the flow should remain homogeneous along spanwise direction. The streamwise and wall-normal directions are the only spatial directions appear in the governing equations. However, it will be discussed that three-dimensional corner flows can develop along streamwise direction and affect the entire configuration of the flow in the experiment. Second, flow separation occurs on a flat plate due to strong APG, and a Cartesian coordinate is used to describe the flow and boundary conditions. Third, the flow is assumed incompressible, which simplifies the governing equations. As a result, Reynolds-average form of the Navier-Stokes equation in the direction of $(x, y) = (x_i)_{i=1,2}$, where x is streamwise direction and y is wall-normal direction, can be written as

$$\frac{\partial < U_i >}{\partial x_i} = 0$$

$$\rho\left(\frac{\partial < U_i >}{\partial t} + < U_j > \frac{\partial < U_i >}{\partial x_j}\right) = -\frac{\partial < P >}{\partial x_i} + \mu\frac{\partial^2 < U_i >}{\partial x_j{}^2} - \rho\frac{\partial < u_i u_j >}{\partial x_j} \tag{2.1}$$

where $u = U - <U>$ is velocity fluctuation and U is instantanious velocity. APG appears as positive values of $\partial<P>/\partial x$ in Equation (2.1) and $\partial<P>/\partial z$ is assumed to be zero due to the assumed two-dimensionality of flow sepration.

The three-dimensional nature of flow separation adds more complexity to modeling the turbulent stress term in the Reynolds averaged equation (Simpson et al. 1977). It is difficult to describe this phenomenon using TBL equation, which was initially invesigated by Clauser (1956). Since many simplifying assumptions are applied to the Navier-Stokes equations such as neglecting pressure-gradient and the streamwise derivative of Reynolds stresses terms (Skote and Henningson 2002), which are not valid close to the separation point (Skote and Henningson 2002). TBLs subjected to high APG have significantlly different oraganisation of the mean profie, the turbulent structures, and distribution of Reynolds stresses compared to ZPG TBLs. The available numerical models used for ZPG TBLs have inaccuracies in describing features of turbulent flow separation at low computing cost (Cuvier et al. 2014). Models such as Spalart–Allmaras, k–ϵ, and shear stress transport (SST) fail to accurately predicting the size of recirculation bubble, the recovery and backflow regions, and other properties of the flow close to the separation point (Menter 1996, Song et al. 2000, Wasistho and Squires 2005). Most of the methods for predicting propeller performance use complex and semi-empirical models due to the complexity of the modeling of separation (Burger 2007). Therefore, researchers have performed several experiments to understand the mechanisms involved in the flow detachment, which helps implementing more accurate numerical models (Cuvier et al. 2014).

2.3 Mean velocity profile

The mean velocity profile changes as the TBL is subject to APG. For instance, the log law region shrinks, the wake region expands, and the upper part of the inner region does not follow a standard log-law at higher APG (Webster et al. 1996). Skote and Henningson (2001) suggested that the mean profile in the log-law region subjected to APG can be described as

$$U^+ = \frac{1}{K}\left(\ln y^+ - 2ln\,\frac{\sqrt{1+\frac{\partial P^+}{\partial x}y^+}+1}{2} + 2\left(\sqrt{1+\frac{\partial P^+}{\partial x}y^+}-1\right)\right) + C \tag{2.2}$$

where U^+=<U>/u_τ, $y^+=y/u_\tau$ and $u_\tau=(\nu\, \partial$<U>$/\partial y)^{1/2}$ calculated at the wall (y=0). The parameters C and K are set to be 0.5 and 0.41 respectively. By setting the pressure gradient term to zero this equation gives the standard log-law equation (Zagarola et al. 1997). There are theories that provide a power-law equation for the inner and the outer part of the APG TBLs (Cuvier et al. 2014), however, they still do not completelly describe the mean profile in these regions (e.g., Castillo and George 2001; Skote and Henningson 2001; Townsend 1976). Perry and Schofield (1973) provided an empirical equation for the velocity profile of the inner and the outer regions of APG boundary layers on flat and low-curvature surfaces upstream of the flow detachment with the condition that the maximum shearing stress, $-$ <uv>$_{max}$, is less than 1.5 τ_w / ρ, where $\tau_w(= \mu\, \partial$<U>$/\partial y)$ is wall shear stress. They examined other velocity and length scales, and found out that the maximum shearing stress, $U_{mp}^{\,2} = -$ <uv>$_{\max}$ which occurs far from the wall for these types of flow, in addition to its location from the wall, L, are proper parameters for describing the velocity profile (Simpson 1996). Their empirical relation for the outer flow is as follow

$$\frac{U_\mathrm{e} - U}{U_\mathrm{s}} = 1 - 0.4\,\eta_2^{\,0.5} - 0.6\sin(\pi\,\eta_2/2) \tag{2.3}$$

where $\eta_2 = y/\Delta$ and $\Delta = (\delta\ /\ C)\ (U_e\ /\ U_s)$, in which U_s is set to adjust this equation to fit experimental data and $U_s / U_{mp} = 8(\Delta/L)^{0.5}$.$U_e$ is the mean velocity outside of the boundary layer. C_s is a universal constant given by $C_s = \int f_2(\eta_2)\, d(\eta_2)$ where $f_2(\eta_2) = (U_\infty - U(\eta_2))/U_\mathrm{s}$ across the boundary layer and it is empirically obtained as 0.35. For the backflow region, the mean velocity field can be characterized using the maximum negative velocity, denoted as U_N, and normal distance between the location of max negative velocity and the wall, denoted as N. N varies as the shear-layer thickness increases downstream of the separation point (Simpson 1996). Simpson (1996) divided the backflow into three layers: a viscous layer dominated by flow unsteadiness where Reynolds shear stress is almost zero; an intermediate layer, in which mean-velocity profile is almost semi-logarithmic and it is considered as an overlap region between the viscous wall and outer region; and the outer backflow region that is assumed to be a part of the outer-region flow. In the regions with no instantaneous backflow and zero Reynolds shear stress, law-of-the-wall type of velocity profiles as a function of τ_w do not govern the flow. Law-of-the-wall type of velocity profile have the form, $U^+=1/k \ln(y^+) + C$, where U^+ is dimensionless velocity normalized by shear velocity, y^+ is wall coordinate normalized by shear velocity and kinematic viscosity, and k and C are constants. Agarwal and Simpson (1990) showed that law-of-the-wall type of velocity profiles are not valid when $U_N / U_e < 1/4$, where U_N is the maximum back flow velocity. Simpson (1983) proposed a power-law equation for the viscous sublayer ($y / N < 0.02$ where N is the wall normal distance of the location with maximum backflow) as

$$U/|U_N| = -C_N(y/N) + P_1(y/N)^2/2 \tag{2.4}$$

where $P_1 = -N^2 / (\rho\, v\, |U_N|)\, dP/dx$. At the downstream of detachment, where the backward flow occurs more than 50% of the time, a semi-logarithmic equation for the overlap region is also proposed by Simpson (1983) as

$$U/|U_N| = A\,(y/N - \ln|y/N| - 1) - 1 \tag{2.5}$$

where A=0.3. This equation is derived for the data at the region with the mean backflow that $0.02 < y/N < 1.0$ and $N/\delta < 0.06$. This equation does not govern the flow very close to the wall ($y/N < 0.02$), because the properties of outer backflow region are influenced by the large-scale outer-region flow, which are different from the properties of viscous layer (Simpson 1989). For the viscous layer and other regions of the back flow, a number of empirical correlations are also provided by Simpson (1989).

2.4 Curvature effects

In many engineering applications, TBL passes over a curved surface as it is experiencing pressure gradient. As the streamlines are affected by the wall curvature, an additional term $\partial V/\partial y$ is introduced in the governing equations. Concave and convex curvatures have opposite effects on boundary layers (Tulapurkara et al. 2001). For instance, the TBL shows quick response to the appearance and removal of stabilizing convex curvature, in contrast, the reaction of TBL to concave curvatures is slow (Khoshnevis et al. 2009). Baskaran et al. (1987) proposed a new internal layer, which is formed as the flow passes over a curvature and the change in the curvature of the wall is significant. This new internal layer grows similar to a new boundary layer and appears to act independently from the presence the external-flow (Baskaran et al. 1987). Therefore, the behavior of turbulence close to the wall and the friction velocity is dictated by this layer. The external layer starts decaying as the internal layer develops (Baskaran et al. 1987). Baskaran et al. (1987) suggested that the internal layer determines the friction distribution and the occurrence of separation independent of the external layer. The knee point that appears in the external region of turbulent intensity profile for such flow can be explained by introducing this new layer (Baskaran et al. 1987).

2.5 Turbulent statistics

Upstream of the detachment point, the flow is subject to APG. Krogstad and Skåre (1995) concluded from their experiemntal study that APG increases the production of turbulence and signifficanlty changes the distribution of Reynolds stresses. The turbulent transport is observed to be toward the wall, and therefore, the inrushing fluid is being deflected by the wall significantly comparing with ZPG case (Krogstad and Skåre 1995). In the separation region, normal stresses ($<u^2>$, $<v^2>$ and $<w^2>$) and cross-stream pressure gradient, $\partial <P>/\partial y$, are associated with strong curvature of streamlines (Thompson and Whitelaw 1985).

In streamwise momentum-transport equation, turbulent diffusion has great contribution and is in balance with the pressure gradient terms (Thompson and Whitelaw 1985). In the equation of wall-normal momentum-transport, for the region immediately upstream the flow separation, the pressure gradient and convective terms dominate (Thompson and Whitelaw 1985). Downstream of the detachment, the pressure gradient terms are still dominant for both momentum equations, and Reynolds shear stress has higher magnitude compared with normal Reynolds stresses (Thompson and Whitelaw 1985). Reynolds shear stress pattern has found to have similarity with wall-normal velocity fluctuation pattern and also with the dominant production term ($<v^2> \partial <U>/\partial y$) of Reynolds shear stress in the vicinity of flow separation (Cuvier et al. 2014). This similarity indicates that the existing turbulent structures contain u and v fluctuations with similar characteristics. The region with large Reynolds stresses occurs downstream of the detachment point and extends in downstream direction (Cuvier et al. 2014).

The production of streamwise Reynolds stress, $<u^2>$, is significantly larger than the production of wall-normal Reynolds stress, $<v^2>$, in the separated region (Cuvier et al. 2014). This production is relatively high near the flow detachment due to deceleration of the flow and is dominated by the term $-<u^2> \partial <U>/\partial x$ (Cuvier et al. 2014). The production of Reynolds shear stress was also found to be high dominated by the term $-<uv> \partial <U>/\partial y$ downstream of the reattachment. This region is probably caused by the wall-normal flapping motion of the large-scale structures characterized by high u and v fluctuations (Simpson 1996 and Cuvier et al., 2014). The turbulent production was shown to be small inside the recirculation zone (Simpson 1996 and Cuvier et al., 2014). As explained, turbulent structures play an important role in explaining the Reynolds stress distributions. Therefore, Reynolds stresses should be modeled considering turbulent structures not only local mean velocity gradient (Simpson 1981).

2.6 Turbulent structures

Studying coherent structures contributes to understanding turbulent mechanisms, modeling, and flow control strategies (Robinson 1991). The formation and evolution of coherent structures can provide details of statistical properties of flow. The coherence and contribution to turbulent production are among the criteria to identify most important structures (Kähler 2004; Robinson 1991). The signature of coherent structures not only can be detected in the distribution of statistical parameters including Reynolds stresses, but also they appear in instantaneous flow fields (Robinson 1991).

2.6.1 Coherent structures in adverse-pressure-gradient

As the flow is subject to APG upstream of the detachment, turbulent structures of the boundary layer change in size and shape compared to ZPG boundary layer. Krogstad and Skåre (1995) observed that strong motions towards the wall, especially the Q4 motion, are more frequent in APG TBL, whereas, the Q1 and Q4 events are of same importance in ZPG TBL. The strong first quadrant events appear near the wall, which is associated with the wall reflection of large-scale outer layer inrushs (i.e., sweeps). The numerical simulation of Lee and Sung (2008) reported the same conclusions as the last experimental study. They also show that the low and high momentum streaks near the wall become week and their spacing increases and becomes irregular. However, the extent of the streaks in spanwise direction is almost the same for ZPG and APG TBLs (Lee and Sung 2008). APG increases the strength of vortical structures of the outer layer, which results in an increase in the Reynolds shear stress. The increase in Reynolds shear stress in this region causes the development of a second peak in turbulent production (Lee and Sung 2008). The second peak appears at $y/\delta \approx 0.5$ and has been observed in several studies (Skåre and Krogstad 1994). The near-wall vortical structures are found to become weak and their orientation changes by increasing the strength of the APG (Lee and Sung 2008). For instance, the space between the vortex heads increases and quasi-streamwise vortices become stronger in the nearwall region (Lee and Sung 2008). APG increases their inclination angle compared to the ZPG case (Lee and Sung 2009). Low momentum regions (LMRs) are also observed and are associated with hairpin structures similar to ZPG TBL (Adrian et al. 2000). LMRs are found to be more concentrated in the outer region of a TBL with APG (Adrian et al. 2000). Similar to ZPG, the LMRs increase in length with the distance from the wall (Lee and Sung 2009). Hain et al. (2016) investigated large-scale structures which are several times larger than the boundary layer thickness in APG TBLs. As the flow velocity decreases, these structures grow in spanwise direction and their length decreases in streamwise direction. However, by normalizing spatial correlations with the local velocity at the TBL edge, they noticed that the average shape and size of these superstructures existing in ZPG TBL are similar to APG TBL.

2.6.2 Unsteady structures of flow separation

Based on Section 2.1, it was noted that the direction of the flow frequently changes forward and backward in the vicinity of flow separation; this is one of the leading reasons behind the presence of unsteady structures within the flow separation. Strong three-dimensional structures populate the flow including focus and saddle structures close to the separation line as explained by Duquesne et al. 2015 and Simpson et al. 1977. Due to these structures, the separation surface is found to be highly unsteady, and its shape and size change instantaneously (Duquesne et al. 2015).

The high turbulence region of the separation zone is dominated by large-scale coherent structures, which can be characterized by strong u fluctuations (both negative and positive) with the magnitude reaching above 25% of mean velocity (Cuvier et al. 2014). These large-scale coherent structures can be as long as 3δ in streamwise direction and 0.5δ in spanwise direction, where δ is boundary layer thickness close to the flow detachment. High-momentum structures in the outer part of the TBL in this high-turbulence region are observed with almost similar size compared to the similar upstream structures (Cuvier et al. 2014). In a numerical study of a channel flow, Skote and Henningson (2002) found that the structures convected from the upstream of the separation region are lifted above the recirculation zone and are weakend downstream. In a simillar numerical study, Marquillie et al. (2008) showed that low-speed streaks are observed before the seperation point, but are not present close to the separtion. However, they once again reappear downstream of the seperation location. They associate their breakdown with strong vortices existing at the separation region. Although intense generation of vortices happens downsteam of the detachment region, strong vorticies are not observed upstream of the separation region (Marquillie et al. 2008). Concerning sweeps and ejecions, upstream of the separation region where pressure gradient is small, ejection motions have the dominant contribution to Reynolds shear stress for $y^+>12$ compared with sweep motions.

However, close to the detachment point on a smooth plate, sweep motions have the most contribution due to the passage of the large eddies close to the wall below the mean-velocity inflection point (Song and Eaton 2002).

2.6.3 Large motions of the separated flow

Two dominant large-scale motions of the separated flow are found and characterized using POD analysis (Kiya and Sasaki 1983; Cherry, Hillier and Latour 1984; Mohammed-Taifour et al. 2016). These motions are called breathing motion and shedding motion by (Mohammed-Taifour et al. 2016). Mohammed-Taifour et al. (2016) performed investigation on a pressure-induced turbulent recirculation zone formed on a flat plate by diverging and converging the wind tunnel walls resulting in high local APG. They showed that the first POD mode (called breathing mode) of the flow contains 30% of the total turbulent kinetic energy, and this mode represents low-frequency expansion and contraction of the recirculation zone and corresponds to low-frequency wall-pressure fluctuation. Mohammed-Taifour et al. (2016) reported that the variation of the bubble size in their flow setup is observed to be 90% of the bubble size. A POD study on three-dimensional flow separation in a diffuser also shows that quasi-periodic motions exist in the flow at low frequency (Malm et al. 2012). Large streamwise streaks spanned half the width of the diffuser are associated with this quasi-periodic motion and first POD mode (Malm et al. 2012). They explained this motion as unsteady interaction between the forward flow and the separated flow.

The second unsteady mode represents the frequency of the passage of the large-scale vortices and their shedding downstream of the recirculation zone as they are visualized and tracked by Mohammed-Taifour et al. (2016). Strong vortical structures were successfully visualized using both Q criterion on filtered velocity fields and the technique defined by Graftieaux et al. (2001) to detect the vortices and determine the frequency of their passage in the flow field (Mohammed-Taifour et al. 2016). The average passage frequency of these structures matches the frequency of the maximum pressure fluctuations on the wall (Mohammed-Taifour et al. 2016). Malm et al. (2012) also observed large-scale shedding in three-dimensional flow separation, but could not find a POD mode only associated with vortex shedding.

2.6.4 Three-dimensional flow separation

Three-dimensional features may appear in separated flows due to small asymmetry in the flow setup or the inflow condition. Three-dimensional flow separation is an important and challenging topic, and its complicated nature is still a mystery and under investigation (Tobak and Peake 1982; Délery, 2001). Critical points appear in the separation regions, and they include saddle, foci, and node points. Varieties of velocity vector patterns are possible based on flow configurations and boundary conditions (Délery et al. 2013). For three-dimensional flow separation, flow detachments can be detected at the points or lines where skin friction is zero; however, skin-friction lines have complicated patterns. One criteria of the occurrence of flow separation can be defined as the convergence of skin-friction lines, which occurs in the mentioned critical points (Tobak and Peake 1982). At the regions where skin-friction lines converge, the forward flow close to the wall has a strong upward motion away from the wall. Therefore, this criterion also satisfies the condition of strong upward motion, which is also a suggested defining criterion for two-dimensional flow separation (Tobak and Peake 1982; Simpson 1987).

Duquesne et al. (2015) studied three-dimensional separation in the diffuser of a turbine. They reported several foci and saddle points existing in the flow close to the wall. Malm et al. (2012) investigated flow features in a three-dimensional diffuser. The asymmetry of the walls of the diffuser causes corner vortices with different shape and strength appear and develop downstream. These corner structures affect the entire configuration of the flow separation and cause three-dimensional features in the mean flow even far from the corners and create significant secondary flow motions (Malm et al. 2012).

2.7 Methods of investigation of unsteady turbulent structures

A number of statistical techniques have been developed during last decades to investigate turbulence events in space and time (Robinson 1991). These techniques are used to explain the contribution of events to statistical properties of the flow (Robinson 1991). To name a few, the variable-interval time average (VITA) method and the quadrant analysis are used in several studies (Robinson 1991). VITA algorithm provides information about shear-stress-producing motions, which was previously used to analyze hot-wire signal (Morrison et al. 1989). VITA is based on conditional sampling of a signal based on a criterion and a threshold (Blackwelder and Kaplan 1976). The criteria and thresholds allow detection of the events associated with sudden and strong change of a variable (Robinson, 1991). VITA has been used for pattern recognition in turbulence and detecting the passage of shear layer (Robinson 1991).

The POD analysis is another statistical method to investigate dominant turbulent structures (Lumley 1967). POD breaks each flow velocity field to several modes and ranks them based on their turbulent kinetic energy. It is possible to find out more specifications of the flow such as high and low energy regions, the symmetry of the flow, incompressibility of the flow, and interactions of turbulent structures using POD (Berkooz et al. 1993). In addition, using these modes, small-scale structures and measurement noise can be filtered (Duquesne et al. 2015). Duquesne et al. (2015) utilized POD to investigate unsteady flow separation in a turbine diffuser. They studied the energy content of the flow structures with regard to the size and the location of the flow separation (Berkooz et al. 1993). Using the vector field method (Sirovich 1987), they obtained POD-reconstructed velocity fields to detect critical points in the flow. They used Poincaré–Bendixson index (PBI) and characterized the critical points with topological functions.

It has been reported that conditional averaging analysis provides consistent results for numerical and experimental data (Adrian et al. 1989). Duquesne et al. (2015) used conditional averaging method to provide a better picture of the separation front. One simple idea is to perform the conditional averaging based on the occurrence of the backflow and its strength to characterize the separation front movements and the associated events (Duquesne et al. 2015). As far as for the cases that flow separation happens in a three-dimensional geometry, the separation line is not identical to the boundaries where longitudinal backflow $U\ (x,y,t)<0$ occurs (because backflow might have components in z direction), this criteria is an approximate indicator of the presence of the separation zone. The movement of the separation line is also investigated using other criteria for conditional averaging, which is categorizing velocity regions to three cases: negligible backflow (less than 0.5% of the velocity vectors are negative), moderate backflows (between 0.5% and 33%), and important backflows (more than 33%) (Duquesne et al. 2015). Using this technique, features of the conditionally-averaged mean flow influenced by different turbulent structures can be observed.

Corino and Brodkey (1969) and Willmarth and Lu (1972) investigated sweep and ejection processes, using well known probability distribution of u and v. In a TBL, the probability of spending time in the second ($Q2$) and fourth ($Q4$) quadrants of the u-v plane is higher compared with the other quadrants. Events in the second quadrant are referred as ejections, in which negative fluctuations are moved far from the wall by positive fluctuations normal to the wall. The fourth quadrant is for positive fluctuations which are moved toward the wall, and they are called sweeps (Adrian et al. 2007; Corino et al. 1969). Song and Eaton (2002) investigated sweeps and ejections of a separated flow over a smoothly contoured ramp and their contribution to the Reynolds shear stress. They found that below the mean-velocity inflection point at the separation region, the sweeps have greater probability compared with ejections due to the passage of the large eddies (Song and Eaton 2002).

2.8 Conclusion

To sum up, previous studies have mostly focused on two-dimensional flow separation. They have characterized the properties of the flow upstream and downstream of the flow detachment, the frequency of backward motion and the development of mean velocity profile. The effects of the wall curvature on the boundary layer are also discussed. The organization of turbulent structures upstream of flow detachment as the flow experiences APG has been investigated in the previous literature, but there are minor studies on the turbulent structures at the vicinity of flow detachment. However, some dominant motions in the flow have been reported in the separated flow, which are associated with the strong pressure fluctuations at the wall. Three-dimensionality of flow separation adds complexity to this phenomenon. For instance, the flow detachment has complex geometry and may contain several critical points. Different methods on investigating turbulent structures are reviewed including the VITA method, the POD analysis, conditional averaging and the quadrant analysis.

Chapter 3 Experimental Setup

The experimental setup described in this chapter is designed to generate separation of a relatively thick TBL over the expanding section of a diffuser. Using auxiliary plates installed in a water channel, the cross section of the flow is varied along streamwise direction to create APG and separation of the boundary layer. Planar PIV and Tomo-PIV setups are presented in this chapter. The measurement area covers upstream and downstream of the flow detachment point ($\partial\langle U\rangle/\partial y = 0$). The free-stream pressure and streamwise velocity are also measured along the centerline of the channel using Pitot tube.

3.1 Flow Facility

A TBL is formed on a vertical plexi-glass plate installed in a water flume. The top view of the water channel is shown in Figure 3.1. The dimensions of the setups are normalized by change in the width of the cross section as denoted by H (=165 mm). The water flume is about 5 m (30.3 H) long, and the cross section of the channel has 0.65 m (3.94 H) width and 0.52 m (3.15 H) height. The water level height from the bottom of the channel is 0.49 m (2.97 H) at the measurement region.

One portion of the upstream flow in the channel enters the measurement channel where flow separation occurs, and the other passing the other side of the plates as shown in Figure 3.1. A curved plate installed at the leading edge of the plate to let the flow smoothly enter the measurement path. The boundary layer formed on the leading edge curve is tripped about 150 mm (0.9 H) downstream of the end of the leading-edge curve using a 1.5 mm diameter wire as shown in Figure 3.1 (b). The straight section of the channel has slight change in the cross section area as its width is 1.52H upstream of the section and it increases to 1.6H downstream of it as shown in Figure 3.1 (a) and (b). This small variation in the cross section area helps adjust the separation location at the current position in order to provide enough measurement space upstream and downstream of the separation point in the diffuser section. The inclined plate of the diffuser section is connected to the upstream flat plate by a curved plate, which lets the flow smoothly pass to the high pressure region. The curved plate is a circular arc with 15° angle and a radius of 0.6 m (3.64 *H*). This inclined plate is deflected 15° with respect to the upstream flat plate (18.4° with respect to channel walls) in order to increase the cross section of the flow and produce APG. The TBL develops over the straight section with estimated thickness of δ_{99} = 76 mm before the diffuser curve, which is calculated based on TBL growth equation proposed by Schlichting (1979, p. 638). As the TBL is subjected to APG in the diffuser section, its thickness increases to about 95 mm at the most upstream location of the field of view (FOV) (180 mm upstream of the detachment point). The inclined plate of the diffuser section is connected to another flat plate at the very downstream as shown in Figure 3.1 (a) in order to prevent the flow passing by the other side of the plates from mixing and affecting the flow at the measurement region. A top plate is also installed above the measurement region at the water level, in order to damp surface waves and prevent their interaction with the flow.

Two coordinate systems are defined and assigned to the flow setup, first coordinate system (x, y) is attached to the inclined plate and its origin coincides with the detachment point. This coordinate systems is normalized as $X = x / H$ and $Y = y / H$, where x and y are in mm normalized by (H=165 mm). The origin of the second coordinate system (x', y') coincides with the centerline of the channel and the streamwise location of the detachment point. This coordinate system is also normalized as $X' = x' / H$ and $Y' = y' / H$, where x' and y' are in mm normalized by H as shown in Figure 3.1 (b). The free-stream velocity and pressure measurements are performed along the centerline of the channel (Y'=0) using Pitot tube as shown in Figure 3.1 (c). The velocity at the center of the straight wall channel (just before the diffuser) is 0.45 m/s, it drops to 0.41 m/s at the streamwise location of the detachment point, and reaches 0.36 m/s downstream of the diffuser section as shown in Figure 3.1 (c). The pressure coefficient is defined as $C_p = (p-p_c) / (0.5\times\rho\times U_c^2)$, where p_c and U_c (=0.45 m/s) are static pressure and velocity at $X' = -9.8$ and $Y' = 0$. The pressure coefficient is plotted in Figure 3.1 (c).

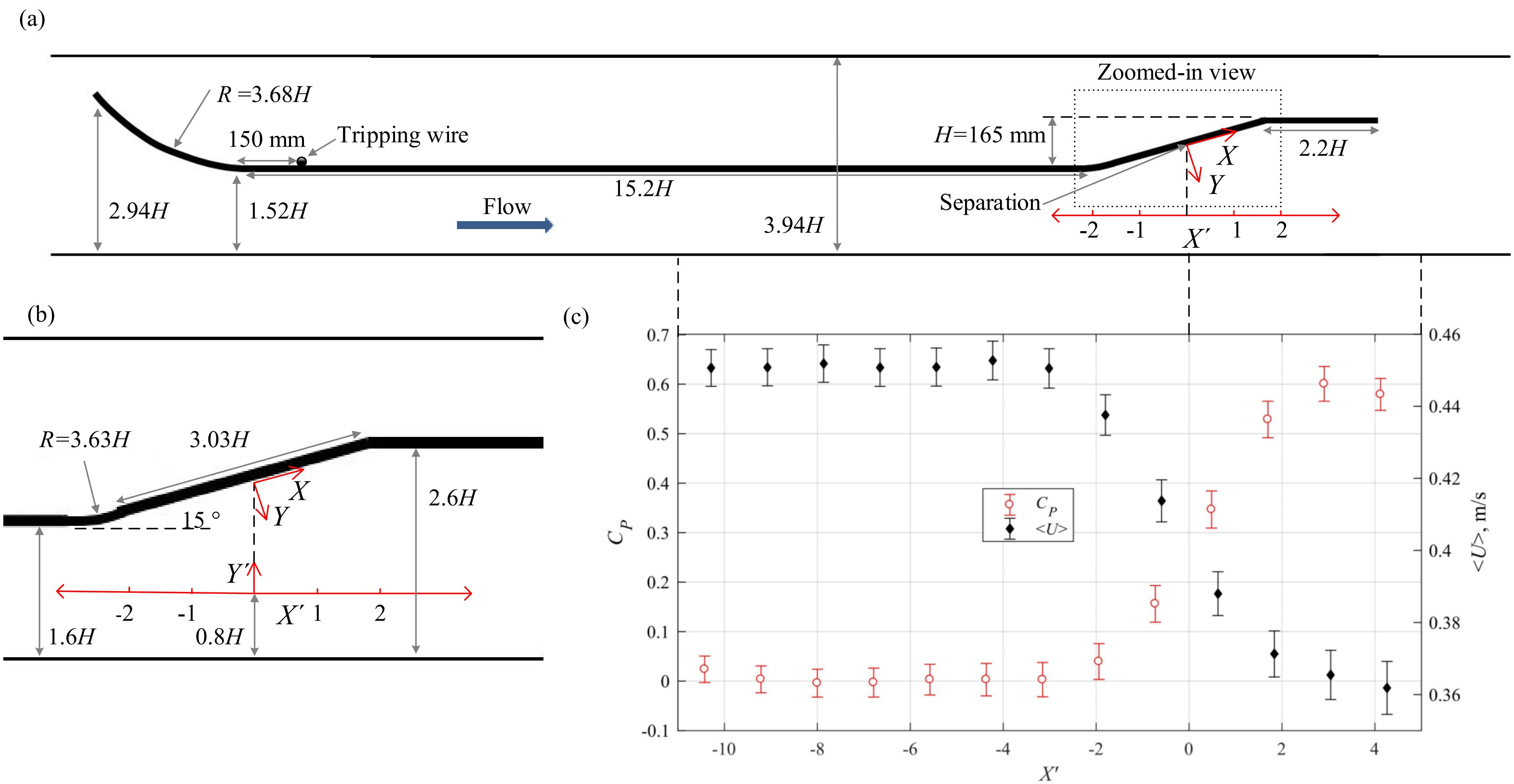

Figure 3.1 The specifications of the setup and free-stream velocity and pressure measurements. (a) The top view of the water channel showing the leading edge, flat section and the diffuser plate. (b) zoomed-in view of the diffuser section including the deflected mid plate and two coordinate systems (X, Y) and (X', Y') assigned to the deflected wall and the centerline of the measurement channel respectively. (c) The streamwise velocity, <U>, and pressure coefficient, C_p, plotted versus streamwise locations (X') along Y'=0 line.

3.2 Planar PIV setup

Four PIV cameras are instantaneously capturing the flow velocity field in a wide region upstream and downstream of the detachment point. The PIV cameras are 2048×2048 pix (7.4 µm×7.4 µm) 14 bit CCD cameras (Imager ProX 4M, LaVision GmbH)). The cameras are placed under the water channel and they are looking at the plane vertically using 45-degree oriented mirrors as shown in Figure 3.2 (a). The FOV of each camera is set in a configuration to be side by side with certain amount of overlaps to facilitate stitching of the four flow fields. The cameras are equipped with 105 mm SLR lens at aperture setting of *f*#/11, where *f*# is the aperture setting defined as *f*/*D,* where *f* is the focal length of the lens and *D* is the lens aperture. The depth of field (DOF), which is the distance range that the particles are in focus, can be estimated as

$$\mathrm{DOF} = 4(1+\frac{1}{M})^2 f\#^2 \lambda \tag{3.1}$$

where *M* is the magnification and λ is the wavelength of the laser beam. For this setup DOF is estimated 12 mm. The depth of focus of the imaging system represents the tolerance of the displacement of image plane in the camera that can produce in focus image. The depth of focus can be calculated as

$$t = 2(1+M)f\#c \tag{3.2}$$

where *t* is the total depth of focus and *c* is the circle of confusion, which can be estimated as *f*/1000 (Raffel et al. 2013). Therefore, the total depth of focus is estimated as 3.4 mm.

The magnifications of the cameras and their digital resolutions are tabulated in Table 3.1 for the camera located upstream (camera 1) to the one at the downstream (camera 4) respectively. The FOV for each camera is about 75×75 mm^2, but it varies slightly from one camera to another. The digital resolution is about 27 pix/mm. The entire FOV covers 240 mm of the wall in streamwise direction and 66 mm in wall-normal direction.

Table 3.1 Magnifications and digital resolutions of cameras.

	Magnification	Digital resolution (pix/mm)
Camera 1	0.0370	27.3
Camera 2	0.0374	27.6
Camera 3	0.0372	27.5
Camera 4	0.0368	27.2

The flume was seeded with 2 μm silver-coated spherical glass particles (SG02S40, Potters Industries) with the density of ρ_p (=4,000 kg/m^3). As the density of the particles is higher than the fluid density ρ_p (=1,000 kg/m^3), the particles settle down in the channel. This settling velocity, V_s, causes relative velocity between the flow velocity and particle velocity, resulting uncertainty in the velocity measurement (Raffel et al. 2013). To estimate V_s, Stokes' equation is used, and by assuming particles as spheres, V_s can be calculated as:

$$V_s = d_p^2 \frac{(\rho_p - \rho_f)}{18\mu} g \tag{3.3}$$

where g is gravitational acceleration, μ is the dynamic viscosity of the fluid and d_p is the diameter of the particles (Raffel et al. 2013). Therefore, for this setup, V_s is calculated as 3.3×10^{-6} m/s, which is significantly smaller than the uncertainties of velocity calculation as it will be discussed in this section; and therefore, it can be safely ignored (Prasad 2000). For this PIV setup, the diameter of the particles considering diffraction effect is theoretically about 3 pix while particles with diameter of 2 to 4 pix are visible in the PIV images. This is an optimized size of particle images for PIV measurements as suggested by Raffel et al. (2013).

The laser system (Spectra-Physics, PIV400) provides a horizontal laser sheet in order to illuminate seeding particles in the FOV as shown in Figure 3.2 (a). The laser sheet is ~1 mm thick and ~ 300 mm wide, generated by a combination of spherical and cylindrical lenses. The laser beam has λ of 532 nm with the maximum output power of 400 mJ per pulse. Two mirrors are used to redirect the laser beam and set it horizontally at the measurement region. The laser sheet and FOV are located 260 mm above the bottom of the channel (almost at the middle of plate). The time separation between two laser pulses is 2 ms and the data acquisition is performed at 2 Hz frequency. The cameras and the laser system are synchronized using a programmable timing unit (PTU9, LaVision GmnH). An ensemble of 7,000 double images is captured for each camera to provide data convergence. This number of images provides satisfactory convergence of streamwise and wall-normal velocity as will be discussed in section 3.2.1.

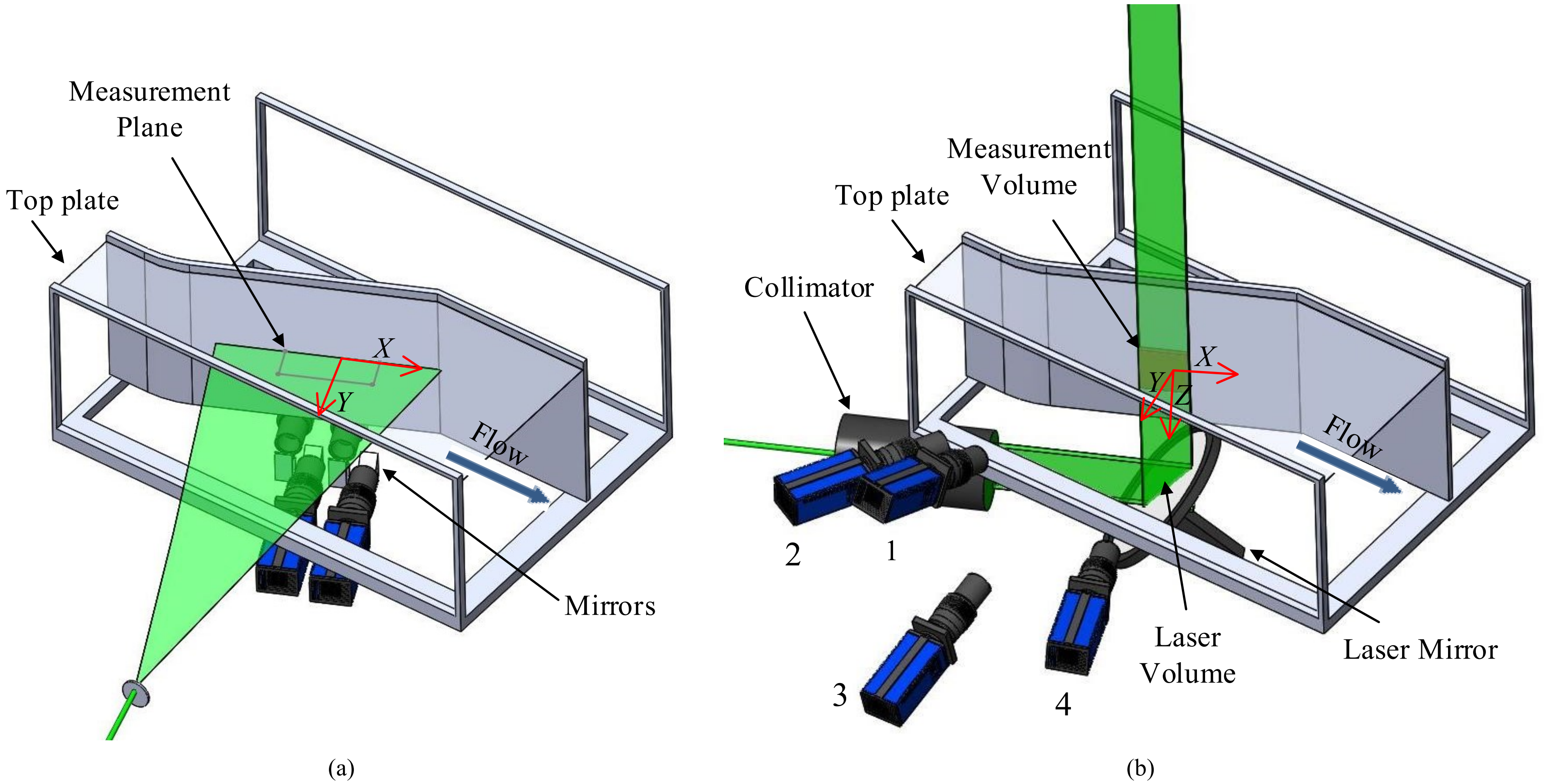

Figure 3.2 Planar and Tomo-PIV Camera setup parts: (a) Planar setup including a breadboard, mirror mounts, and cameras installed under the water channel (b) Tomo-PIV setup including collimator, mirror, and cameras installed at the side of the channel window.

To improve the signal-to-noise ratio in the near-wall region, the minimum intensity of the ensemble of images is subtracted from the individual images, followed by normalizing the images by the average of the ensemble. The double-frame images are cross-correlated in DaVis 8.3 (LaVision, GmbH) using a multi windows algorithm with final window size of 32×32 pix (1.18×1.18 mm^2) with 75 % overlap. A summary of the specifications of the PIV system is provided in Table 3.2.

Table 3.2. Specifications of PIV measurement for both planar and tomographic PIV.

	2D-PIV	Tomo-PIV
Data set	7,000	1,500
Magnification	0.0370	0.0336
Digital resolution	27 pix/mm	30.1 pix/mm
Δt (μs)	2,000	5,000
Measurement field dimensions (x,y,z)	240×65 mm^2 6480×1755 pix	75×12×70 mm^2 2258×361×2107 voxel
Vector calculation method	double-frame correlation	double-frame correlation
Final window sizes	32×32 pix	48×48×48 voxel
Window overlap	75 %	75 %

In order to stitch the simultaneously captured velocity fields of the four side-by-side PIV cameras, images of a printed calibration target that covers almost the entire FOV are used to find the relative locations of the field-of-view of the four cameras. The target marks have the diameter of 2.7 mm with spacing of 6.38 mm. The optical and perspective distortions of the images are corrected using the calibration target images, and the magnifications of the images are determined. The relative locations of the camera views are used to stitch the velocity vector fields. A MATLAB code written by the author improves the quality of the stitching by applying rotation and linear scaling using cross-correlating of velocity vectors as presented in section 4.1.

3.2.1 Measurement uncertainties

Uncertainties regarding vector calculation can be estimated using the maximum 0.1 pix error associated with calculating the location of the center of the particle for particle displacements of less than 10 pix as described by Westerweel et al. 1997. This error results in 2×10^{-3} m/s error in calculating flow velocity, which is around 0.6% of free-stream velocity. This error increases very close to the wall and the shear layer, where flow velocity has magnitudes around 0.01 m/s. For this case, the RMS of the error is around 0.05 pix, which results in the maximum error of 10% of the velocity magnitude.

Stitching of the four vector fields captured by the cameras also imposes errors in the overlap regions of the fields. Maximum difference between the velocity magnitudes of two neighbor flow fields in the overlap region is found to be 6×10^{-3} m/s, which occurs at the overlap region of cameras 3 and 4 at their mid-height field. Comparing this error with local average velocity magnitude at this point, stitching error is 4.2 % of the local velocity. Close to the wall, due to low magnitude of velocity, this error reaches to the maximum of 6 %. The velocity differences vary from one vector field to another. The maximum standard deviation of the velocity differences in the whole FOV is 0.067 m/s as calculated in section 4.1.3. Concerning whether the movements of particles accurately represent the flow velocity, as we discussed before, the associated uncertainty due to the settling velocity of particles is 3.3×10^{-6} m/s, which is negligible to the magnitude of velocity investigated in this study and less than the error associated with vector calculation.

There are two kinds of error sources, which are errors in photonics measurement system components and errors in the components of the setup.

Error sources associated with optical components and measurement procedure can be summarized as follow:

- Increase of noise due to changes in temperature of the camera sensor
- Misalignment of the laser sheet and camera field of view
- Misalignment of laser pulses

- Vibration of camera or laser
- Noises of other light sources rather than laser
- Optical defects and distortion

Error sources related to the setup components can be summarized as follow:

- The vibration of the water channel when it operates at low flow rate
- Reflection of the water surface, which results in background noise in the particle images
- Unknown particles in the water, which might not follow the flow faithfully and change correlation function
- Non-uniform distribution of tracer particles
- Fluctuations in water flow rate (week flow rate control)
- Deviation of the laser sheet or the focus plane from perpendicular position with respect to the plates

In order to confirm that the number of the acquired flow fields provide us satisfactory statistical convergence, the convergence of U and V is investigated by monitoring the average of U and V using N flow fields denoted as $\langle U_N \rangle$ and $\langle V_N \rangle$ respectively. The distributions of $\langle U_N \rangle$ at X=0 and Y=0.05 are plotted as shown in Figure 3.3 (a) and (b) for all the flow fields and the last 1000 flow fields respectively. Similarly, the distributions of $\langle V_N \rangle$ are plotted at X=0 and Y=0.05 as shown in Figure 3.3 (c) and (d) for all the flow fields and the last 1000 flow fields respectively. Same procedure has repeated at a point further away from the wall at X=0 and Y=0.35, and the distributions of $\langle U_N \rangle$ and $\langle V_N \rangle$ are plotted in Figure 3.4.

Close to the wall (X=0 and Y=0.05), considering the last 1000 flow fields, the maximum variation of $\langle U_N \rangle$ from $\langle U \rangle$ is 8×10^{-4} m/s, which is less than 5% of $\langle U \rangle$ as shown in Figure 3.3 (b). This variation is 8×10^{-4} m/s for $\langle V_N \rangle$ at the same location, although as $\langle V \rangle$ also has small magnitude, this variation is 25% of $\langle V \rangle$ as shown in Figure 3.3 (d). Further away from the wall, this variation is less than 0.3% of $<U>$ and less than 0.7% of $<V>$ as shown for last 1000 flow fields in Figure 3.4 (b) and (d).

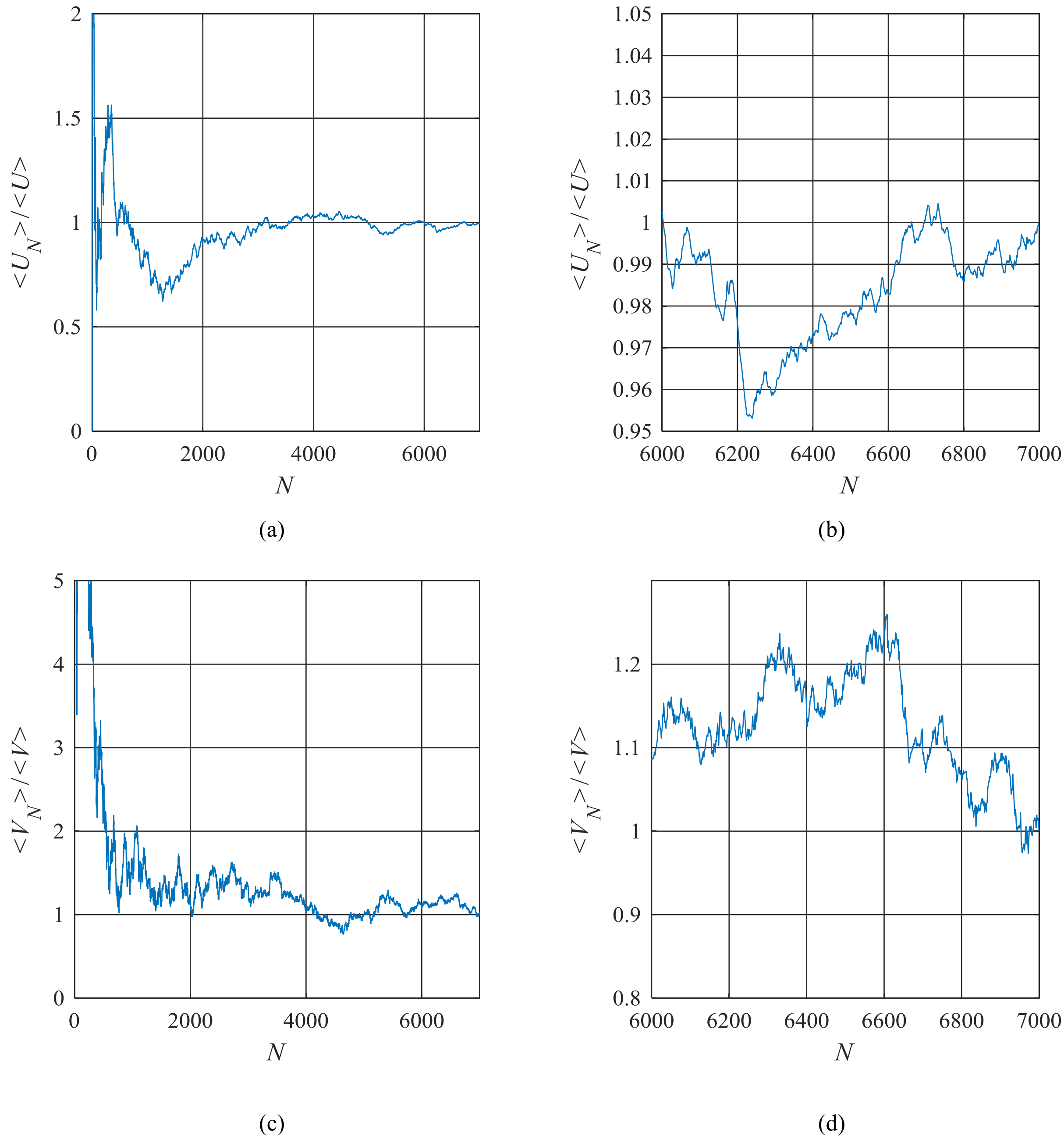

Figure 3.3: The convergence analysis of mean streamwise and wall-normal velocities at X=0 and Y=0.05. (a) convergence plot of mean streamwise velocity for 7000 images, (b): convergence plot of mean streamwise velocity at last 1000 images, (c) convergence plot of mean wall-normal velocity for 7000 images, (b): convergence plot of mean wall-normal velocity at last 1000 images.

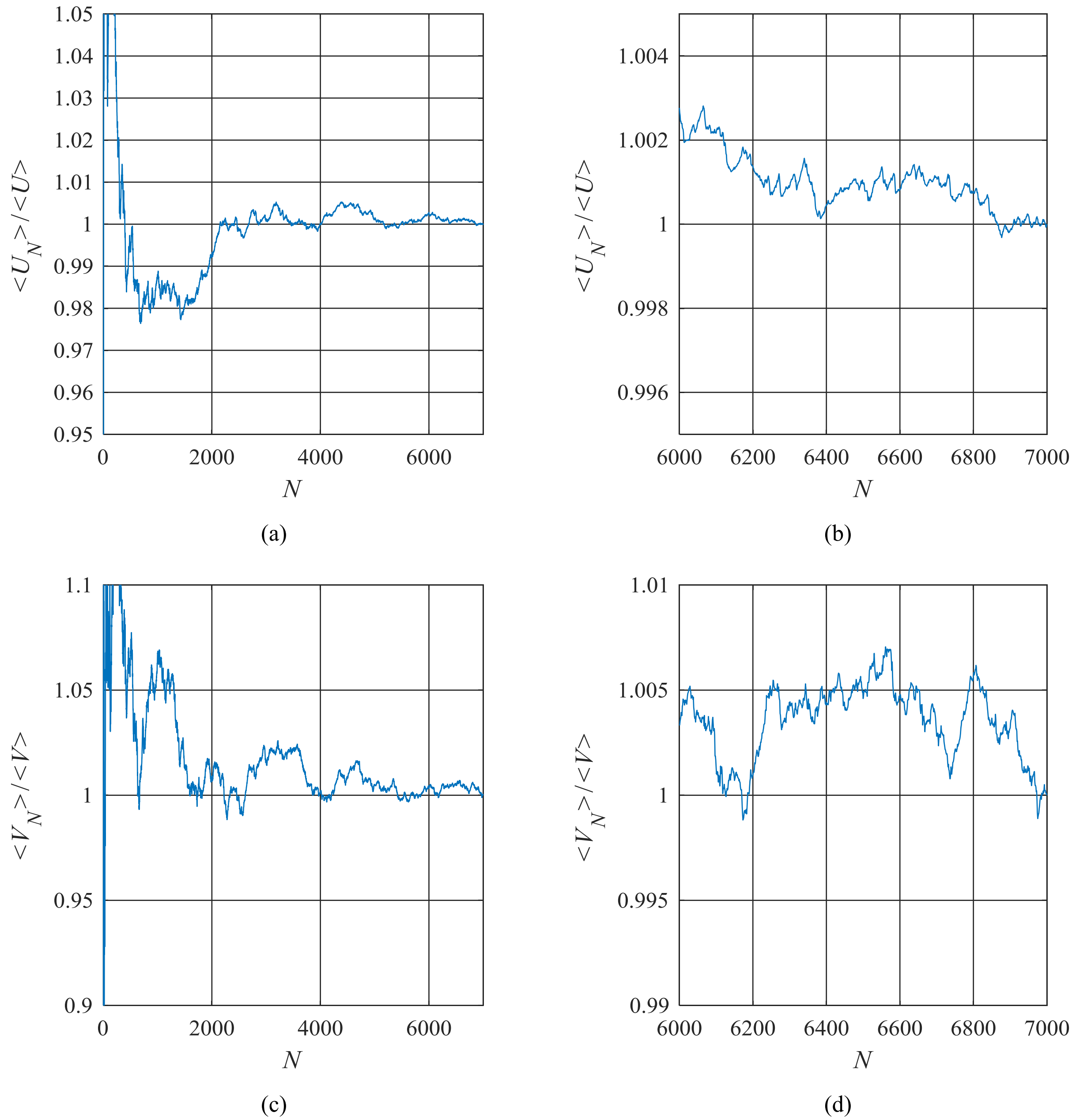

Figure 3.4: The convergence analysis of mean streamwise and wall-normal velocities at X=0 and Y=0.35. (a) convergence plot of mean streamwise velocity for 7000 images, (b): convergence plot of mean streamwise velocity at last 1000 images, (c) convergence plot of mean wall-normal velocity for 7000 images, (b): convergence plot of mean wall-normal velocity at last 1000 images.

3.3 Tomographic PIV setup

Tomographic PIV (Tomo-PIV) is a 3D technique to measure the velocity field in a 3D volume by reconstructing the tracer images in the volume and doing 3D cross-correlation. Using this method one can measure three components of velocity in a volume and provide a good understanding of turbulent structures and flow properties. The flow configuration is the same as the planar PIV experiment. The origin of the coordinate system (X, Y, Z) used in Tomo-PIV is aligned with the center of a large vortex that appears in the mean flow field where $\partial <U>/\partial X$ and $\partial <W>/\partial Z$ are zero where W is the spanwise component of velocity. Figure 3.2 (b) shows the orientation of the cameras and the laser volume. Same PIV cameras and 105 mm SLR lenses used for planar PIV measurement are used here. The cameras are installed in a cross-like orientation as described by (Scarano et al. 2012). The angle between the wall-normal axis and the camera views are approximated based on the calibration and the pin-hole model implemented in DaVis 8.3, and they are 17°, 39°, 10°, and 31° for cameras 1 to 4, respectively. Two of the cameras with highest view angles are looking through water filled prisms installed on the water channel glass wall to reduce astigmatism effects. Scheimpflug adapters are used to tilt the camera lenses to align the depth-of-field with the laser sheet. Similar to planar PIV measurements, 105-mm SLR lenses provide proper magnification (0.0336) and FOV of 75×69 mm^2 for this experiment. The aperture of the Camera 1 lens is set at *f*#/16, which is the camera capturing backward scattering, and *f*#/22 for rest of the cameras. The depth-of-field considering the camera with *f*#/16 aperture is 22.8 mm, which encompasses the entire laser volume making all illuminated particles in focus. The digital resolution is 27.3 voxel/mm (30.1 pix/mm), and the measurement volume has the size of 0.45×0.073×0.42 in (X, Y, Z) as shown in Figure 3.2 (b).

A 3D calibration target (LaVision, Type 11) is used for initial calibration. The target has two parallel planes with 2 mm offset, and 2.2 mm diameter dots are spaced 10 mm. The target is traversed in four 2 mm steps in the Y direction. The pinhole- model fit implemented in DaVis 8.3 is used to find a mapping function between the image space and the physical three-dimensional space. The disparity map for residual root-mean-square (RMS) of the image distortion shows the maximum initial distortion of 2.5 pix. This error can be due to slight movements of the cameras or errors in the calculated mapping function. In order to improve the mapping function, particle images are processed using volume-self-calibration technique (Wieneke et al. 2008). The individual particles are detected in 2D particle images, and by triangulation of the 3D position of the particles in space and calculating residual triangulation errors (disparities), the mapping function has improved through DaVis 8.3. Several volume-self-calibrations were applied using DaVis 8.3 to make the distortion errors less than 0.1 pix, which is a tolerable error (Wieneke et al. 2008).

The same laser system as the one used for planar PIV is used to generate a 12-mm thick laser volume in the test section with the width of about 100 mm using a collimator system and cylindrical lenses (LaVision GmbH). The laser light is emitted vertically from the bottom of the channel through the bottom glass window and illuminates particles close to the wall as shown in Figure 3.2 (b). The laser volume almost touches the wall at the measurement region and illuminates particles within the first 12-mm region starting from the wall according to the profile of laser intensity in this volume implemented in DaVis 8.3. Four knife-edge filters are installed at the bottom glass wall of the channel to block low-energy regions of the laser volume (four edges of the cross-section) to provide high energy and almost uniform laser intensity throughout the laser volume. The laser intensity drops at the edges of the volume as it is expected and implemented by the knife edges. Laser intensity profile shows the signal-to-noise ratio of 1.36. The cameras are synchronized with the laser system using a programmable timing unit (LaVision, GmbH). The same seeding particles used for planar PIV measurement are used here. The diameter of particles is between 3 pix to 6 pix in the particle images. Same seeding particles are used with concentration of about 0.05 particle per pix (ppp). This concentration of particles provides a satisfactory reconstruction quality (Elsinga et al. 2006). The source density (N_s) is determined as 0.31, which is slightly higher than the upper limit of 0.3 proposed by Novara et al. (2010) for high precision image processing. De Silva et al. (2012) proposed an optimum particle number by defining the number of particles in interrogation windows normalized by the window volume size (S_d). Considering last interrogation window of 48×48×48 voxel for this measurement setup, S_d is determined 2.26×10^{-4}, which is close to the reported optimum value of 1.4×10^{-4}.

In addition to subtraction of the minimum intensity of the ensemble of images to increase signal-to-noise ratio, local subtraction of minimum intensity with kernel of 50 pix, and local averaging of the signal over 50 pix are applied. The volume reconstruction is performed using MART algorithm (Herman and Lent 1976) using Davis 8.3. Subsequently, volumetric cross-correlation with multiple window sizes is performed. The size of the final window is 48×48×48 voxel (1.59×1.59×1.59 mm^3 or 0.0096×0.0096×0.0096) with 75 % overlap. Finally, calculated vector fields are further processed to remove miscalculated vectors using the universal outlier detection (Westerweel and Scarano 2005). The number of particles per interrogation volume is about 3.8 particles.

3.3.1 Measurement uncertainties

To calculate the uncertainty involved in the calculation of the velocity field, the standard deviation of the velocity divergence ($\varepsilon = \sigma\ [\nabla.\boldsymbol{V}]$) is calculated as suggested by Scarano and Poelma (2009). They reported a Gaussian width of 0.005 voxel/voxel for ε distribution (Scarano and Poelma 2009). For current setup, ε is about 1.0×10^{-2} voxel/voxel as calculated and averaged for several flow fields. The Gaussian width of the error distribution is 0.0015 voxel/voxel. Comparing calculated uncertainty with other Tomo-PIV measurements, Kim et al. (2013) performed high resolution Tomo-PIV experiments on a confined liquid droplet and reported ε = 0.025 voxel/voxel uncertainty. Atkinson et al. (2011) investigated on accuracy of Tomo-PIV measurements in TBLs and reported ε = 0.05 voxel/voxel as a satisfactory uncertainty.

Similar to planar PIV measurement, the uncertainty in the tomographic mean flow velocity is investigated here by investigating the convergence of $\langle U\rangle$, $\langle V\rangle$ and $\langle W\rangle$ close to the wall at X=0.1, Y=0.01 and Z=0.1. Parameters $\langle U_N\rangle$, $\langle V_N\rangle$ and $\langle W_N\rangle$ are assigned here to present the average components of velocity calculated using N flow fields as shown in Figure 3.5. Figure 3.5 (a) shows that for $\langle U_N\rangle$, the uncertainty for last 500 flow fields is less than 20% of $\langle U\rangle$, which is less than 4.2×10^{-4} m/s. This uncertainty for $\langle W_N\rangle$ is less than 30% of $\langle W\rangle$, which is less than 8.1×10^{-4} m/s, and for $\langle V_N\rangle$, because of very low magnitude of $\langle V\rangle$ (=6.6×10^{-5} m/s), $\langle V_N \rangle$ has not converged very close to the wall (Y=0.01) as shown in Figure 3.5 (c). However, away from the wall at X=0.1, Y=0.06 and Z=0.1, $\langle V_N \rangle$ shows better convergence pattern as shown in Figure 3.5 (d).

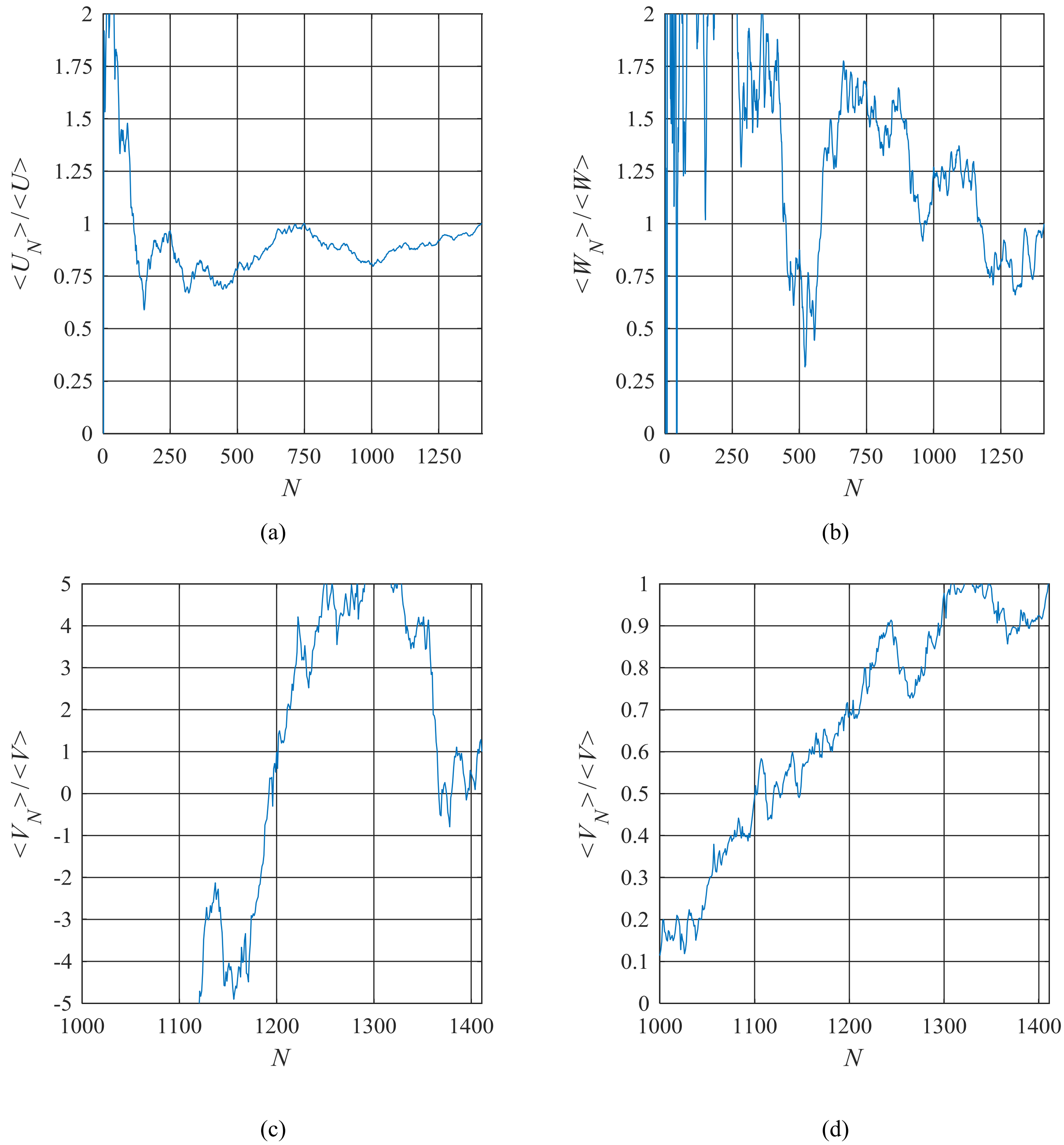

Figure 3.5 The convergence analysis of mean streamwise, wall-normal and spanwise velocities. (a) convergence plot of mean streamwise velocity for 7000 flow fields at X=0.1, Y=0.01 and Z=0.1. (b) convergence plot of mean spanwise velocity at X=0.1, Y=0.01 and Z=0.1 for 7000 flow fields. (c) convergence plot of mean wall-normal velocity at X=0.1, Y=0.01 and Z=0.1.(d) convergence plot of mean wall-normal velocity at X=0.1, Y=0.06 and Z=0.1.

3.4 Conclusion

In summary, the flow setup and PIV measurement setups are described in this chapter. The measurement channel provides a region with APG, which causes the flow separates from the wall of the diffuser. Planar PIV setup contains four PIV cameras capturing images along the wall of the diffuser in a large FOV with overlaps of four fields of view. The flow fields captured by the four cameras are stitched together using images captured from a large dotted target. Tomo-PIV setup also contains four PIV cameras and it provides three-dimensional flow velocity field close to the detachment point.

Chapter 4 Data analysis

In this chapter, the preformed data analyses of this study are presented. First, the procedure for stitching planar fields of view is explained and evaluated, and second, the conditional averaging, POD and quadrant analysis applied for data reduction are discussed.

4.1 Vector Stitching Procedure

The simultaneously acquired velocity fields of the four side-by-side PIV cameras are stitched to obtain the velocity field over the entire measurement domain. The images of a calibration target that cover almost the entire FOV are used to find the relative locations of the four camera FOVs. In addition, the optical and perspective distortions of the images are corrected, and the actual dimensions of the images are determined. The relative locations of the camera views from the previous step are used to stitch the velocity vector fields. A MATLAB code written by the author improves the quality of the stitching using cross-correlating of velocity vectors. The concepts used in the MATLAB code are presented here. Finally, an error analysis is performed to investigate the uncertainties involved in the results of the stitched flow fields.

4.1.1 Image Correction using Target Images

The images of a two-dimensional target aligned with the laser sheet plane are used to correct possible perspective and optical distortions applying DaVis 8.3. The marks on the calibration target are detected, and the pinhole camera model fit implemented in DaVis 8.3 is used to correct possible optical and perspective distortions. In addition, images are rotated in the way that their vertical and horizontal axes align with the grid coordinate system, which is detected and defined based on the orientation of the marks. Therefore, all the image frames and the target grid coordinate have the same orientation using DaVis 8.3. The mark detection and the explained corrections on one image sample is shown in Figure 4.1. The magnifications and the actual dimensions of all the images are determined based on the properties of the calibration target and assigned to all the images through DaVis 8.3. To apply the corrections in DaVis 8.3, first the calibration option is selected for the raw images. In the new window, the first step of calibration appears, which provides the options named ‘define origin, maintain calibration’, ‘1 camera (2D)’, ‘2 cameras (independent 2D+2D)’, ‘2 cameras (mapped, e.g. stereo)’, and ‘advance setting’. The ‘advance settings’ is selected. In the second step, one plane and one view are assigned to the coordinate system as the target is a flat plate (one plane) and only one view of the target is used for each camera. In the third step, the properties of the used target are assigned to a new defined target because it is not among the available conventional targets suggested by DaVis 8.3. Step four loads target images by finding their address. Three neighbor marks are selected manually in step five. Step six detects the marks of the target images according to the initially selected marks automatically. A fit mapping function is calculated in step 7. The rotation and perspective corrections are corrected using the grid coordinate system as mentioned before in step 8. Finally, the calculated corrections can be applied to all of the raw images at the final step.

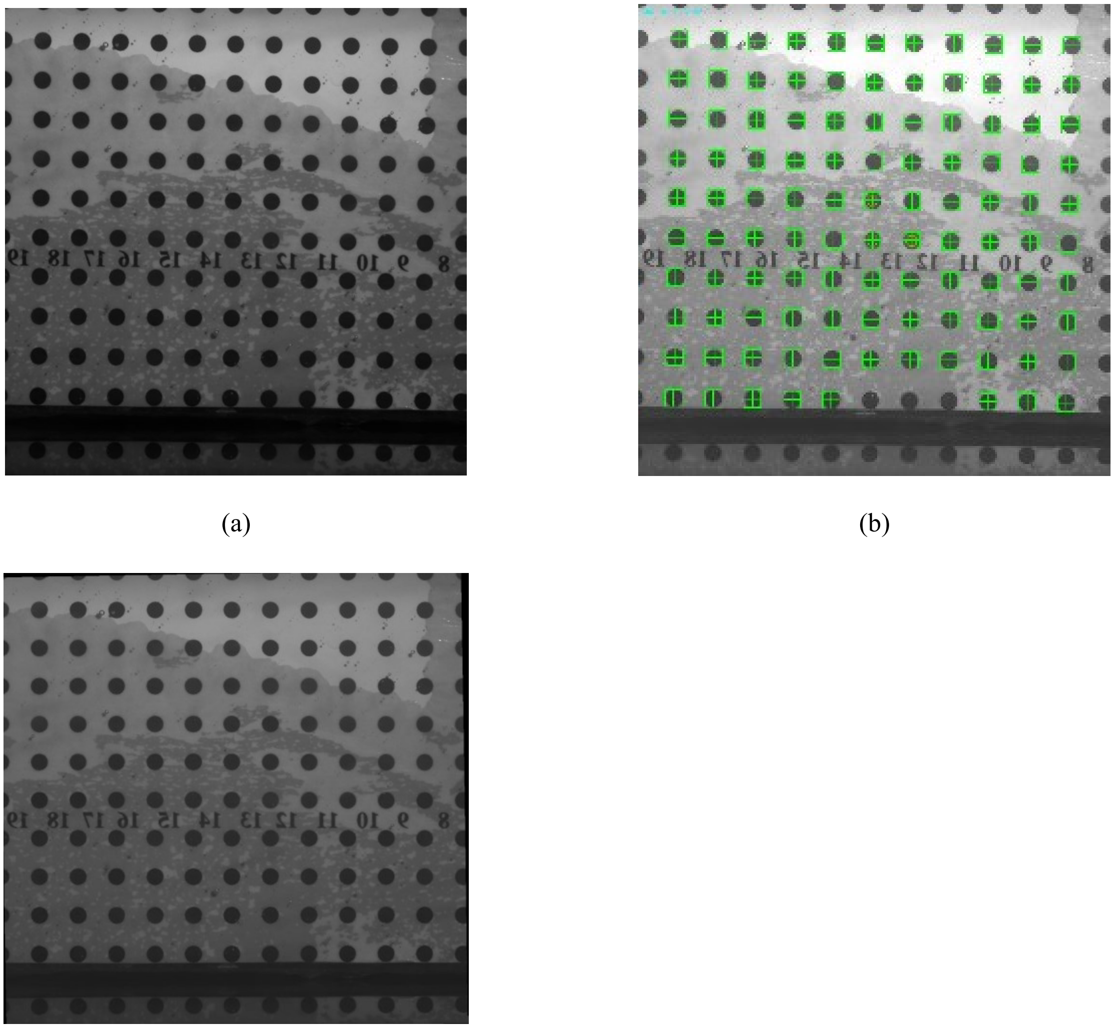

(a) (b)

(c)

Figure 4.1 The correction process of a target image (a) The original image of the target plate (b) Mark detection (c) The corrected image. The corrected image has slightly rotated counter clockwise (as the dark region in the top-right corner of figure (c) shows it) in a way that the horizontal and vertical axes of the image align with the coordinate of the marks.

After applying the corrections, the perspective distortion and other possible distortions are improved, and target images are stitched together by matching common target marks in the overlap regions. The result of the stitching is shown in Figure 4.2. As the images almost perfectly match visually at the overlap regions in Figure 4.2, it is concluded that the relative locations of the four camera frameworks are accurate, and they are used for stitching of the velocity vector fields.

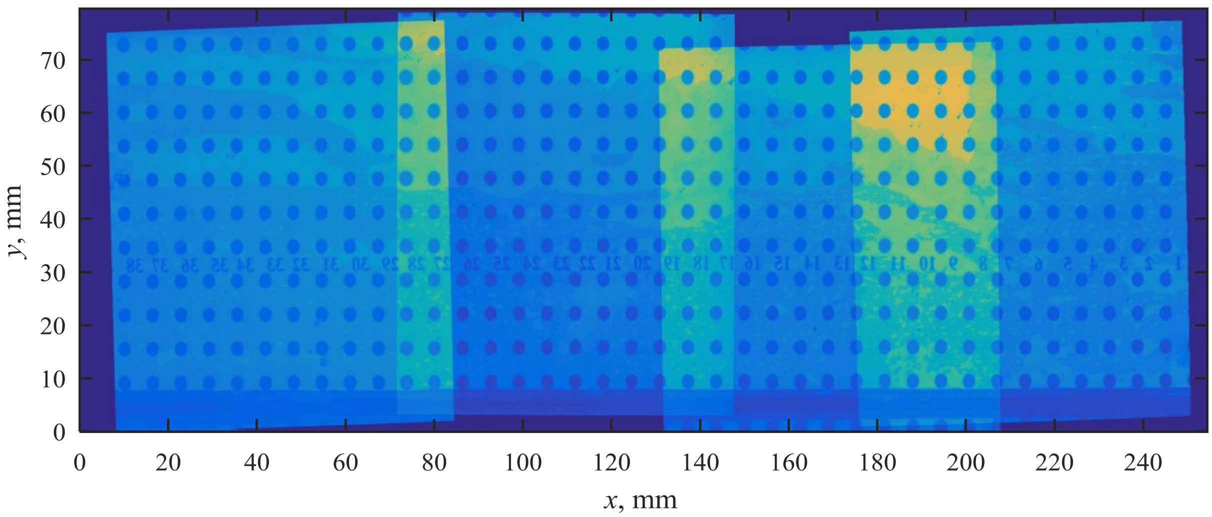

Figure 4.2 The image of the entire target is made by stitching of four images captured by four cameras. The images have a good alignment at the overlap regions.

4.1.2 Velocity field stitching

In order to stitch the velocity fields, the perspective corrections and rotations applied to the target images are applied to the raw images (particle images). Then the results are processed by DaVis 8.3 to calculate the velocity fields. Figure 4.3 shows camera 1 velocity flow field after performing the perspective corrections and calibration.

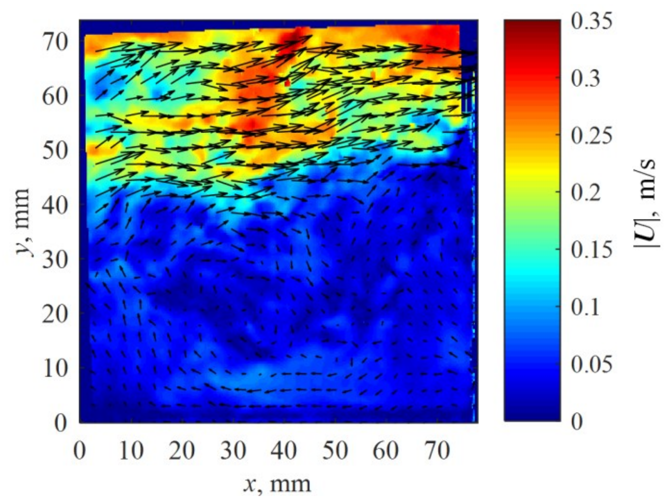

Figure 4.3Velocity field captured by camera 1 after applying perspective and coordinate corrections.

The average streamwise and wall-normal velocities are shown by $\langle U \rangle$ and $\langle V \rangle$ respectively. DaVis 8.3 assigns spatial locations to each vector in the velocity fields. Using the actual locations of the common marks found in the previous section for each camera view, and by matching the locations of the common marks in the neighbor velocity fields and finding the relative locations of the velocity fields, the four velocity fields are stitched. The result of the stitching of one velocity field and average velocity field is shown in Figure 4.4 (a) and (b), respectively. The background contours represents of the magnitude of velocity ($|\boldsymbol{U}| = (\langle U \rangle^2 + \langle V \rangle^2)^{1/2}$). The red arrows indicate the borders between the neighbor velocity fields where the source of velocity values switches from one camera to the next one.

There are still minor misalignments at the stitched borders as they are visible in Figure 4.4. This can be due to perspective and optical distortions, which are not corrected by the previous procedure based on grid calibration. In addition, any misalignment between the laser sheet plane and the target leads to errors and possible mismatches, because the corrections applied according to the target are not same as the corrections required for the particle images. In order to alleviate these errors and improve the stitching results, two interrogation windows with the size of 31×31 pix are selected, which coincides with the center of a common target mark in the overlap region.

One window is selected in the velocity field of the camera 1, and the other is selected in the velocity field of camera 2, both corresponding to a common target mark. Another pair of integration windows is also selected around another common target mark relatively far from the previous mark as shown in Figure 4.5. By selecting these two pairs of interrogation windows and cross-correlating over them, it is possible to apply new corrections to the velocity field of camera 2, which improves the stitching results.

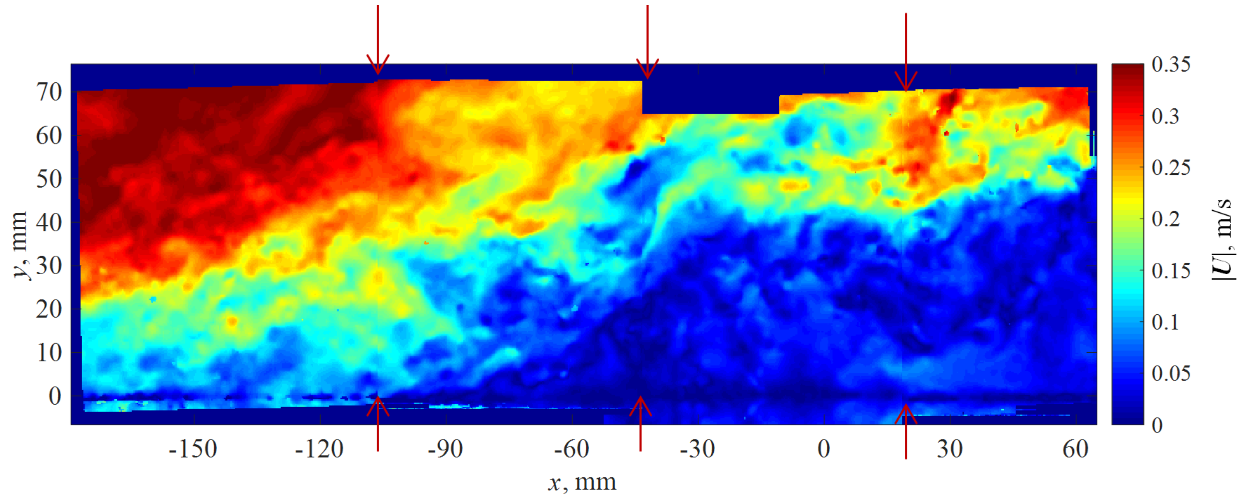

(a)

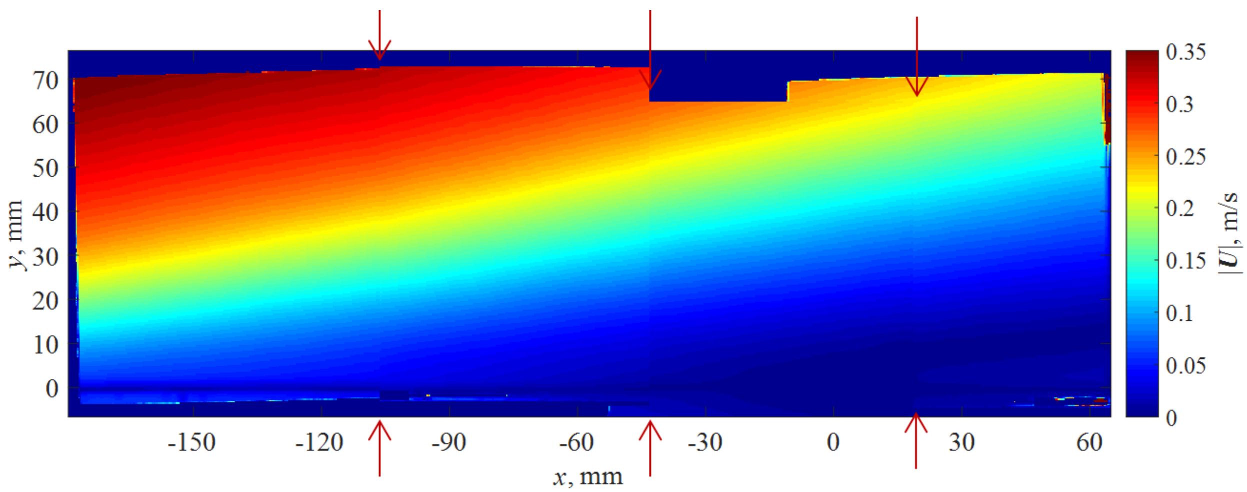

(b)

Figure 4.4 Initial stitching of velocity field for (a) one instantaneous velocity field and (b) average flow field with background contours of $|\boldsymbol{U}|$.

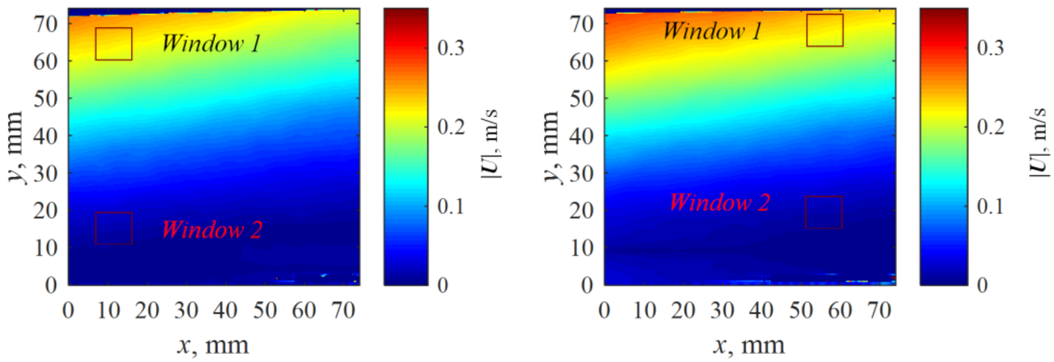

(a) (b)

Figure 4.5 Interrogation windows selected for applying NCC functions are shown in the velocity filed of (a) Camera 1, and (b) Camera 2.

The values of the magnitude of average velocity, $|\boldsymbol{U}|$ (m/s), inside these windows are stored in four matrices, and the normalized cross-correlation (NCC) functions of the two pairs of corresponding matrices are calculated. If the selected common points, which are determined according to the initial stitching, show exact same spatial locations, then the corresponding matrices should include exact same values of $|\boldsymbol{U}|$; therefore, the NCC functions should have the maximum value at the origin. Otherwise, the corresponding selected points do not have exact same spatial locations; therefore, the relative actual distances between the points can be determined using the deviation of the NCC maximum locations from the origin. NCC maps are shown in Figure 4.6. The asymmetry of the NCC maps indicate that the selected windows do not show exact same spatial location, and the dislocations between the peaks of the maps and the centers of the windows show their relative locations as shown in Figure 4.6. Therefore, it is expected that applying further corrections results in symmetric patterns in NCC maps with the peaks located at the center of the windows.

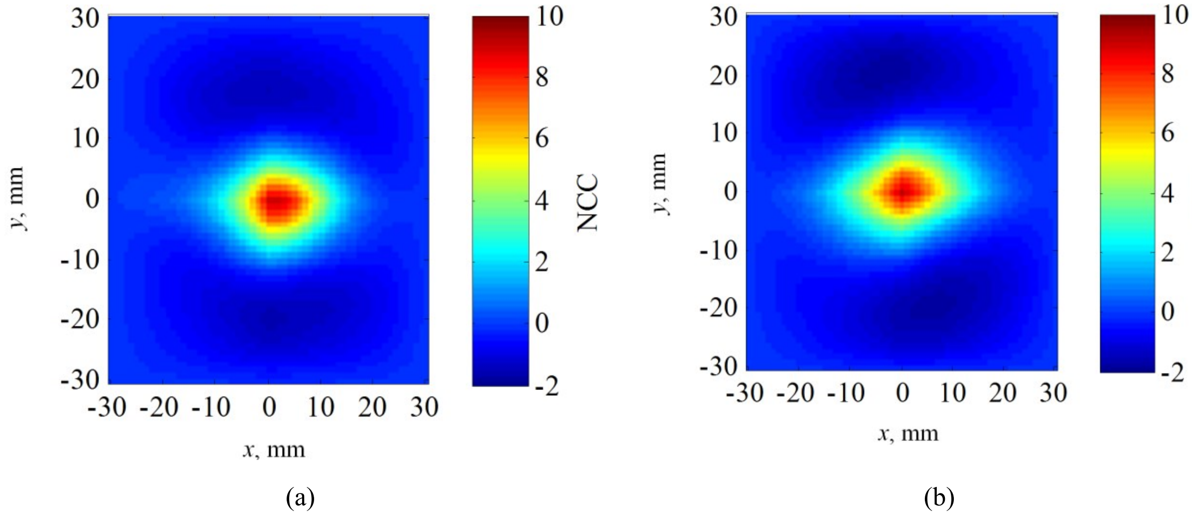

Figure 4.6 Average NCC maps for (a) window 1 (b) window 2 before applying corrections for camera fields 1 and 2.

The relative locations of the interrogation windows are used to improve the stitching and correcting the scale and the orientation of the velocity field of camera 2 in the way that each pair of the interrogation windows shows one spatial location and velocity field. Figure 4.7 shows the center of interrogation windows selected in the velocity field of camera 2 by red plus signs, and the centers of the integration windows moved by the relative locations found by NCC shown by blue crosses. The blue crosses show the locations in the velocity field of camera 2 that the distributions of $|\boldsymbol{U}|$ have the best similarity to the ones within the interrogation windows selected in velocity field of camera 1. In Figure 4.7, a red line connects the window centers selected in the velocity field of camera 2, and a blue line connects the ones moved by the relative distances. The relative distances are exaggerated in this figure for better visibility. In order to correct the camera 2 field and match the window centers, the required values of rotation and scaling of the camera 2 field are the ones required to be applied to the red line to match the blue line.

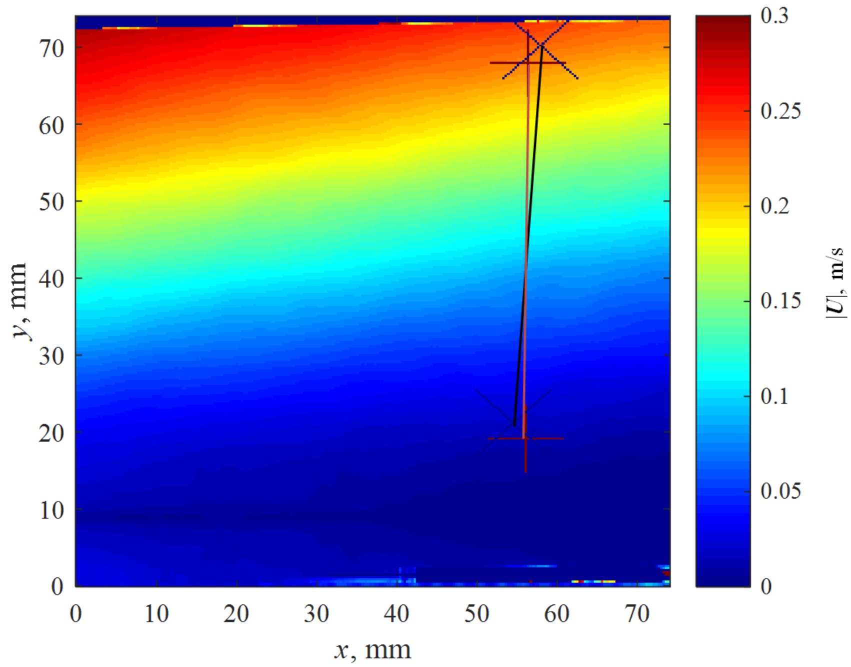

Figure 4.7 The selected interrogation window centers in the flow field of camera 2 (red crosses) and the ones match the interrogation windows selected in the flow field of camera 1 according to NCC (blue crosses). The misalignment between the lines is exaggerated for better visibility.

The same procedure is performed to improve the stitching of field 2 to field 3, and field 3 to field 4. Due to small overlap regions between fields 2 and 3, and fields 3 and 4, the interrogation window sizes of 25×25 pix and 13×13 pix are selected, respectively. Figure 4.8 shows the stitching result after repeating the same procedure to all neighbor fields, and applying the described corrections. The stitching results have been improved as it can be concluded comparing Figure 4.8 and Figure 4.4 at the boundaries of the neighboring fields. The rotation and scaling applied to three consecutives fields corresponding to cameras 2, 3 and 4 are tabulated in Table 4.1.

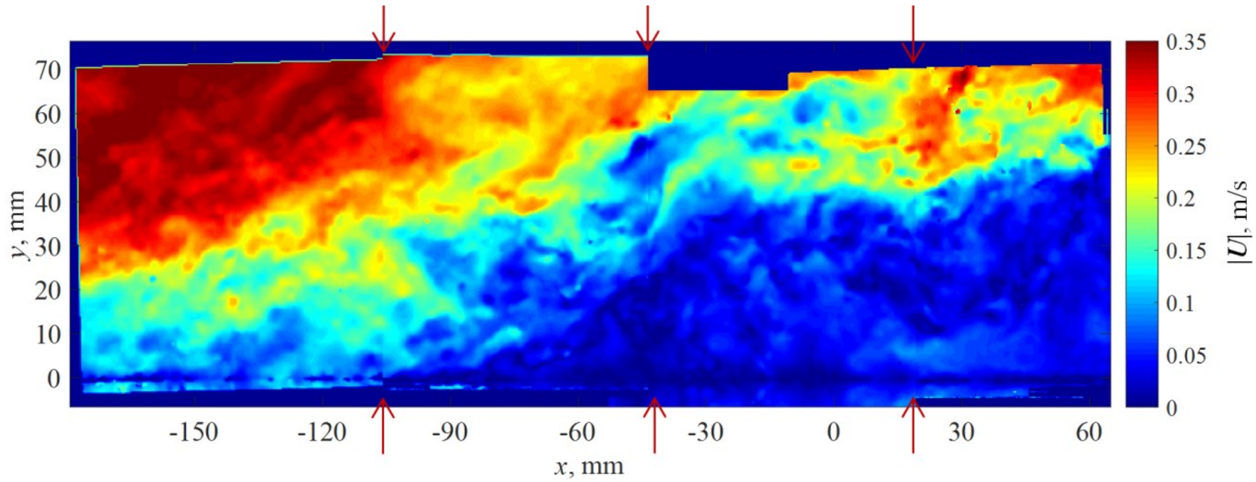

(a)

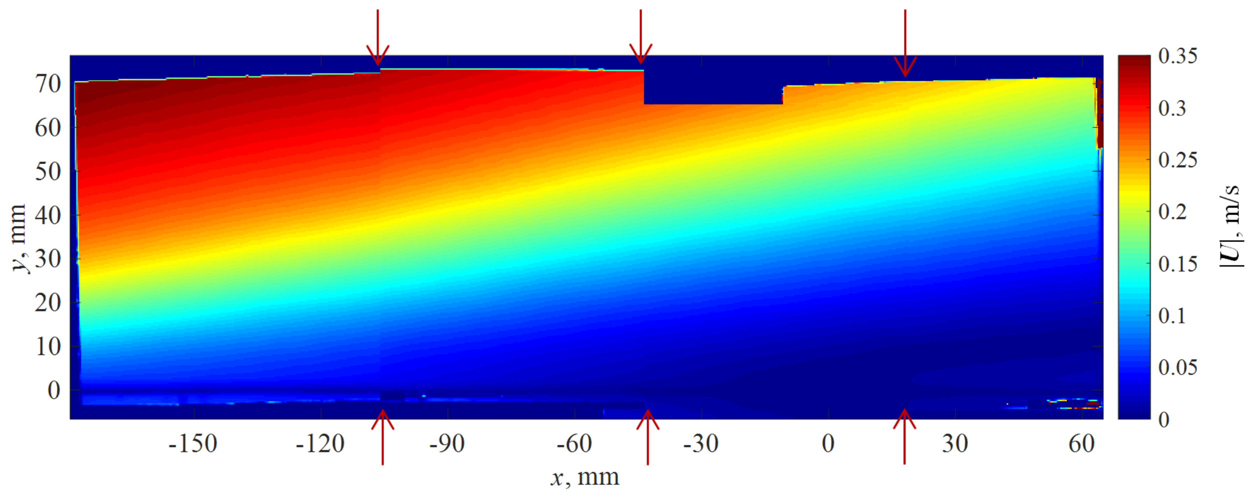

(b)

Figure 4.8 Velocity Magnitude after correction using the cross-correlation method. The red arrows show the boundary lines for (a) instantaneous velocity field, and (b) average field with background contours of $|\boldsymbol{U}|$.

Table 4.1 Rotation and scaling values applied to velocity fields 2, 3, and 4 based on displacements calculated using NCC functions and the procedure explained in Figure 4.7. Positive values of rotation refer to counter clockwise rotations.

	Camera 2	Camera 3	Camera 4
Rotation (Degree)	−1.675	0.130	−0.873
Scaling factor	1.0098	1.0012	1.00011

4.1.3 Validation of stitching and errors

To investigate the accuracy of the stitching results, new interrogation windows are selected in the camera 2, 3 and 4 fields. The same procedure explained in the previous section is followed to find out if the correlation maps have improved (e.g. have become symmetric). Figure 4.9 shows new correlation maps for each pair of windows at the overlap region of field 1 and 2. The maximum values are located almost at the center of the maps, and the correlation maps are more symmetric with respect to horizontal and vertical axes compared to initial NCC maps as shown in Figure 4.6. Therefore, NCC maps indicate that selected windows have a better match after applying the last corrections. According to new NCC functions for window 1, the relative distances are 0.0039 and 0.0159 of the size of the interrogation window elements, e=0.30 mm, (the distance between two neighbor vectors) in y and x directions respectively. For window 2, the relative distances are $1.366\times10^{-5}e$ and $7.342\times10^{-5}e$ in y and x directions. Since these values are significantly smaller than e, it can be concluded that the interrogation windows in fields 1 and 2 have an acceptable match.

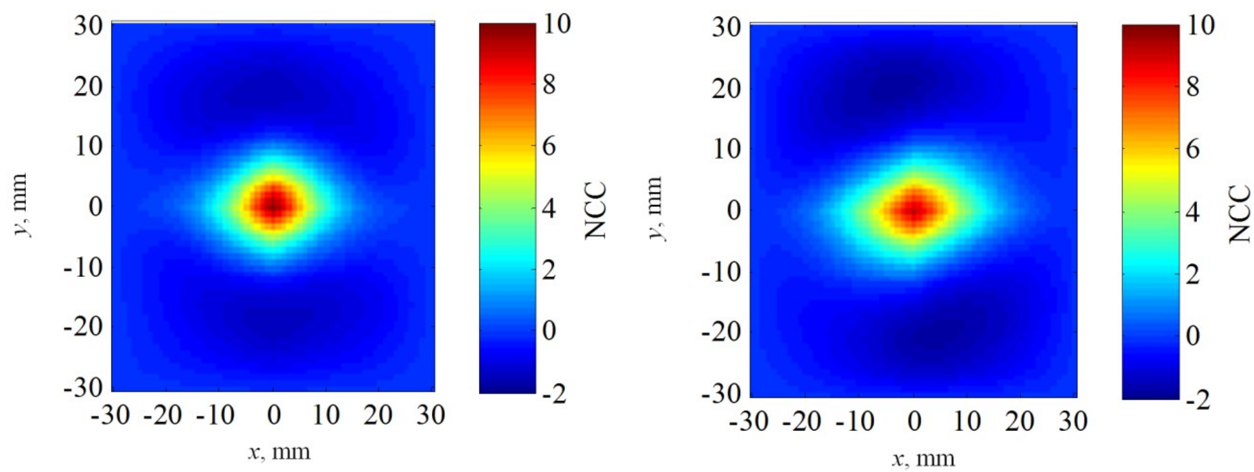

(a) (b)

Figure 4.9 Average NCC maps after applying corrections explained in the previous section and tabulated in Table 4.1 for (a) window 1 and (b) window 2.

The NCC maps for two pairs of windows, which are selected in the overlap regions of fields 2 and 3, and the overlap regions of fields 3 and 4 are provided and explained in Appendix A. The relative distances are found for all the overlaps before and after applying corrections, and tabulated in Table 4.2. Similar to fields 1 and 2, the relative distances calculated by NCC functions for the overlap region of field 2 and 3 and the overlap region of field 3 and 4 are used to calculate the required rotation and scaling for field 3 and 4. After applying the mentioned rotation and scaling, the new relative distances are found to be negligible (Table 4.2), which shows the applied corrections provide better match between the interrogation windows at the overlap regions.

Table 4.2 Relative distances calculated based on NCC functions before and after corrections for interrogation windows at three overlap regions. The relative distances are normalized by the size of interrogation windows, e=0.30 mm. Positive values of Δx show that window 2 located downstream of window 1, and positive values of Δy show window 2 located farther away from the wall compared to window 1.

	$\Delta x/e$ (before corrections)	$\Delta y/e$ (before corrections)	$\Delta x/e$ (after corrections)	$\Delta y/e$ (after corrections)
Window 1 (fields 1 and 2 overlap)	−1.25	−0.196	0.0039	0.0159
Window 2 (fields 1 and 2 overlap)	−0.1688	0.1328	7.342×10^{-5}	1.366×10^{-5}
Window 1 (fields 2 and 3 overlap)	0.1230	0.2628	−0.0726	0.0552
Window 2 (fields 2 and 3 overlap)	0.1073	0.0595	−0.0101	0.1022
Window 1 (fields 3 and 4 overlap)	1.5973	−0.6123	−0.05439	−0.2831
Window 2 (fields 3 and 4 overlap)	−0.4882	−0.5025	−0.04686	−0.1944

In addition, the difference between average velocity values of field 1 and field 2 in the overlap region is investigated by subtracting the values at the overlap region. The velocity difference is defined as $\Delta V_d = (U_2^2 + V_2^2)^{1/2} — (U_1^2 + V_1^2)^{1/2}$, where U and V are flow velocities in streamwise and wall-normal directions for fields 1 and 2 respectively. The subtraction results before and after applying corrections using NCC functions are shown in Figure 4.10 (a) and (b), respectively. The subtraction results illustrate decrease in the velocity difference, and therefore a better match has achieved at the overlap regions as shown in Figure 4.10 (a) and (b). The maximum difference in the overlap regions after applying rotation and scaling is 2.1×10^{-3} m/s, where the average velocity is 8.807×10^{-2} m/s, resulting in 2.4% difference.

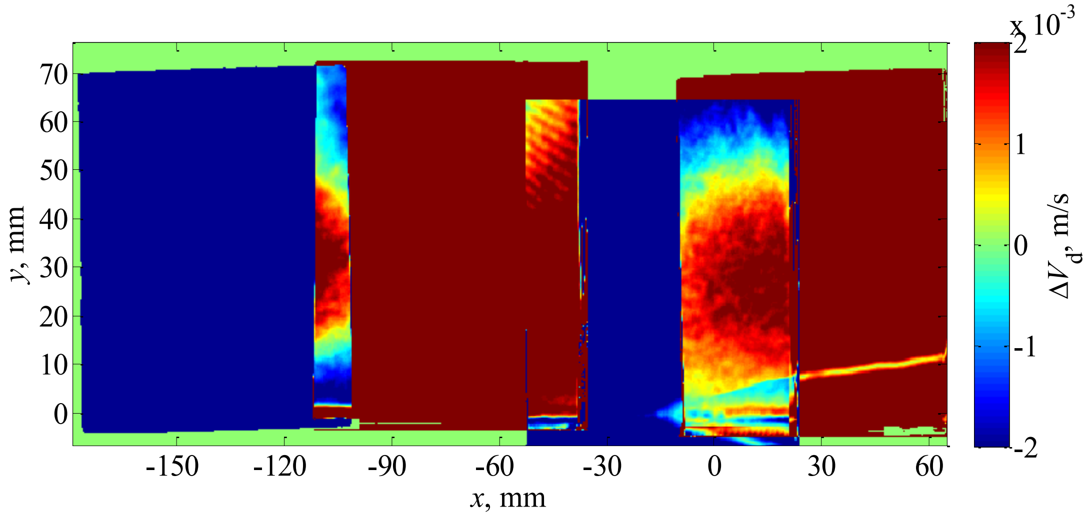

(a)

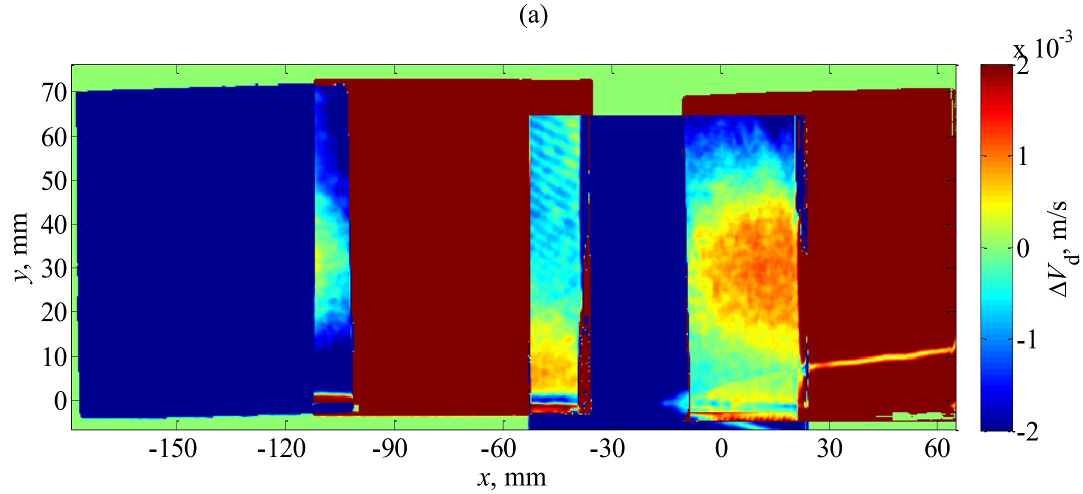

(b)

Figure 4.10 The velocity difference, ΔV_d, in the overlap regions of neighbor cameras calculated (a) before and (b) after applying corrections using NCC functions.

As it can be seen in Figure 4.10 (b), there is no specific trend for the remaining velocity difference. The maximum difference occurs at the midway height and it is smaller close to the wall and the top boundaries in the overlap regions of fields 3 and 4 and fields 1 and 2, and it varies randomly along the wall-normal axis for the overlap region of camera fields 2 and 3. In order to investigate these differences for instantaneous flow velocity, the velocity differences for 500 instantaneous velocity values at 15 points located at overlap regions are calculated as shown in Figure 4.11. The locations of the points and the average of ΔV_d for 500 velocity fields are tabulated in Table 4.3 for the overlap region of fields 1 and 2. The same information for fields 3 and 4 and fields 1 and 2 are provided in Appendix A. Since the selected point 1 is very close to the separation point and the particle displacements are very small, the random error is greater than other points. ΔV_d versus the velocity field number (N) at the 15 mentioned locations are plotted in Appendix A.

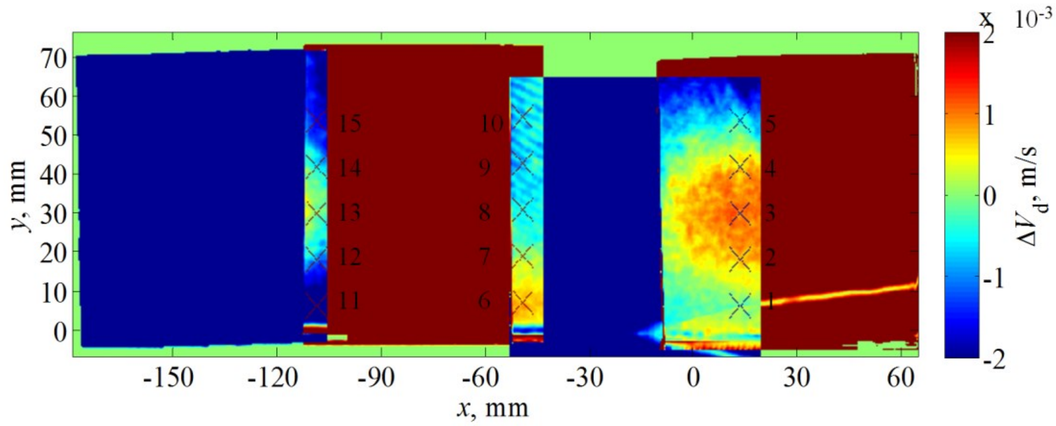

Figure 4.11 Locations selected in the overlap regions to investigate the fluctuations of velocity difference, ΔV_d.

Table 4.3 Locations of the monitored points selected in the overlap region of field 1 and 2 with respect to the separation point.

	Separation point	Point 1	Point 2	Point 3	Point 4	Point 5
x (mm)	0	13.9	13.9	13.9	13.9	13.9
y (mm)	0	2.47	14.3	26.0	37.83	49.6
$<\Delta V_d>$ (m/s)		1.6×10^{-4}	7.5×10^{-4}	4.7×10^{-4}	7.4×10^{-4}	0.002
$<\Delta V_d>/<U>$ (%)		6.4	4.1	0.81	0.70	2.0
Standard deviation of $<\Delta V_d>$		0.064	0.061	0.054	0.012	0.011

The magnitude of velocity $|\boldsymbol{U}|$ is plotted versus streamwise location (x) through the lines passing the points 1 to 5 is shown Figure 4.12. The red vertical lines distinguish between the data extracted from different camera fields. As it can be seen, there is no significant change in the magnitude of velocity as the graphs passes the lines and the source of the data points switches from one camera field to the neighbor one. Velocity magnitudes associating with points 1, 2, 3, 4, and 5 are shown by blue, black, yellow, green and red curves respectively.

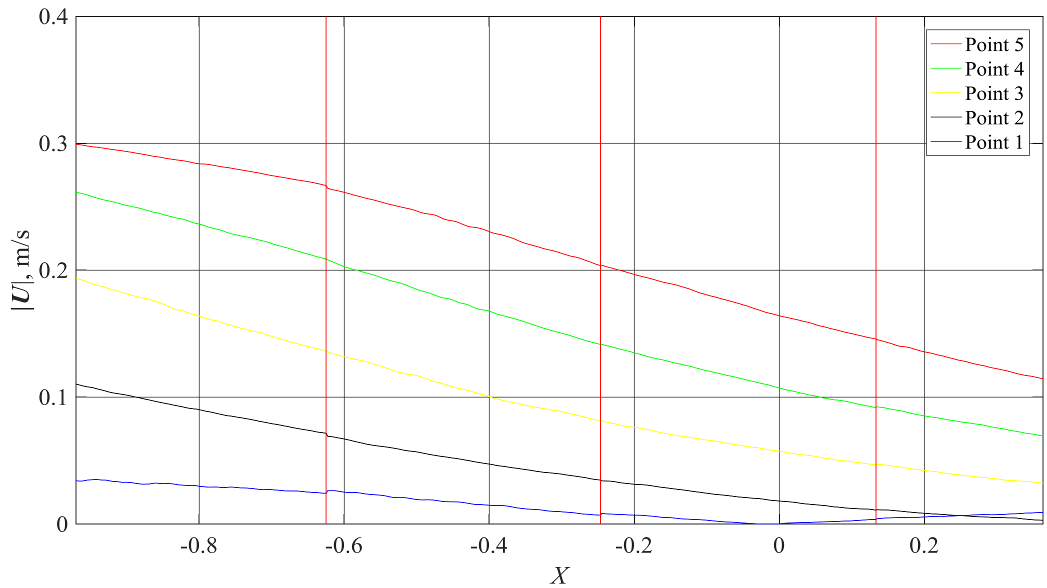

Figure 4.12 Magnitude of average velocity, |***U***|, is plotted versus streamwise location along 5 lines passing different wall-normal locations.

4.2 Conditional averaging

The conditional averaging used in this study has focused on the occurrence and detection of flow detachment in each velocity field, and categorizing the velocity fields based on the status of flow detachment. In this chapter, the mathematical details of the conditional averaging performed in this study are explained and some features of the separated flow have been extracted and described.

4.2.1 Mathematical description

The detection of the velocity fields with instantaneous flow detachments and the location of the detachment front are carried out for conditional averaging analysis. At each streamwise location, X_0, the streamwise velocity component has been averaged inside a box of 0.036H (0.007<Y<0.043) in wall-normal direction and 0.12H (X_0 – 0.06<X_0< X_0 + 0.06) in streamwise direction close to the wall and named as U_W. In the next step, the backward flow at X_0 is defined as

$$U_W = \frac{1}{N} \sum_{x=X_0-0.06}^{x=X_0+0.06} \sum_{y=Y_0-0.043\,H}^{y=Y_0+0.043\,H} U_{x,y} < -0.009\ U_c \tag{4.1}$$

where Y_0=0.025, N=1380 is the total number of data points that were averaged, and $U_{x,y}$ shows streamwise component of velocity, which are within the limits defined in the sums. Similarly, the forward flow is defined as

$$U_W = \frac{1}{N} \sum_{x=X_0-0.06H}^{x=X_0+0.06H} \sum_{y=Y_0-0.043H}^{y=Y_0+0.043H} U_{x,y} > 0.009\ U_{c.} \tag{4.2}$$

Therefore, for each streamwise location, 1380 data points are averaged within the specified range defined in the previous equations to determine whether the flow is attached or detached. The locations for which the sign of this averaged streamwise velocity changes from positive (forward flow) to negative (backward flow) are defined as flow detachments. Similarly, the locations that this sign changes from negative to positive are defined as flow reattachments. Although flow reattachment does not occur in the average field, it has been detected in instantaneous vector fields. Only strong and large structures are detected based on the above criteria as small structures such as small-scale vortices can only locally affect the direction of the flow close to the wall. In addition, setting a threshold helps determine strong gradient of velocity and filters small variations of flow velocity at the locations where the sign of streamwise velocity varies frequently. The selected threshold ($0.009U_c$) is determined by trial and error. Large thresholds limit flow detachment and reattachment to very strong ones, which exist only in few flow fields. Small thresholds would include any small local change in the direction of the flow caused by small-scale structures among flow attachment or reattachment. The goal here is to only capture the larger structures in the flow without filtering most of the flow features.

Figure 4.13 (a) shows the smoothed profile of velocity and the original data points, and Figure 4.13 (b) shows the corresponding flow field and contours of zero velocity. Comparing these figures, it can be seen that the smoothed profile only responses to the flow motions having strong U component of velocity with large span at the wall. Small structures such as vortices can locally affect the direction of the flow close to the wall; however, strong change in the status of the flow is of interest here, which can be mathematically distinguished by averaging the velocity.

Based on these criteria, for any flow field, the properties of the backward or forward motions such as the streamwise extent of them at the wall can be determined. As detachments occur at different streamwise locations in different instantaneous flow fields, moving windows are assigned to each of the flow fields in the way that the origin of their coordinate system coincides with the detachment points for all of the flow fields. Therefore, the location of detachments of the conditionally averaged flow fields remains at the origin of the coordinate system. By averaging over the moving windows, the averaged properties of the flow close to the detachment events can be captured. Therefore, the result of this conditional averaging can provide features of potential structures existing close to single-detachment events. Only flow detachments occur at the wall within $-0.1 < X < 0.1$ are selected for conditional averaging (totally 503 velocity fields), because the characteristics of flow detachments can vary along streamline locations, and it is preferred to average the instantaneous flow fields carrying similar characteristics in order to magnify and reveal these characteristics.

To apply a similar procedure for Tomo-PIV flow fields, the detachment points are monitored at Z=0 along streamwise direction. The velocity vectors close to the wall in the volume of 0.12H ($X_0 - 0.06 < X < X_0 + 0.06$) × 0.03$H$ ($-0.015 < Z < 0.015$) × 0.003H ($0.001 < Y < 0.004$) are averaged to determined detachment points based on Equation (4.1) and (4.2) by extending the averaging of U along spanwise direction with the same threshold of velocity (0.009U_c). Similar to planar vector fields, the moving windows only move in streamwise direction to match the detected detachment points of different vector fields at X=0 close to the wall. Totally, 121 velocity fields are used for this conditional averaging. As the criteria and procedure used for planar and Tomo-PIV vector fields are similar, it is expected to capture similar flow structures in the results.

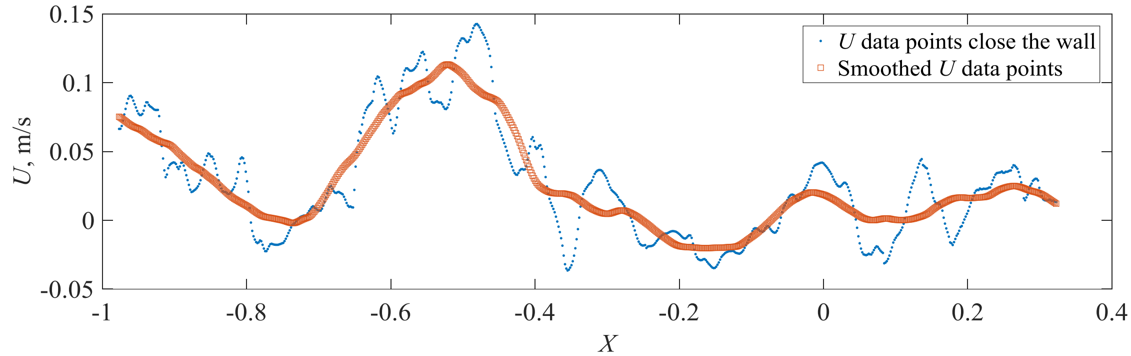

(a)

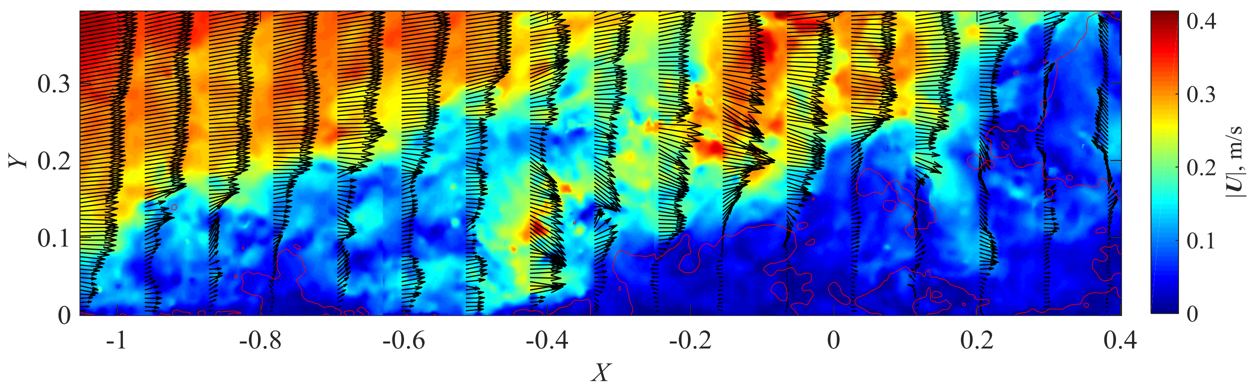

(b)

Figure 4.13 Streamwise velocity variation for one instantaneous velocity field as shown by (a) the original data points and the smoothed ones calculated by averaging over nearby data points at Y=1.8×10^{-3} (0.295 mm) along streamwise direction; and (b) the contours of zero velocity of the vector field plotted to be compared to the extracted velocity profiles. The vector field is spatially down-sampled for better visualization.

It is also possible to implement other criteria for detecting structures using Tomo-PIV flow fields, for instance, movements of separation line in Z direction and the structures involved can be investigated. Detachments close to the wall occur and move in X and Z directions; therefore tracking these structures can provide insights on mechanisms involved in initiation of detachment and the structures involved.

4.2.2 Categorizing vector fields based on detachment status

The shear layer shape and detachment state of the flow vary from one vector field to another. To quantify these variations using Equation (4.1) and (4.2) criteria, several bins/categories are defined and named as follow. There are a few vector fields in the ensemble with no significant detachment in the entire FOV. These vector fields are stored in bin 0. Vector fields with an attached flow at the upstream region of the FOV and with only one downstream detachment are stored in bin 1. Bin 2 represents vector fields with attached flow at upstream, one detachment, and a followed reattachment in the downstream region. Bin 3 represents the sequence of detachment, reattachment, and detachment from upstream to downstream. The same pattern has been repeated for next bins. For instance, bin 6 indicates occurrence of 3 pairs of detachment and reattachment starting with a detachment. The vector fields with backward flow (detached) at the very upstream boarder of the FOV are stored in bins named with negative integers. For instance, bin −1 shows that vector fields have backward flow upstream of the FOV, and the flow reattaches downstream. Bin −3 represents the sequence of reattachment, detachment and reattachment, from upstream to downstream. Same pattern and pairs of reattachment and detachment repeat similarly for next negative numbers. Finally, bin −8 represents the case of the complete detached flow. Figure 4.14 show the population of each bin for planar and Tomo-PIV vector fields. Bin −8 is very uncommon for planar PIV flow fields because of the low probability of flow detachment and backflow occurring upstream of planar FOV as γ is greater than 90% at the wall as shown in Figure 4.14 (a). However, as tomographic FOV is much smaller and is close to the average location of flow detachment, the probability of the occurrence of flow detachment upstream of the FOV is high; therefore, many of tomographic flow fields are categorized in bin −8.

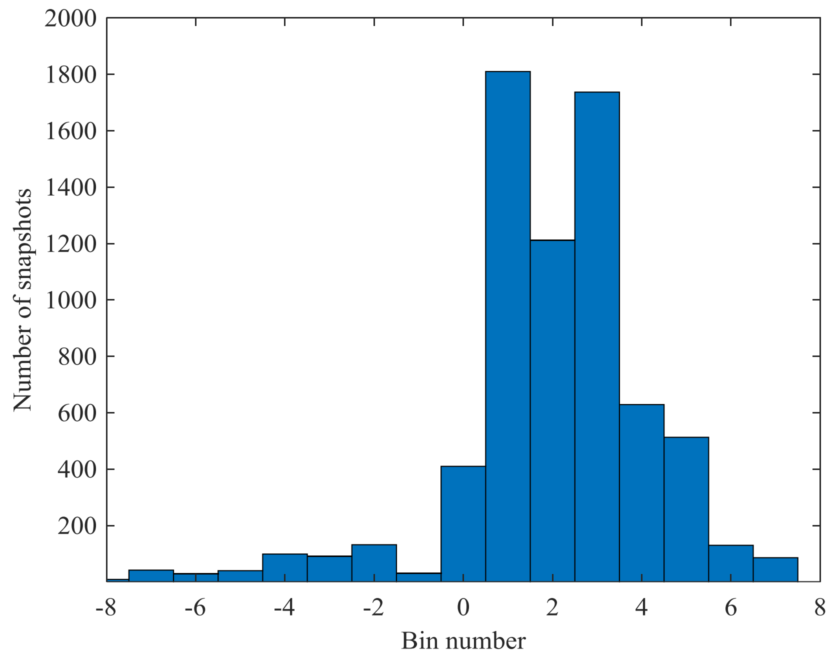

(a)

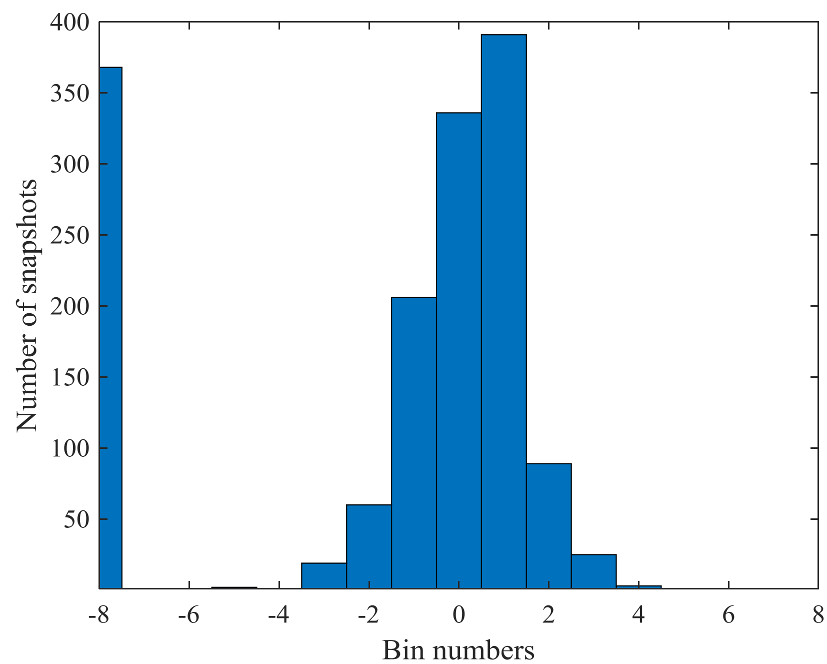

(b)

Figure 4.14 Distribution of vector fields in the defined bins for (a) planar data and (b) Tomo-PIV data. Bin 1 (single detachment) contains the maximum number of vector fields for both sets of data.

4.3 The Proper Orthogonal Decomposition

The method of 'Snapshot POD' as introduced by Sirovich (1987) is performed here, in which instantaneous flow velocity fields are used, and fluctuation components (u, v and w) of all vector fields are calculated and stored in a global matrix (U_g). Assuming each component in each vector field has M data points, and there are N vector fields, matrix $\boldsymbol{U_g}$ can be created as

$$U_g = [\boldsymbol{u}^1 \dots \boldsymbol{u}^N] = \begin{bmatrix} u_1^1 & \cdots & u_1^N \\ \vdots & \ddots & \vdots \\ u_M^1 & \cdots & u_M^N \\ v_M^1 & \cdots & v_M^N \\ \vdots & \ddots & \vdots \\ v_M^1 & \cdots & v_M^N \\ w_M^1 & \cdots & w_M^N \\ \vdots & \ddots & \vdots \\ w_M^1 & \cdots & w_M^N \end{bmatrix} \tag{4.3}$$

where $u^N{}_M$ means the M^{th} data point of N^{th} vector field for u component, similarly $v^N{}_M$ indicates v component data points. By defining the autocovarience matrix as C= $\boldsymbol{U_g}^{\boldsymbol{T}}\boldsymbol{U_g}$ and finding the eigenvectors sorted by the magnitude of the eigenvalues of this matrix, a basis is formed by constructing the POD modes as follow:

$$\phi^i = \frac{\sum_{n=1}^{N} A_n^i \,\boldsymbol{u}^n}{\left\|\sum_{n=1}^{N} A_n^i \,\boldsymbol{u}^n\right\|} \quad , \quad i = 1\dots, N \tag{4.4}$$

Here, i represents the mode associated with the i^{th} eigenvalue sorted by its magnitude. The calculated modes (ϕ^i) in Equation (4.4) are matrices containing u, v, and w components, which together, they form vector fields. These modes can also be used to reconstruct each vector field as follow

$$\boldsymbol{u}^n = \sum_{i=1}^{N} a_i^n \,\phi^i \tag{4.5}$$

Where a^n is calculated as $\psi^T\boldsymbol{u}^n$ and ψ=[ϕ^1 ϕ^2 .. ϕ^N]. This reconstruction based on limited number of modes can be used to remove noise and small-scale features from each vector field. The mathematical details are explained in Holmes et al. (1998). Lumley (1967) showed that the total kinetic energy of each velocity fluctuation field is associated with the magnitude of the corresponding eigenvalue. Therefore, the first modes are the dominant features of the flow with maximum kinetic energy. For planar vector fields, only u and v components appear in $\boldsymbol{U_g}$, and other equations.

4.3 Conclusion

Different analyses are performed in this study are explained in this chapter. First, the procedure of the stitching of planar flow fields and its associated uncertainties are described. Second, the conditional averaging performed in this study in addition to the procedure of categorizing different flow fields are mathematically explained. Finally, the mathematical principles of the POD analysis are explained.

Chapter 5 Planar field

The properties of the flow field captured by planar PIV measurement are presented here. The large measurement region provides instantaneous flow velocity very upstream and downstream of the flow detachment. By applying conditional averaging method, quadrant analysis and POD analysis, it is tried to find and characterize the flow structures involved at the detachment instants and most energetic flow motions.

5.1 Mean flow field

Mean properties of the flow are presented here using the planar velocity vector fields. Mean velocity components, Reynolds stresses, γ contours, and third-order moments are presented and compared with previous studies to evaluate the flow regime and general features of the flow field. In addition, the spatial distribution of Reynolds stresses and third-order moments are discussed.

5.1.1 Mean velocity field

Figure 5.1 shows the vector field of flow velocity. The origin of the coordinate system is located at the detachment point on the wall where $\partial \langle U \rangle / \partial y = 0$. The mean flow decelerates upstream of the detachment point until it detaches from the wall at $X = 0$, and a recirculation zone forms and extends downstream of the FOV. The white contour shows the region where $|\boldsymbol{U}|$ is approximately zero ($|\boldsymbol{U}| < 5\times10^{-3}$ m/s) and separates forward flow from backward flow.

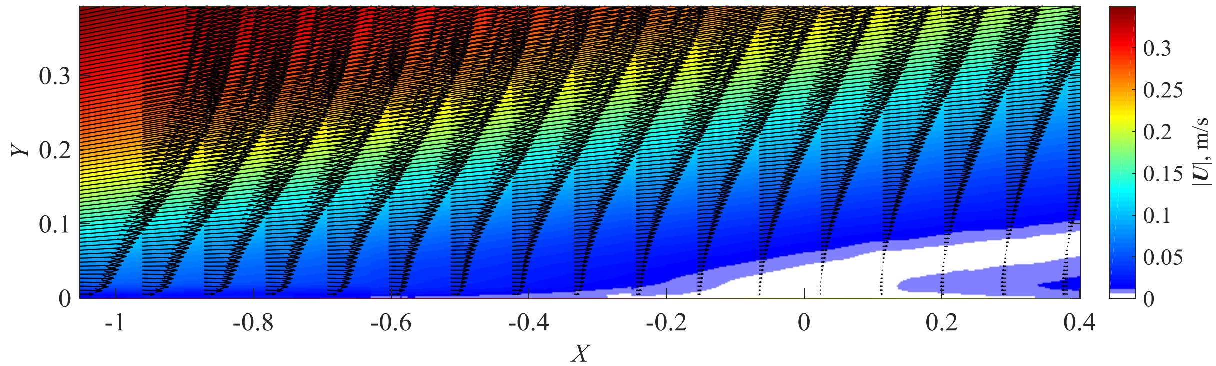

Figure 5.1 Mean velocity vector field with background colormap of velocity magnitude |***U***| (m/s). The vector field has been spatially decimating by the factor of 3 along *Y* direction and 50 along *X* direction for better visualization in this figure.

The mean streamwise velocity (<*U*>) distribution is shown in Figure 5.2, which has the maximum value of 0.35 m/s at the upstream of the FOV and far away from the wall. The white contour shows the region with almost zero streamwise velocity. The backward flow with maximum magnitude of 0.012 m/s appears downstream of the white contour.

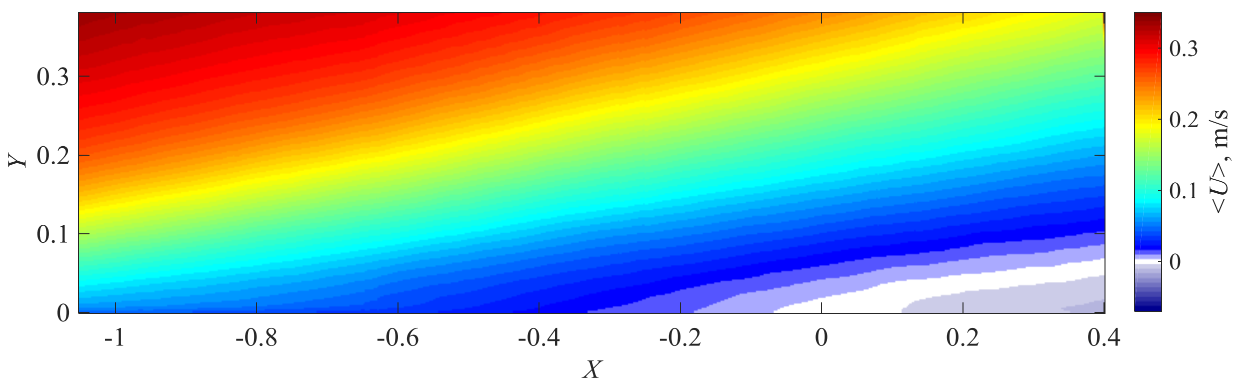

Figure 5.2 Streamwise mean velocity, <*U*> (m/s). The streamwise velocity decreases along streamwise direction, and a recirculation region appears downstream of the FOV.

The magnitude of wall-normal velocity is shown in Figure 5.3. Similar to streamwise velocity, the mean wall-normal velocity decreases in streamwise direction. As the inclined plate has an angle with water channel walls and free-stream flow, the direction of the flow close to the inclined plate (the wall here) redirects and becomes parallel to the wall. In addition, due to increase in TBL thickness close to flow separation, the region close to the wall where the flow direction is affected by the orientation of the wall becomes larger. Therefore, the flow direction becomes parallel to the wall at locations away from the wall downstream of the FOV.

The streamlines are shown in Figure 5.4 with background contours of <*U*> normalized by U_c (= 0.451 m/s), which is the free-stream velocity at $X = -10$ and $Y = 0$. The streamlines close to the wall (Y<0.1) moves away from the wall as the recirculation zone appears at the detachment point and blocks the flow. The streamlines located close enough to the wall (Y<0.05) starts curving and rotating in the recirculation region, and streamlines further from the wall (0.05 <X<0.1) only move away from the wall and continue moving forward downstream of the FOV as shown in Figure 5.4. Streamlines located at Y>0.1H tend to follow free-stream velocity upstream of the field, and as they become close to the recirculation zone, they are deflected toward the wall and become more parallel to the wall direction (Figure 5.4).

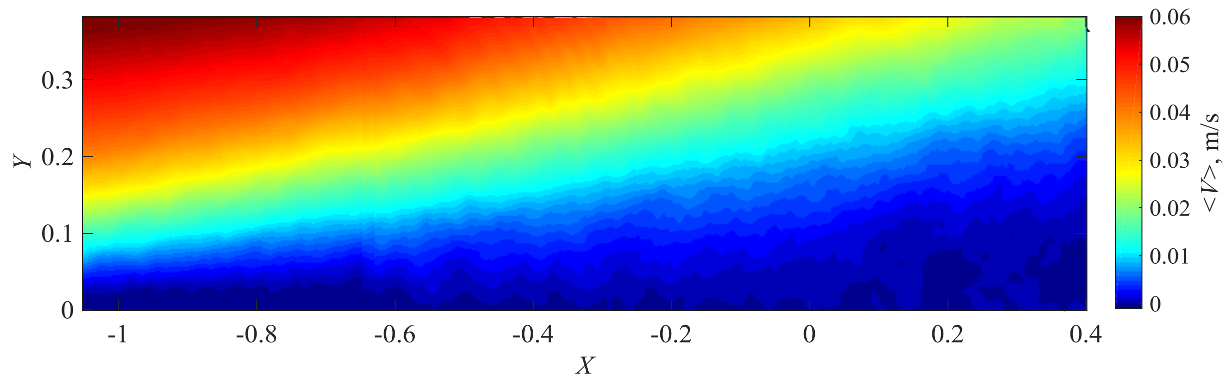

Figure 5.3 Wall-normal mean velocity, <*V*> (m/s). Downstream of the FOV, the *V* component is smaller in magnitude compared with the upstream, and in the separation region its magnitude is almost zero compared to <*U*> component.

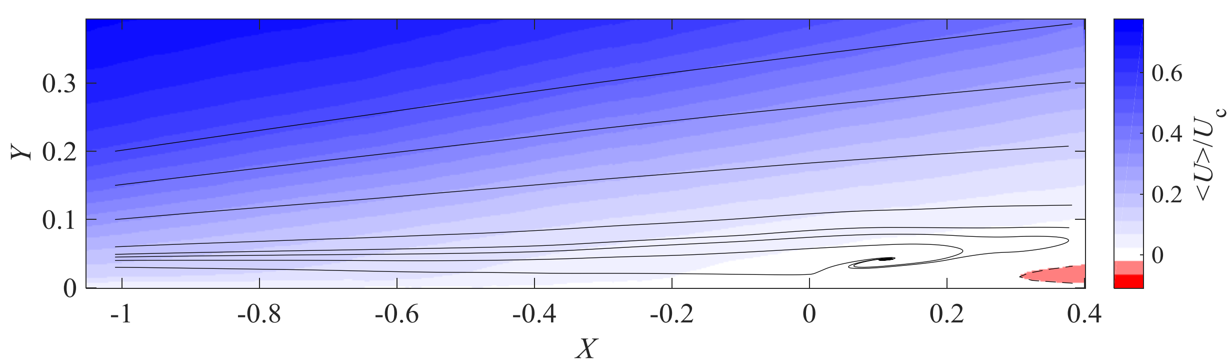

Figure 5.4 The configuration of streamlines in the freestream and close to the recalculation zone. The streamlines are deflected close to the detachment point. The background color shows <*U*> normalized by U_c.

To present the fraction of time that the flow moves in positive *X* direction, the distribution of γ (%), as defined and explained in section 2.1, is plotted in Figure 5.5. The FOV covers γ between 35% to 92% including ITD (80%) and TD (50%) points as defined by Simpson et al. (1996). The pattern of the contours is similar to streamwise velocity pattern of Figure 5.2. The γ=50% contour does not coincide with the detachment point ($\partial\langle U\rangle/\partial y=0$) at the wall in contrast to the result reported by Simpson et al. (1996) in their study on two-dimensional flow separation. This inconsistency can be due to the three-dimensionality of the investigated flow. This is also observable from the probability distribution of streamwise velocity at the detachment point very close to the wall (X=0 and Y= 0.0036H) shown in Figure 5.6. The probability of backward flow is slightly larger than forward flow as the distribution has more area in the region with negative value of U, which is consistent with γ being less than 50% at this point as shown in Figure 5.6.

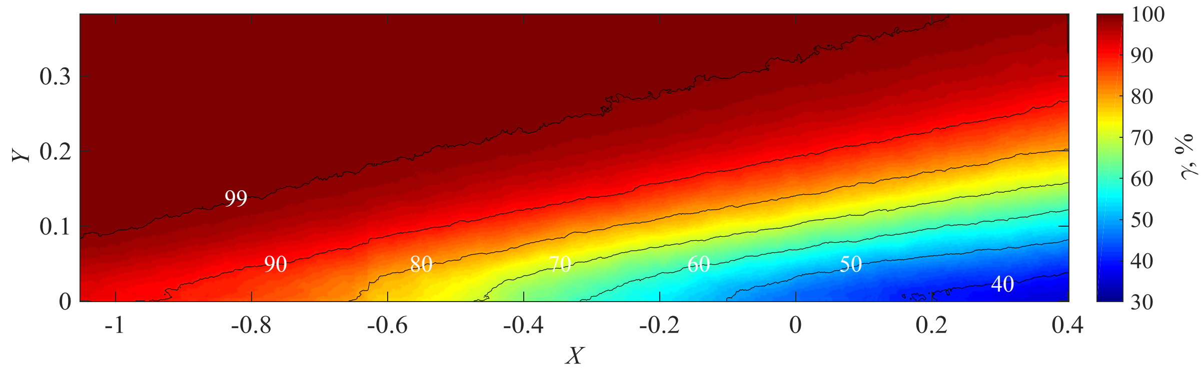

Figure 5.5 Distribution of γ (%). γ is between 35% to 92% at the wall in this FOV, which includes ITD (80%) and TD (50 %) points.

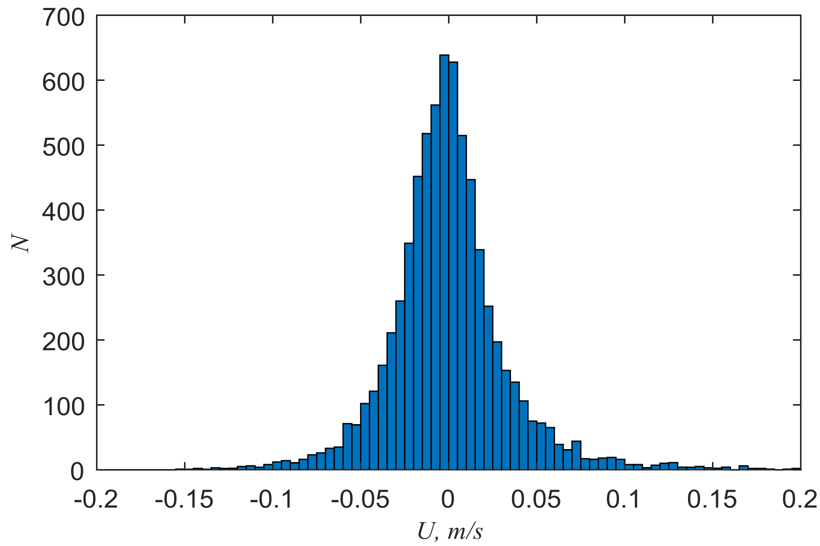

Figure 5.6 Probability distribution of U at X=0 and Y= 0.0036H.

5.1.2 Reynolds stresses

Streamwise normal stress, $<u^2>$, wall-normal stress, $<v^2>$ and Reynolds shear stress, $-<uv>$, distributions normalized by U_c are shown in Figure 5.7 (a), (b) and (c) respectively. The magnitude of $-<uv>$ increases in streamwise direction. Distribution of $<u^2>$ has a maximum located at around Y= 0.1H for X=−H and the location of the maximum reaches Y= 0.3H at X=0.4H. Distribution of $<v^2>$ has a maximum at Y= 0.1H for X=-H and it reaches Y= 0.25H at X=0.4H. As explained by Cuvier et al (2014), the region above the recirculation zone has large-scale structures with both high u and v fluctuations. This can explain the similarity between the patterns of $<u^2>$ and $<v^2>$. Similarly, the distribution of $-<uv>$ has a peak at each streamwise location (X) that moves away from the wall. The loci of the peak of $-<uv>$ for each streamwise location is approximated by a dashed line as shown in Figure 5.7 (c). Cuvier et al (2014) reported almost similar pattern of high magnitude of $|<uv>|$ above a separation bubble formed on a flap as the loci of the peak follow a curve that encompasses the separation bubble. Simpson (1989) also reported same pattern of the movement of the peak of Reynolds shear stress in a pressure induced separated flow, in which the loci of the peak suddenly moves away from the wall at the detachment point and appears above the separation bubble. This region is explained to be due to the passage of large-scale eddies of the separated shear-layer (Cuvier et al. 2014).

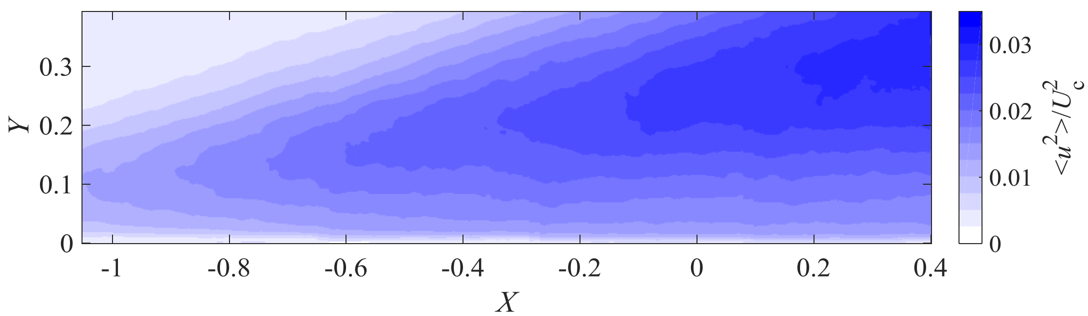

(a)

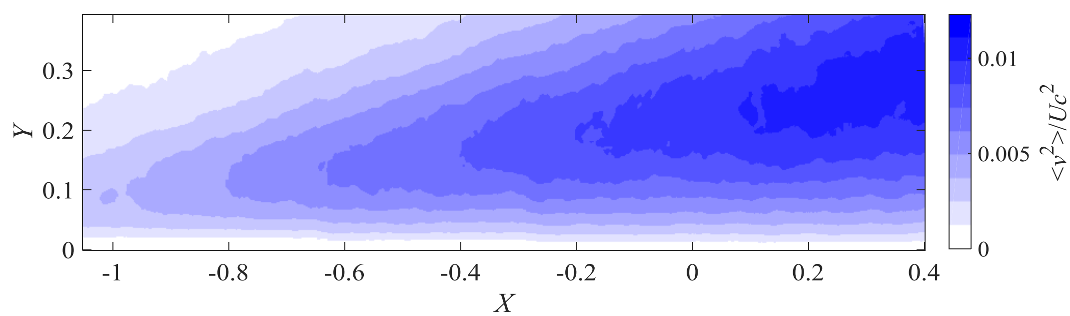

(b)

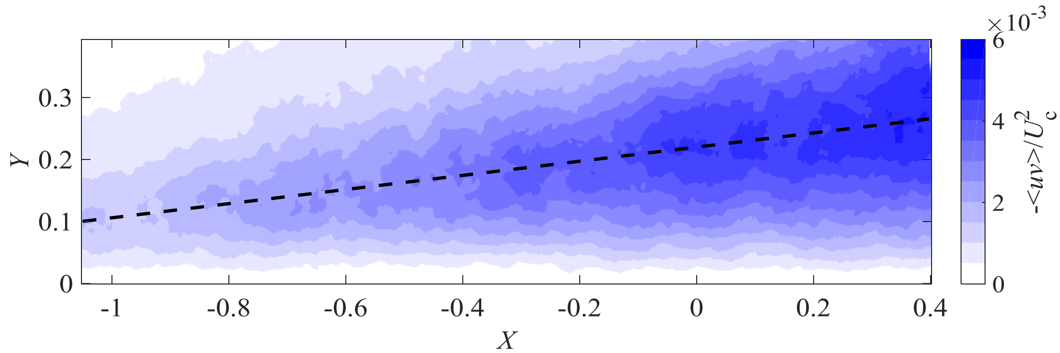

(c)

Figure 5.7 Distribution of Reynolds stresses (a) $<u^2>/Uc^2$, (b) $<v^2>/Uc^2$ and (c) $-<uv>/Uc^2$. The similar patterns of the stresses represent a high turbulence region above the recirculation zone. The dashed line shows the loci of the peak of $-<uv>$ at each streamwise location.

5.1.3 Third-order moments

Third-order moments provide statistical information of *u* and *v* fluctuations including the skewness of their probability. As depicted in Figure 5.8 (a), $<u^3>$ has positive values close to the wall and has higher magnitude downstream of the FOV at the recirculation region compared with upstream of the FOV. The region with positive values of $<u^3>$ expands in the downstream and covers a large region above the wall. A region with negative values of $<u^3>$ appears above the region with positive values, and similarly it increases in height downstream of the FOV. Similarly, the distribution of $<v^3>$ as shown in Figure 5.8 (b) shows a region with negative strong *v* fluctuations, which originates at $Y= 0.05H$ and $X=-0.8H$ and expands in wall-normal direction downstream of the FOV until it reaches $Y= 0.3H$. The shape and location of this region are similar to the ones of the region with positive $<u^3>$ in Figure 5.8 (a), which shows a region where strong sweep motions occur ($u > 0$, $v <0$).

In addition, distributions of $<u^3>$ and $<v^3>$ as shown in Figure 5.8 (a) and (b) downstream of the FOV and away from the wall suggest that this region contains strong negative *u* fluctuations and slightly positive *v* fluctuations representing ejection motions ($u < 0$, $v > 0$). Distribution of $<u^2v>$ also suggests that negative *v* fluctuations are stronger close to the wall downstream of the FOV and positive *v* fluctuations appear away from the wall as shown in Figure 5.8 (c). Distribution of $<uv^2>$ shows strong *u* fluctuations close to the wall downstream of the FOV and negative ones away from the wall as shown in Figure 5.8 (d), which confirms the previous conclusions.

The region with negative value of *v* component close to the recirculation region at the wall accompanies strong $<u^2>$, and similarly, the region with positive value of *v* away from the wall and above the shear layer contains strong $<u^2>$ as shown in Figure 5.8 (a) and Figure 5.8 (c). This distribution shows the production of $<u^2>$ at the shear layer is convected away from this region along wall-normal direction. Similarly, positive values of $<u^3>$ downstream of the shear layer and negative values of $<u^3>$ upstream of the shear layer represent the diffusion of the production of $<u^2>$ at the shear layer away from it towards downstream and upstream with positive and negative *u*, respectively as shown in Figure 5.8 (a). This pattern and description of the transport terms are also provided by Skåre and Krogstad (1994).

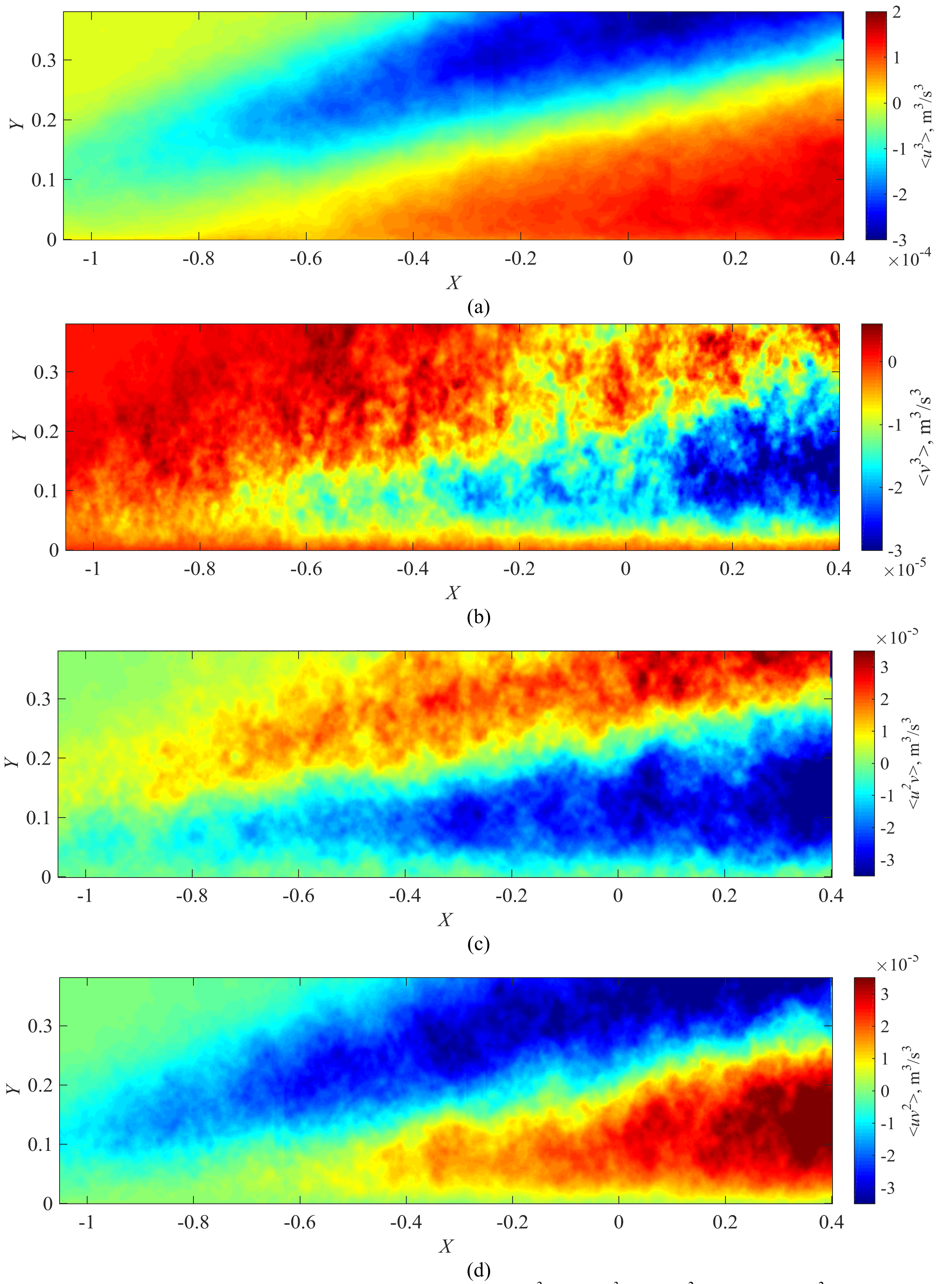

Figure 5.8 Distribution of third order moments including (a) $<u^3>$ (b) $<v^3>$ (c) $<u^2v>$ and (d) $<uv^2>$. Strong u and v fluctuations and their sign appear in these distributions.

5.1.4 Turbulence production

The production terms $-\langle uv\rangle\ \partial\langle U\rangle/\partial Y$ and $-\langle u^2\rangle\ \partial\langle U\rangle/\partial X$ are plotted in Figure 5.9 (a) and (d). Similar to Reynolds stresses patterns, the maximum value of production occur away from the wall, and the loci of the maximum values at different streamwise location moves away from the wall. The magnitude of production also has a general increase in the streamwise direction while the region with high turbulence production expands downstream of the FOV. The patterns of these normalized terms are almost same, and their magnitudes are close to the normalized ones reported by Cuvier et al. (2014). The magnitude of the two terms is almost the same in the entire FOV, and they correspond to the available production terms of $\langle u^2\rangle$. Similar patterns are repeated for $-\langle uv\rangle\ \partial V/\partial X$ and $-\langle v^2\rangle\ \partial V/\partial Y$ as shown in Figure 5.9 (b) and Figure 5.9 (c). The term $-\langle u^2\rangle\ \partial U/\partial X$ appears stronger compared with other production terms. The distribution of $-\langle uv\rangle\ \partial V/\partial X$ contains noise-like variations, although, the similar pattern of a high-magnitude region can be recognized also in Figure 5.9 (b). Wave-like variations in the magnitude of almost all turbulent production terms can be observed in Figure 5.9. These noise-like patterns are not repeated in the turbulent production terms as reported by Cuvier et al. (2014). Therefore, these variations can be due to PIV measurement errors as they appear in the spatial derivatives of U and V.

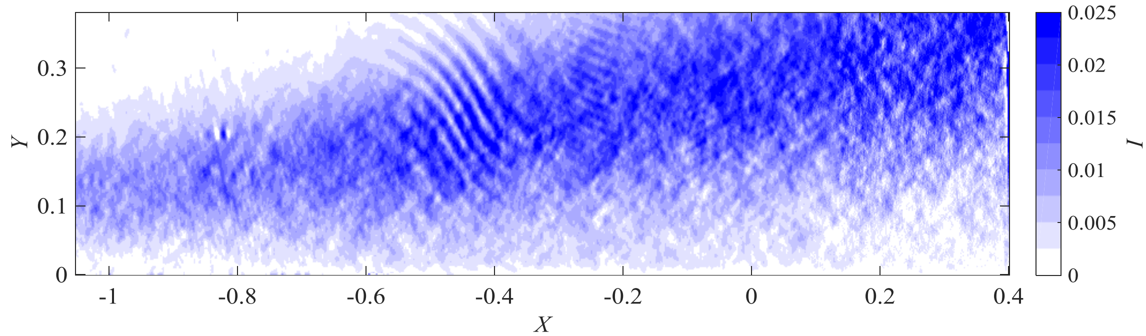

(a)

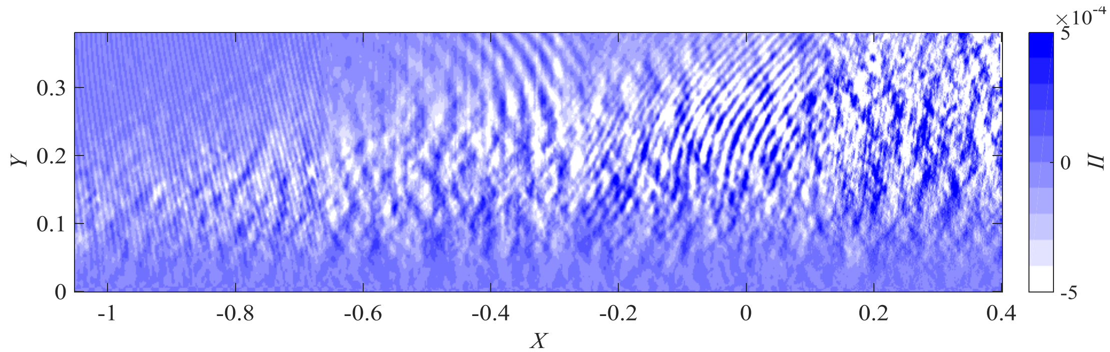

(b)

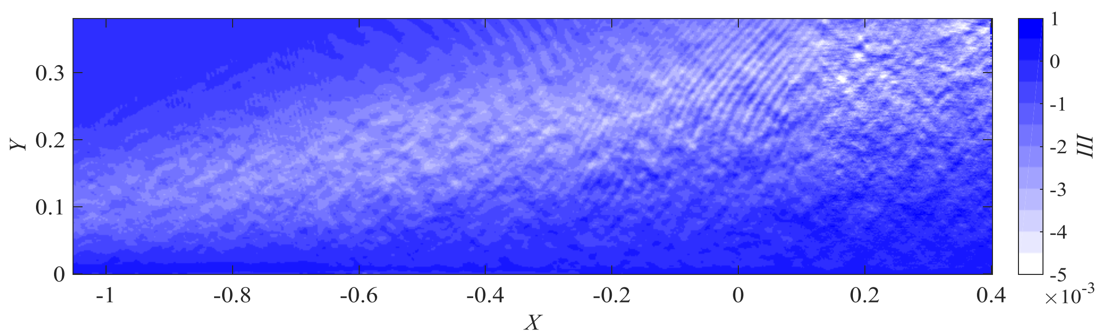

(c)

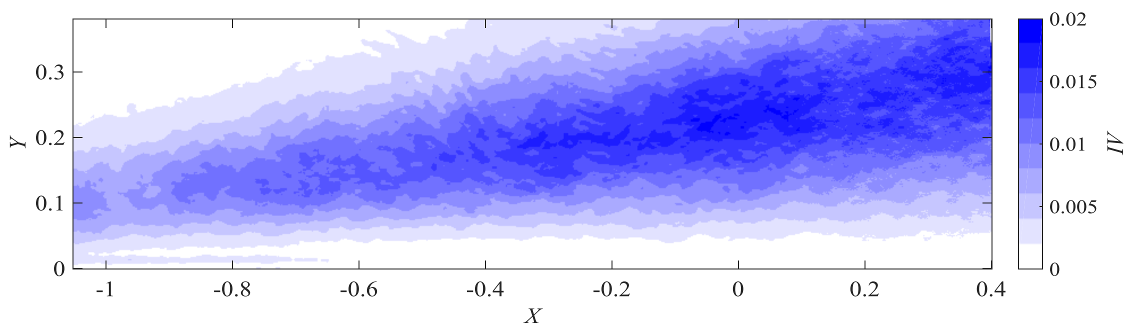

(d)

Figure 5.9 Turbulence production terms are plotted normalized with U^3_c including (a) $I = -\langle u^2\rangle\, \partial\langle U\rangle/\partial X \,/\, U^3_c$ (b) $II = -\langle uv\rangle\, \partial\langle V\rangle/\partial X \,/\, U^3_c$ (c) $III = -\langle v^2\rangle\, \partial\langle V\rangle/\partial Y \,/\, U^3_c$ and (d) $IV = -\langle uv\rangle\, \partial\langle V\rangle/\partial Y \,/\, U^3_{c}$.

5.2 Coherent structures at the separation instants

Planar flow fields are categorized based on the criteria and detachment status explained in chapter 4.3. Vector fields with different detachment configuration may contain specific structures. For instance, vector fields with one strong detachment may contain flow structures that initiate strong detachments, and vector fields with detachments and reattachments may contain flow features causing local detachments.

5.2.1 Instantaneous flow fields with strong single-detachments

In this section, the mean flow properties of the vector fields with single detachment (i.e., bin 1) are characterized using conditional averaging technique. The flow fields with strong detachments within $X = -0.1$ to $+0.1$, for which a large back flow region is guaranteed until the end of the FOV, are separated for conditional averaging. In order to investigate the flow properties and events at the occurrence of flow separation, the detachment points in each flow field were located. Afterward, according to the location of the detachment, a moving window captures velocity fields at ΔX=0.95H upstream and ΔX=0.3H downstream of the detachment points. As detachments occur at different streamwise locations of the instantaneous flow fields, moving windows are assigned to each of the vector fields, so the origin of their coordinate system coincides with the detachment point for all the vector fields. Therefore, the location of detachments of the conditionally averaged vector fields remains at the origin of the coordinate (i.e., X=0). By averaging over the moving windows, the averaged properties of the flow close to the detachment events can be investigated. Therefore, the result of this conditional averaging can provide features of structures in single-detachment events.

Mean velocity field

The conditionally averaged velocity field, $\boldsymbol{U_c}$, shows a strong detachment at the origin, which is followed by strong backflow as shown in Figure 5.10 compared to mean velocity field for all vector fields as shown in Figure 5.1. Comparing Figure 5.10 with Figure 5.1, the formed recirculation zone of $\boldsymbol{U_c}$ is spatially larger and contains a stronger backflow downstream of the detachment point. The distribution of streamwise velocity magnitude $<U_c>$ is shown in Figure 5.10 (b) and indicates a large negative streamwise velocity gradient close to the separation line. The distribution of wall-normal velocity is shown in Figure 5.10 (c). In comparison with wall-normal mean velocity field of Figure 5.3, a region with high magnitude of $<V_c>$ appears above the detachment point, representing a strong upward motion as the flow separates and moves away from the wall above the detachment point as shown in Figure 5.10 (c).

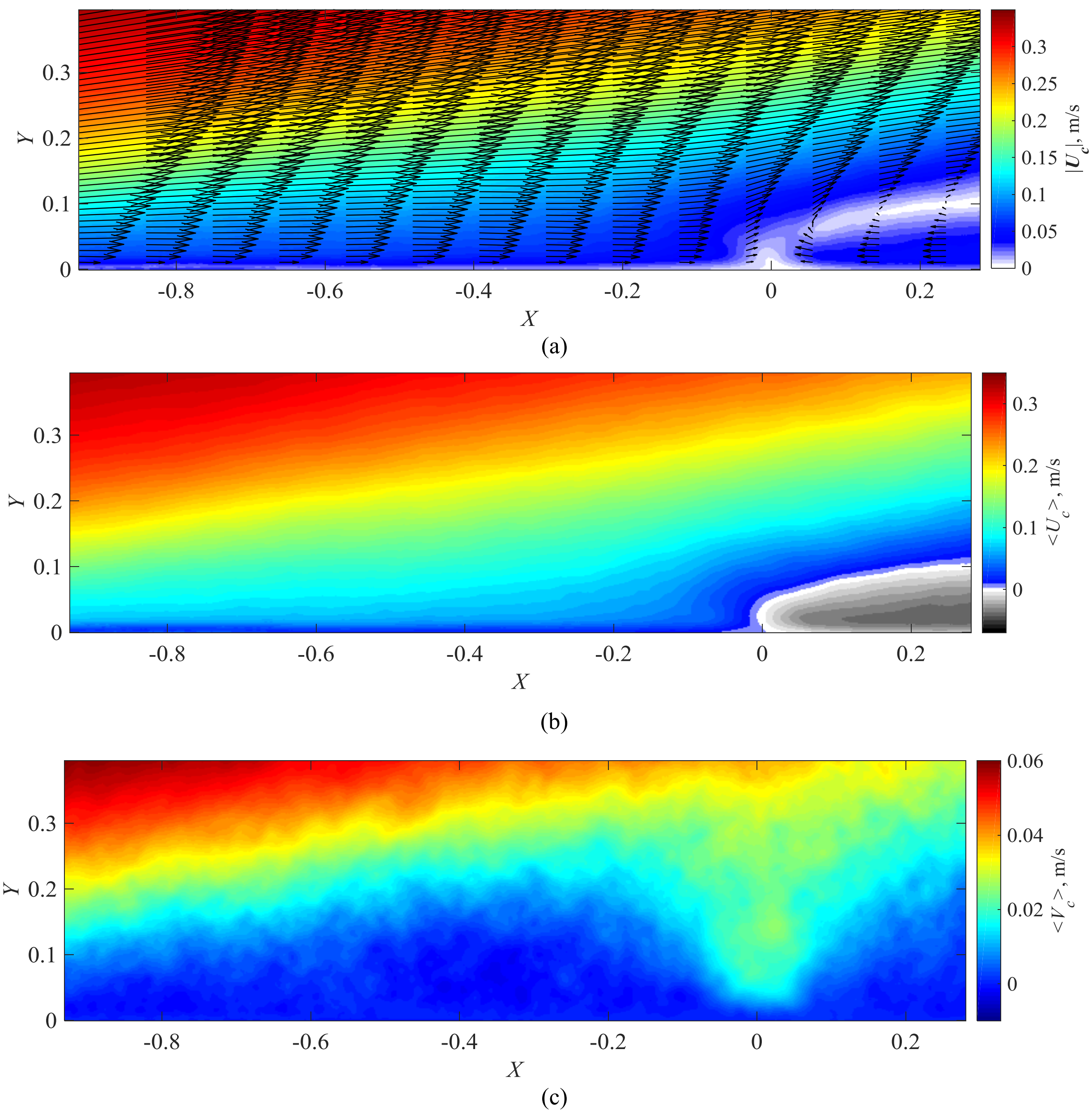

Figure 5.10 Conditional averaging over strong single-detachment vector fields. (a) Vector field with background colormap of the magnitude of velocity, $|\boldsymbol{U}_c|$ (m/s), (b) streamwise velocity, $<U_c>$, and (c) wall-normal velocity, $<V_c>$.

Reynolds stresses

The conditional averages of Reynolds stresses are shown in Figure 5.11. Reynolds shear stress, $-\langle uv_c \rangle$, shows almost the same pattern as the one calculated without conditional averaging. However, close to the detachment point (i.e., the origin), a distinguishable region with low magnitude of $\langle uv_c \rangle$ appears at $-0.2<X<0$ and $Y<0.2$ as shown in Figure 5.11 (a). As shown in Figure 5.11 (b), $\langle u_c^2 \rangle$ has small magnitude close to the detachment point, suggesting relatively smaller magnitude of u fluctuations. Distribution of $\langle v_c^2 \rangle$ is shown in Figure 5.11 (c), which suggests that unlike $\langle u_c^2 \rangle$ distribution, a region with relatively strong $\langle v_c^2 \rangle$ appears close to the detachment location within $-0.15<X$ and $0.1<Y<0.3$. This region with strong $\langle v_c^2 \rangle$ extends to downstream of the FOV. High positive v fluctuations here can be due to strong blockage and backflow existing in single-detachment flow fields at their detachment points. This blockage causes the upstream forward flow to move upward and away from the wall to make space for backward flow downstream, which results in strong v motions above the detachment point. This upward motion also can be seen in streamlines of the average field as shown in Figure 5.4.

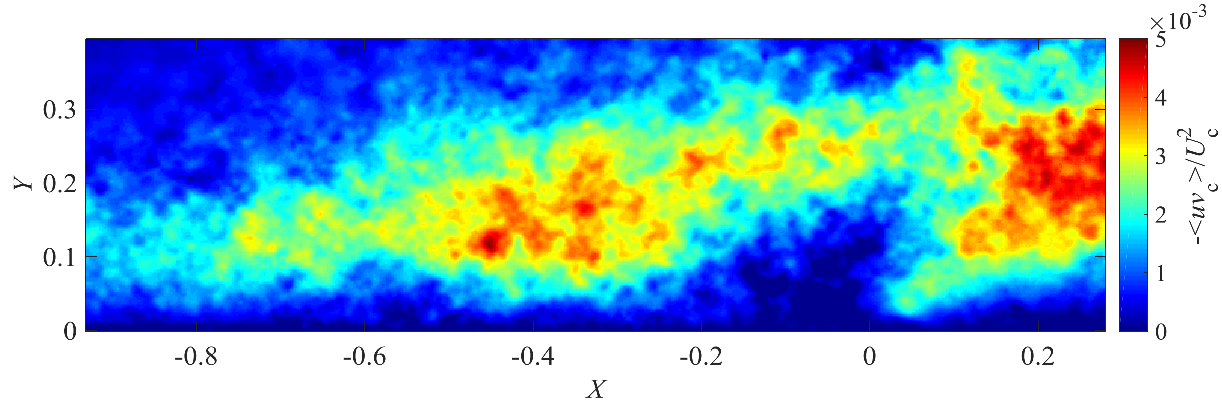

(a)

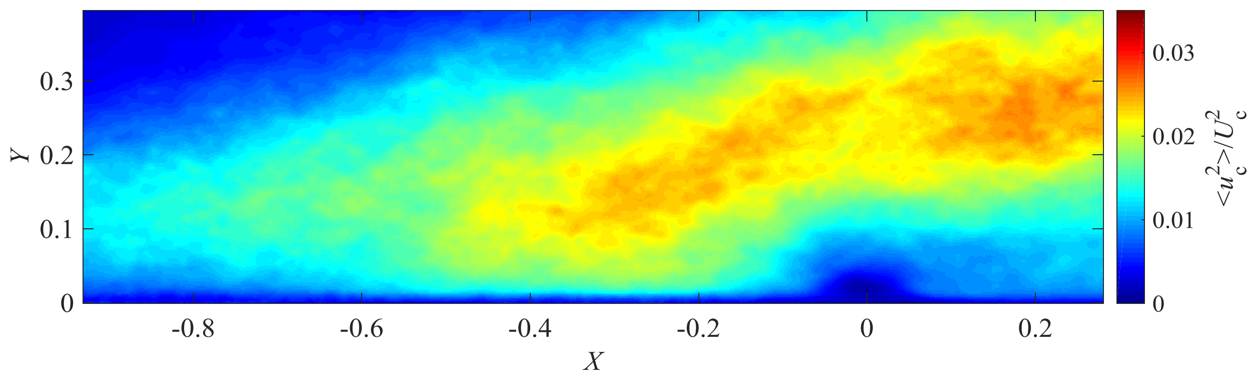

(b)

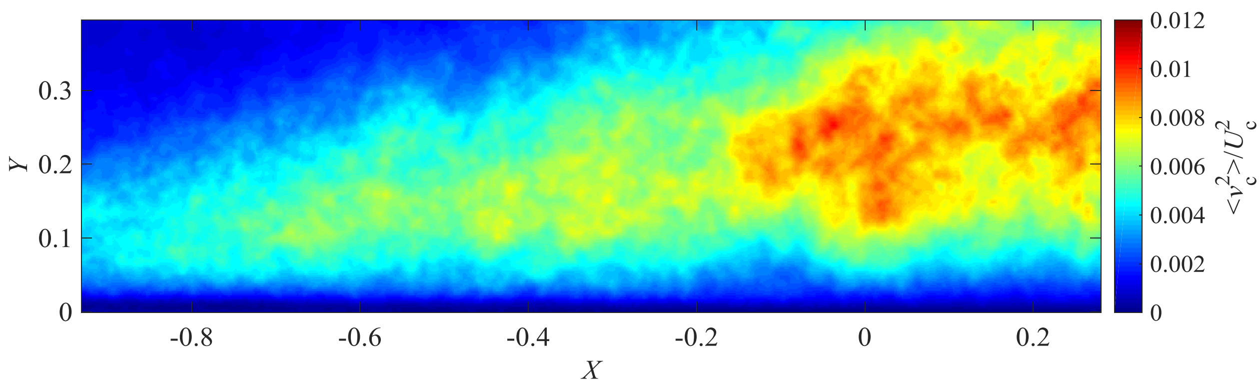

(c)

Figure 5.11 Conditional average of Reynolds stresses including (a) $-\langle uv_c \rangle$, (b) $\langle u_c^2 \rangle$ and (c) $\langle v_c^2 \rangle$. The distributions show different patterns compared with original Reynolds stresses.

Third-order moments

The distributions of third-order moments based on the conditionally selected vector fields are shown in Figure 5.12. In comparison with Figure 5.8, the distributions have completely changed. The distribution of $<u_c^3>$ and $< uv_c^2>$ illustrate a region upstream of the detachment point where strong positive u fluctuations occur as shown in Figure 5.12 (a) and (b) respectively. The center of this region is approximately located at $X=-0.3H$ and $Y=0.1H$. Distributions of $< u^2v_c>$ and $<v_c^3>$ also show that there are strong negative v fluctuations occurring at the same region. Therefore, it can be concluded that sweep events are a dominant feature of the flow upstream of the single detachments. However, u fluctuations are considerably stronger compared with v fluctuations for these motions. A region with strong positive v fluctuation appear around X=0 and $Y=0.15H$, which also appears in Reynolds stresses as explained in the previous section. This region is not associated with strong u fluctuations, and it represents blockage of the backward motion as explained before.

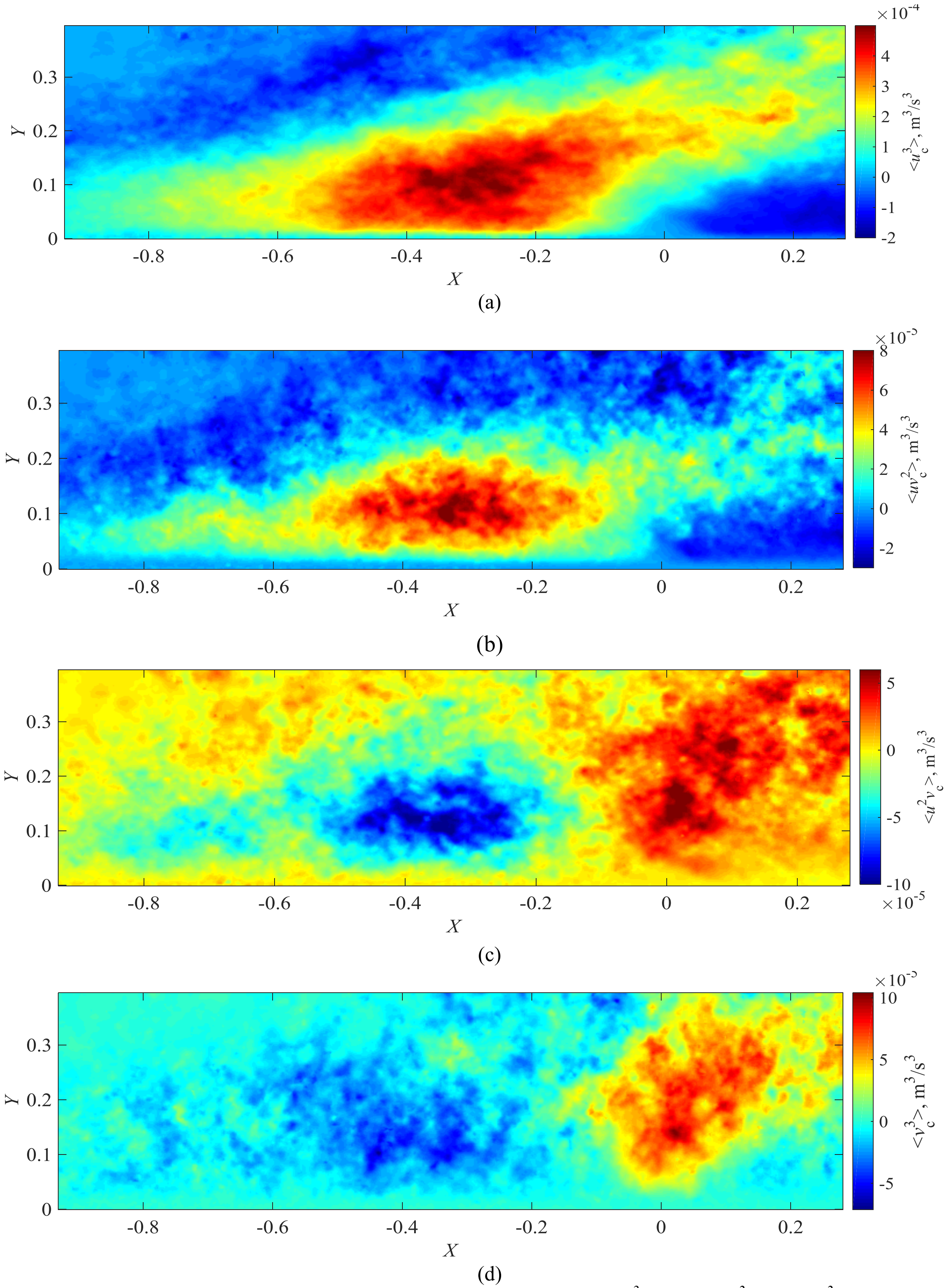

Figure 5.12 Conditional average of third-order moments including (a) $<u_c^3>$ (b) $< uv_c^2>$ (c) $< u^2v_c>$ and (d) $<v_c^3>$. Different patterns of the third moment suggest regions with strong u fluctuations.

5.3 Quadrant analysis

The quadrant analysis reveals the organizations of fluctuation components and Reynolds stresses as they have previously introduced in Chapter 1. Quadrant analysis is performed for 8 locations along streamwise direction from X=−0.848H to X=0.242H with 25 mm gap at Y=0.0303H. Another 8 locations are also selected at same streamwise locations at Y=0.182H as shown in Figure 5.13. First, quadrant analysis is performed considering all vector fields and plotted for 16 points at two different wall-normal locations of Y=0.0303H and Y=0.182H as shown in Figure 5.14 and Figure 5.15 respectively. Second, similar to the described conditional averaging in the previous section, single-detachment (bin 1) vector fields are separated and the quadrant analysis is also performed at the same 16 points as shown in Figure 5.16 and Figure 5.17. The vector fields are captured with frequency of 2 Hz, with this frequency, it is possible to track the flow structures being convected close to the wall within the FOV for several consecutive flow fields. In order to investigate the dominant events occurring for conditionally selected vector fields using quadrant analysis in time, the vector fields captured right before the single-detachment vector field are analyzed. Assuming that one of the single-detachment vector fields is captured at t_0, the vector field captured at $t_0-\Delta t$, where Δt =0.5 s, belongs to a new set of vector fields are analyzed in Figure 5.18 (for Y=0.0303H) and Figure 5.19 (for Y=0.182H). Similarly, the quadrant analysis of the vector fields captured at $t_0-2\times\Delta t$ are plotted in Appendix B.

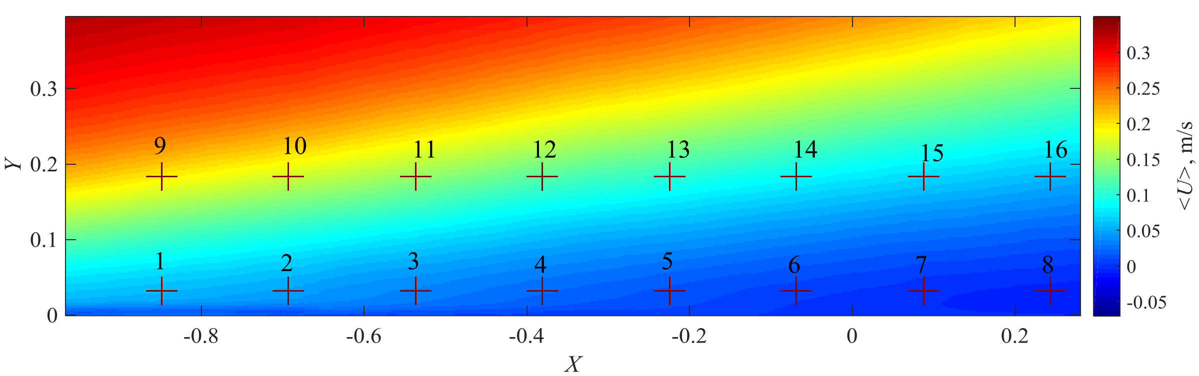

Figure 5.13 Positions of points 1 to 16 at different streamwise and normal-wise locations (Y=0.0303H and Y=0.182H).

By performing the analysis on all of the flow fields at point 1, the quadrant distribution is almost symmetric, and the four quadrants almost have similar patterns, however, u fluctuations have higher strength compared with v fluctuations. For points 2 to 8, strong positive u fluctuations appear among Q1 and Q4 events as shown in Figure 5.14. Further away from the wall (Y=0.182) and upstream of the FOV, quadrant analysis at point 9 shows strong negative u fluctuations and strong frequent Q2 events. For point 10, the negative u fluctuations have become stronger as shown in Figure 5.15. This trend has continued for point 11. For point 12, a strong u fluctuation has also appeared especially among Q4 events. The quadrant distribution of point 13 shows both negative and positive u fluctuations with high frequency and strength of Q2 and Q4 events as shown in Figure 5.15. Same patterns are repeated for points 14 and 15. For point 16, downstream of the FOV, positive u fluctuations are stronger compared to negative u fluctuations. It can be concluded for all the points away from the wall (points 9 to 16) that Q2 and Q4 events are more frequent compared to Q1 and Q3 in contrast to the points close to the wall. Quadrant analysis is separately applied to the instantaneous flow fields with single-detachment as shown in Figure 5.16 and Figure 5.17.

Close to the wall and upstream of the FOV (point 1), positive u fluctuations have higher strength and frequency. However, v fluctuations do not have a tendency toward negative or positive values as shown in Figure 5.16. This trend continues for points 2 to 6 with increase in the strength of positive u fluctuations. For point 7, which is right after the detachment point, strong negative u fluctuations have become dominant with high frequency Q2 events as shown in Figure 5.16 (g). A similar pattern with stronger negative u fluctuations has repeated for point 9 as shown in Figure 5.16 (f). Far away from the wall, at point 9, the positive u fluctuations are still frequent and Q4 events are dominant as shown in Figure 5.17 (a). Almost a similar pattern has repeated for downstream points (10 to 12), however, the strength of the events has increased and Q1 events are more dominant for points 13 and 14 as shown in Figure 5.17. For points 15 and 16, Q2 and Q4 are dominant and the events have stronger strength compared with upstream points as shown in Figure 5.17 (g) and Figure 5.17 (h). As conditionally average flow fields suggested in the previous section, the strong flow features exist close to the wall, which is also confirmed by their strong effects on the quadrant distributions.

Quadrant analysis is also performed on flow fields captured Δt ahead of the occurrence of single-detachment flow fields as shown in Figure 5.18 and Figure 5.19. Same pattern has repeated for points 1 to 8, however, the region with positive u fluctuations appears at points 3 and 4, and the region with negative u fluctuations appears at points 6, 7 and 8 as shown in Figure 5.18. This means that the same pattern of single-detachment flow fields has convected upstream. Also for points 9 to 16, almost same pattern is repeated compared to single-detachment flow fields. However, the location where the organization of u fluctuations change from frequent positive values to negative ones has moved upstream as shown in Figure 5.18. The variation in quadrant patterns from one point to another is less significant in the last quadrant distributions as it can be concluded from Figure 5.18. The instantaneous flow fields captured at $2\Delta t$ before the single-detachment flow fields are analyzed in Appendix B.

The results of the quadrant analysis are similar to the results of the conditional averaging analysis. Both indicate the existence of a region containing high-strength positive u fluctuations upstream of the detachment with frequent low-strength negative v fluctuations, and a region containing high-strength negative u fluctuations downstream of the detachment. The latter region also accompanies positive v fluctuations, which forms ejection motions, especially for single-detachment flow fields and the ones captured Δt before single-detachment flow fields. These flow structures are observed to be convected upstream of the FOV for the flow fields captured at Δt and $2\Delta t$ before single-detachment flow fields. The quadrant analysis confirms the results of conditional averaging of flow fields that a region containing strong positive u fluctuations appears upstream of detachment points. This structure appears close to the wall as it has strong signature and strength at Y=0.03 compared to Y=0.18. It also extends more than 0.6H in streamwise direction as it has appeared in several points of the quadrants upstream of the detachment point.

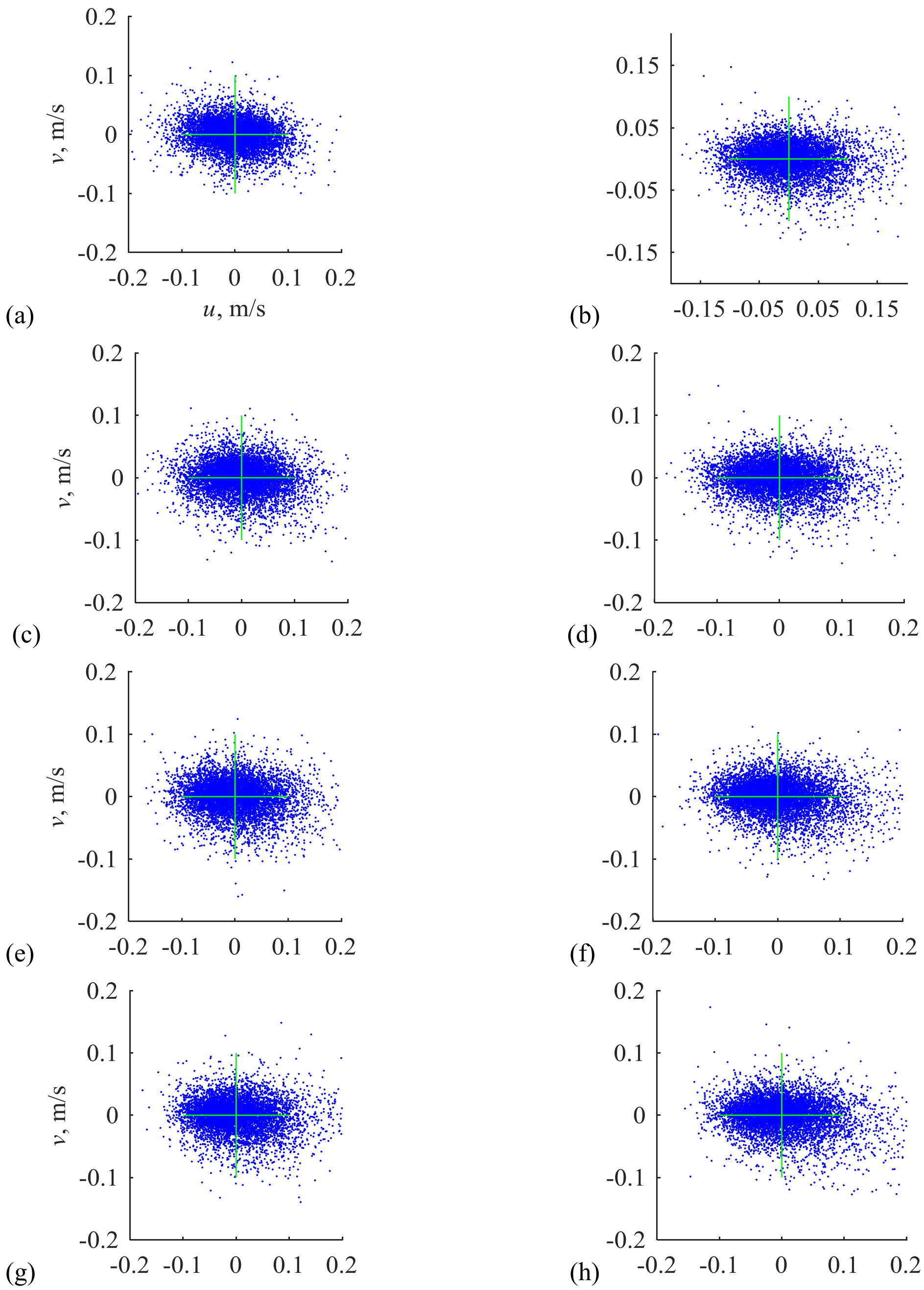

Figure 5.14 Quadrant analysis for all flow fields at points 1 (a) to 8 (h) located at Y=0.0303H.

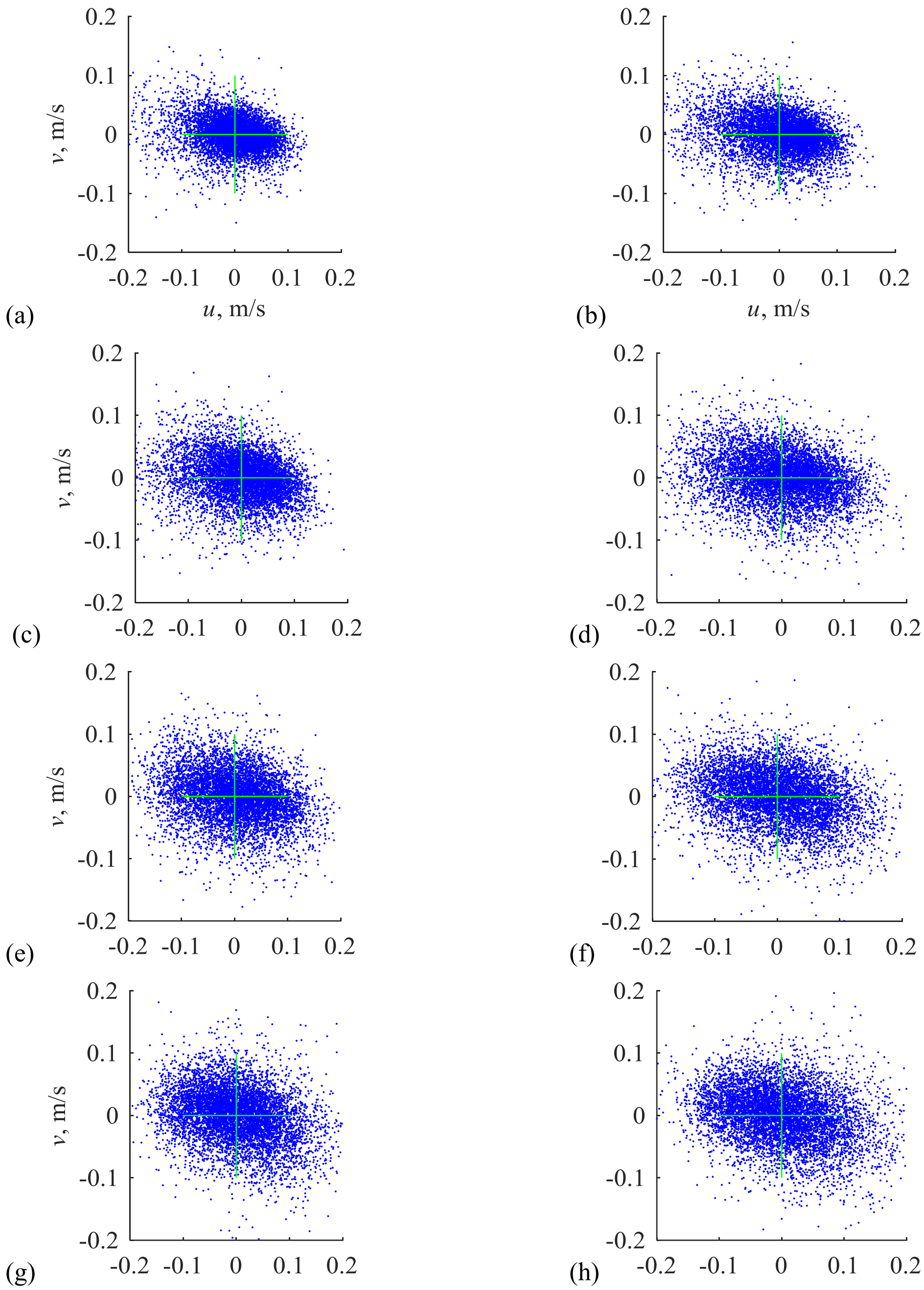

Figure 5.15 Quadrant analysis for all flow fields at points 9 (a) to 16 (h) located at Y=0.182H.

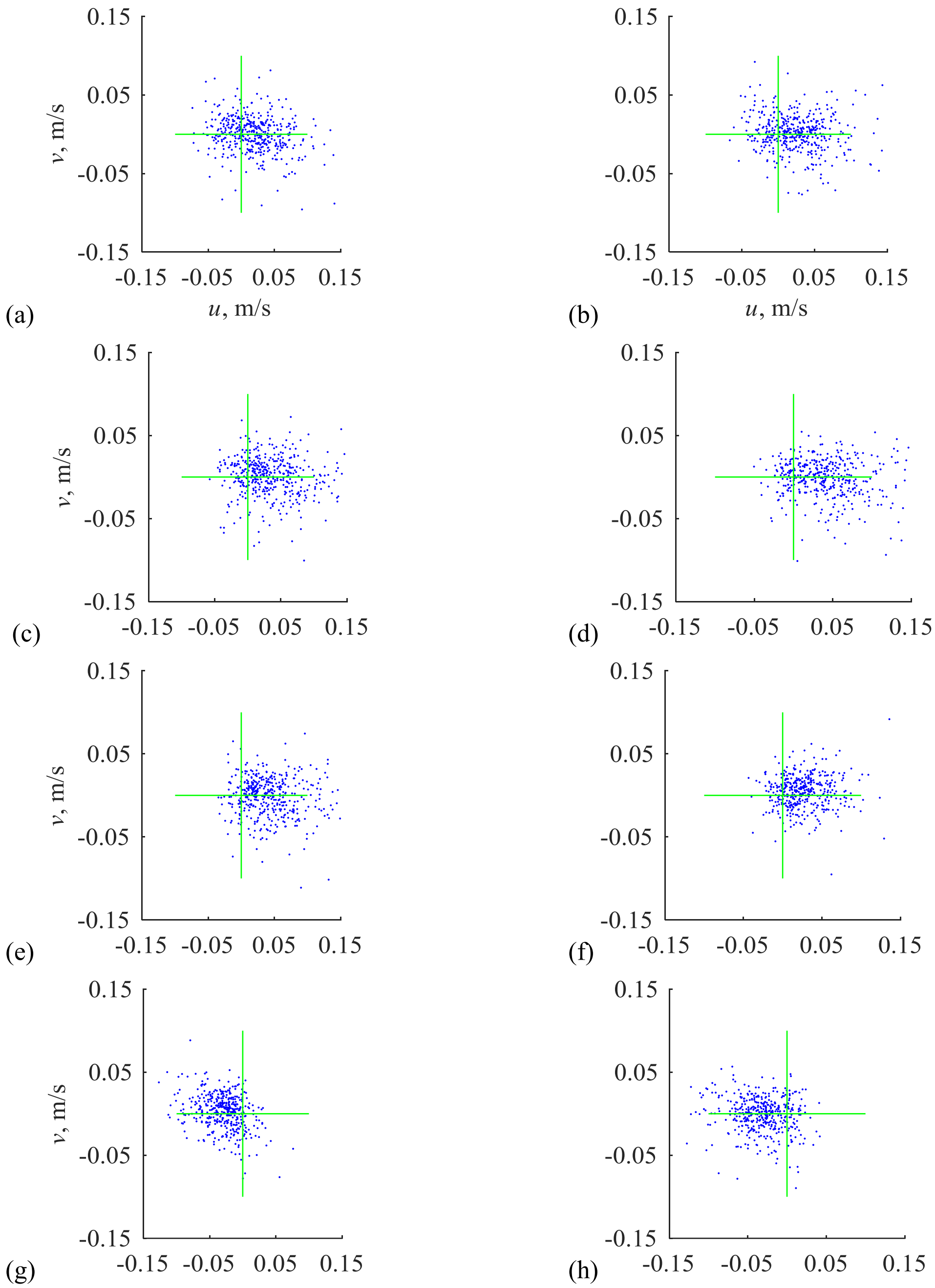

Figure 5.16 Quadrant analysis for flow fields with single detachments at points 1 (a) to 8 (h) located at Y=0.0303H.

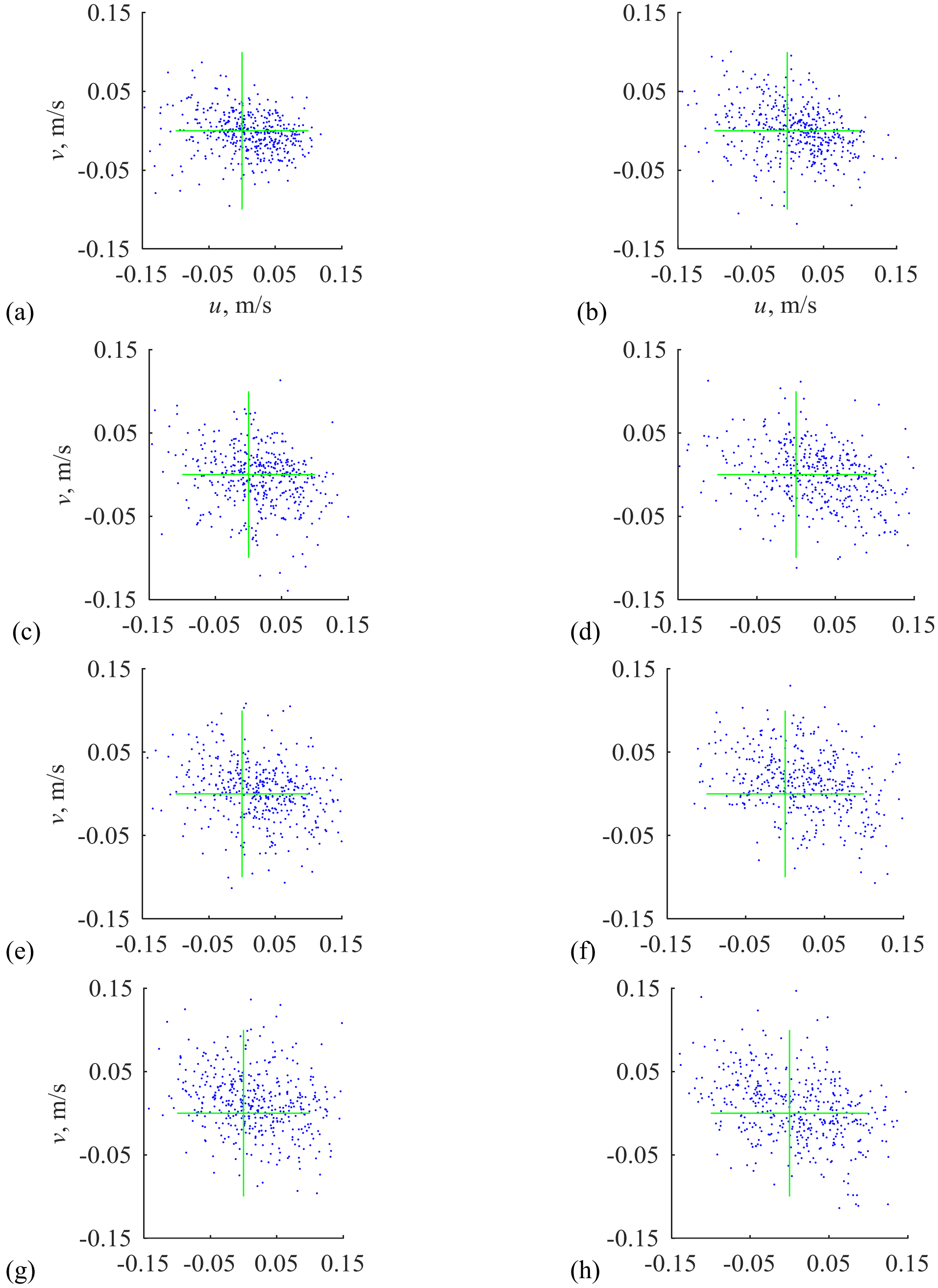

Figure 5.17 Quadrant analysis for flow fields with single detachments at points 9 (a) to 16 (h) located at Y=0.182H.

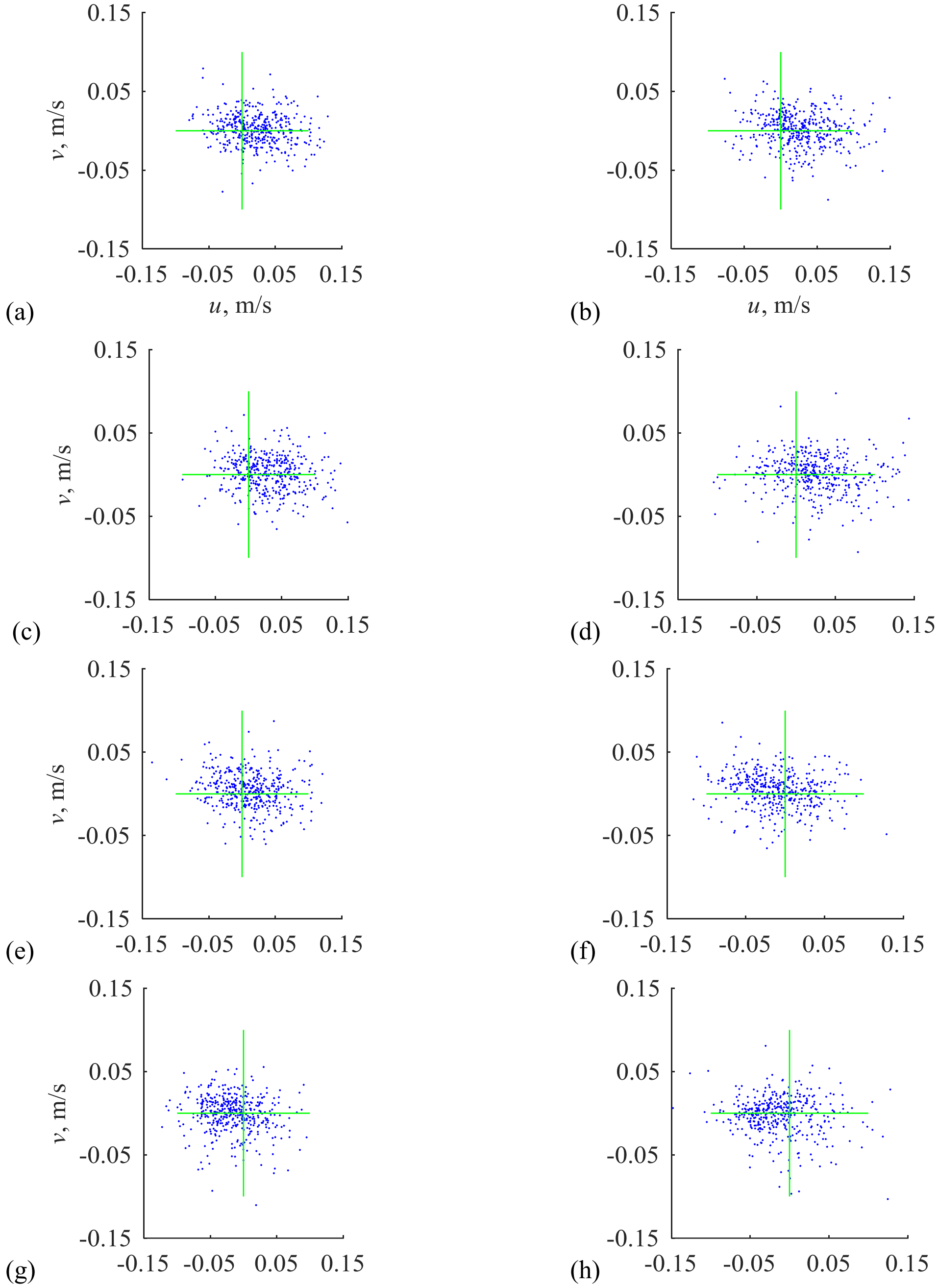

Figure 5.18 Quadrant analysis for the flow fields captured at $t_0-\Delta t$ with respect to single-detachment flow fields at points 1 (a) to 8 (h) located at Y=0.0303H.

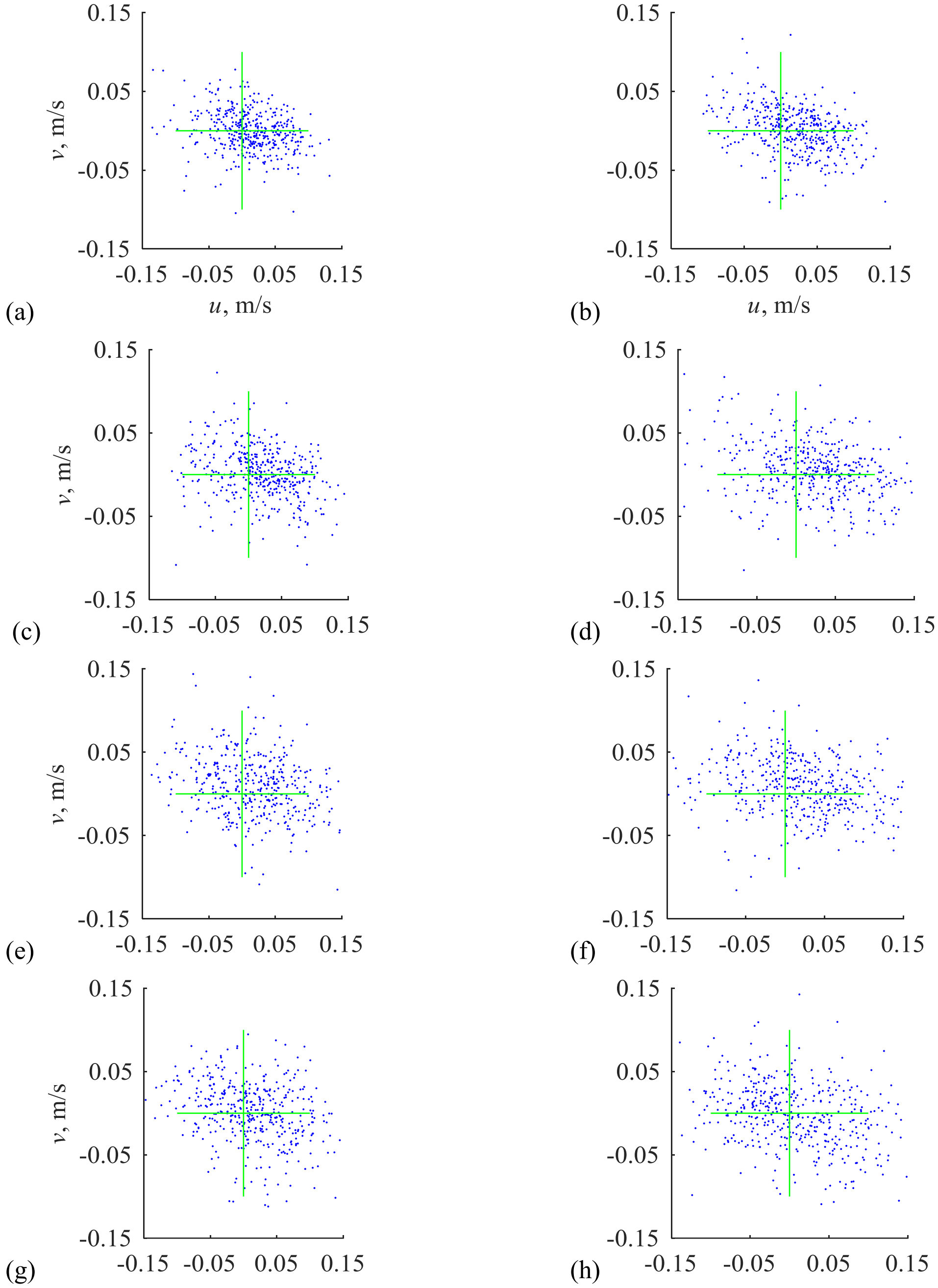

Figure 5.19 Quadrant analysis for the flow fields captured at $t_0 - \Delta t$ with respect to single-detachment flow fields at points 9 (a) to 16 (h) located at Y=0.182H.

5.4 Proper orthogonal decomposition analysis

The POD analysis is performed on planar PIV flow fields to capture the most energetic flow motions. As described in section 4.3, the POD modes are generated using equation (4.4). Using these modes and their coefficients, a_n, calculated as $\psi^T \boldsymbol{u}^n$, the fluctuation velocity field can be reproduced for each flow field as discussed in section 4.3 with more details. The portion of kinetic energy of each mode compared with total kinetic energy is shown in Figure 5.20. The first six planar POD modes contain around 50% of the kinetic energy combined, and each of the rest of the modes contain less than 3% of the total kinetic energy. The first two modes have the most significant energy portions (22% and 11%) and the energy portion of the remaining modes decreases gradually with mode number.

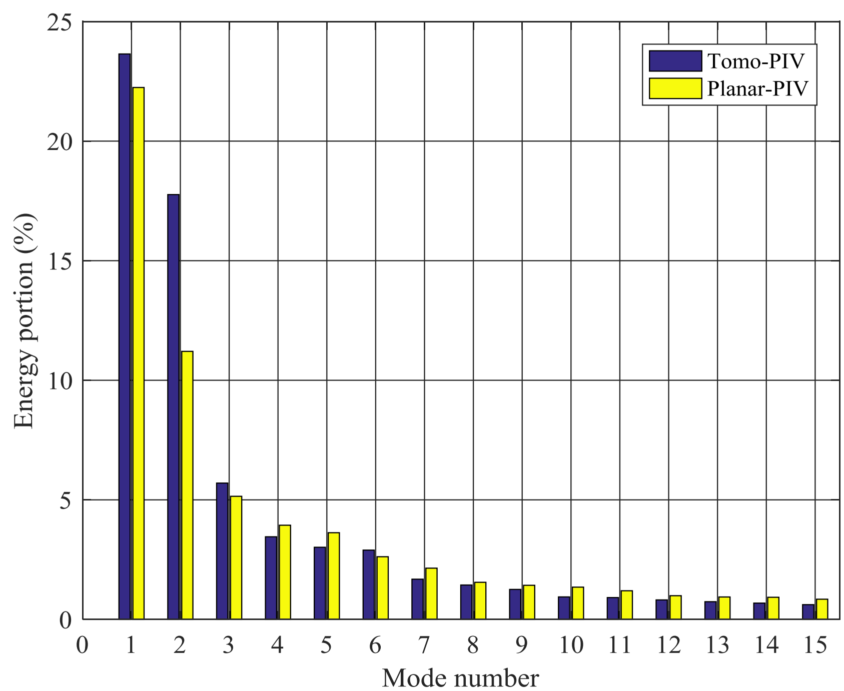

Figure 5.20. Energy distribution of planar PIV and Tomo-PIV POD modes normalized by total kinetic energy.

The vector field of Mode 1 is shown in Figure 5.22 (a), which is an almost uniform field with streamwise direction. The maximum vector magnitude in Mode 1 is close to the wall at the upstream of the FOV and it moves away from the wall as it reached the detachment point. This distribution is similar to the distribution of Reynolds shear stress as shown in Figure 5.7 (a). This similarity can be explained by the fact that the region containing high Reynolds stress is caused by the passage of large structures as they move away from the wall at the detachment point. These large structures contain strong u and v fluctuations and therefore contain high amount of kinetic energy, which justifies this region with high magnitude vectors in the first POD. As the coefficient of this mode, a_1, can have both positive and negative values, it represents the variation of u in the FOV. Therefore, for the flow fields that have significant positive a_1, considering that this mode has backward motion, U has low values close to the wall and therefore the flow detachment occurs upstream its location in the average flow field.

The second POD mode contains a large backward motion upstream, a large forward motion downstream and a separating region with low magnitude vectors appearing almost at the location of the shear layer as shown in Figure 5.22 (b). This separation region originates at the wall at around $X = -0.3$, moves downstream and away from the wall and contains downward motion.

Mohammed-Taifour et al. (2016) presented two dominant motions of a separated flow using POD modes and described first and second POD modes as breathing and shedding motions respectively. A similar description is applicable to the first two calculated modes here, although the flow geometries are completely different. The breathing motion represents the movement of the separation line or the change in the size of the recirculation zone, therefore, the coefficient of this mode should determine the size of the recirculation zone. To prove this, the first mode is multiplied by different coefficients and added to the average velocity field. The results show that different coefficients of mode 1 are controlling the separation line and size of the recirculation zone; therefore, the coefficients of mode 1 (a_1) determines the bubble size and their variation from one vector field to another represent movements of separation line or breathing motion. By applying same procedure to mode 2, the change is visible for the strength of shear layer. For high-magnitude a_2 coefficients, the back flow strength increases and velocity gradient close to the separation point also increase, which is equivalent to increase in the strength of vortices passing this region.

The third POD mode shows a strong vortex that appears above the detachment point with the center located at around X=0.1 and Y=0.3 as shown in Figure 5.22 (c). As the vortex is located close to the shear layer, it can represent the strength of vortices existing at the shear layer. The fourth mode contains two large motions upstream of the FOV and more downstream close to the wall in addition to a backward motion downstream of the FOV and away from the wall as shown in Figure 5.22 (a). The fifth mode contains two large counter-rotating vortices that are separated from each other at around X=0 and their centers are located at around Y=0.15 as shown in Figure 5.22 (a). In the sixth POD mode, the direction of the vector fields have changed several times as shown in Figure 5.22 (f). Starting from the upstream of the FOV, the flow changes from forward to backward, backward to forward, and again forward to backward motion.

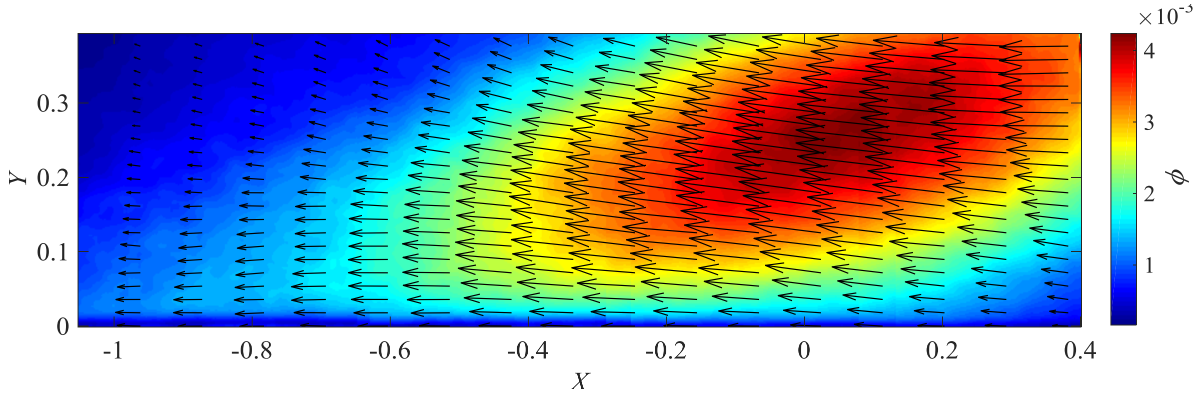

(a) $\boldsymbol{\phi}^1$

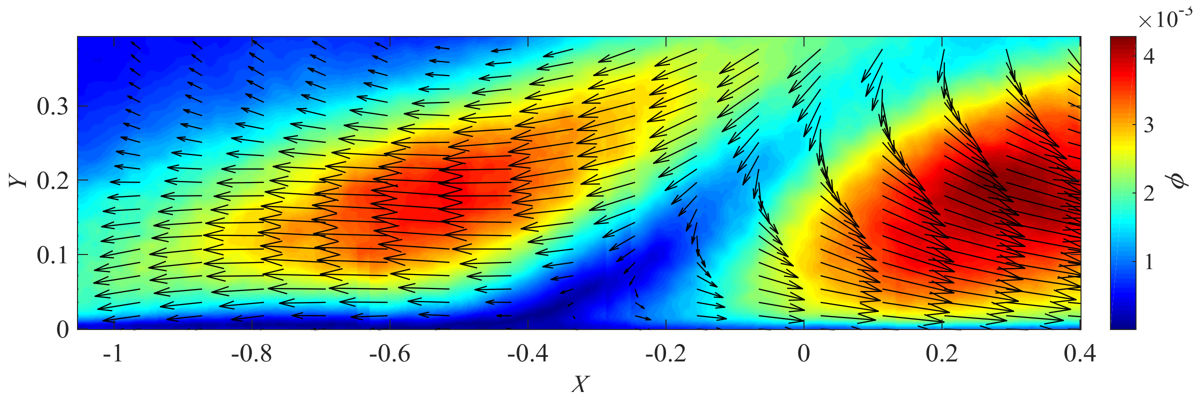

(b) $\boldsymbol{\phi}2$

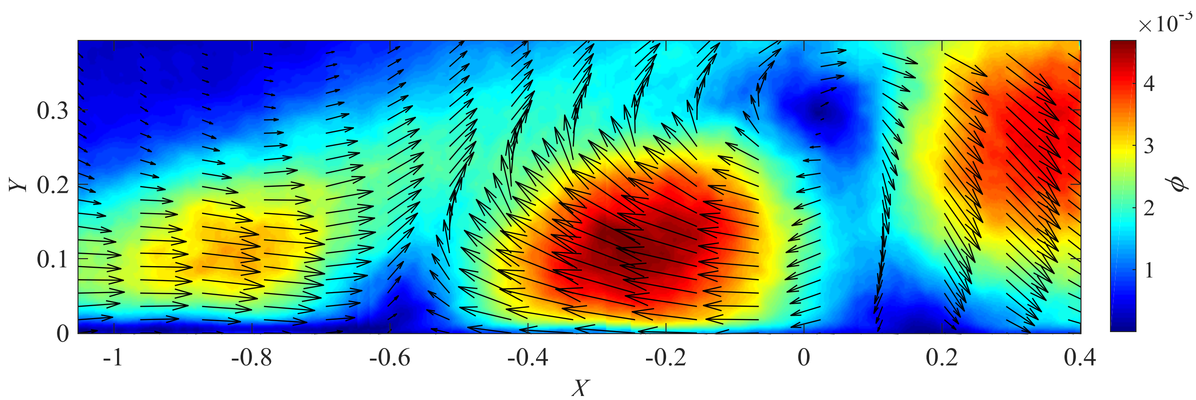

(c) $\boldsymbol{\phi}3$

Figure 5.21 The normalized POD (a) first, (b) second, (c) third, modes with energy portions of 22%, 11% and 5%, respectively.

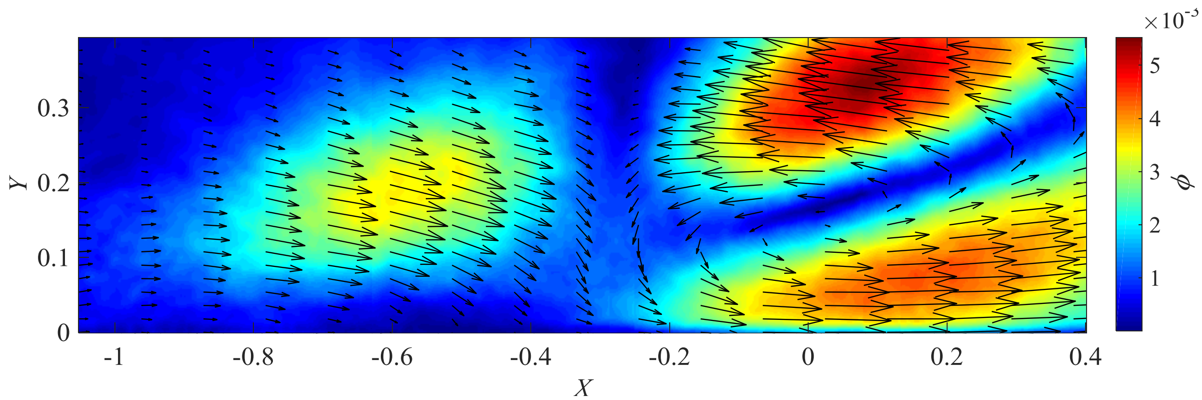

(a) $\phi 4$

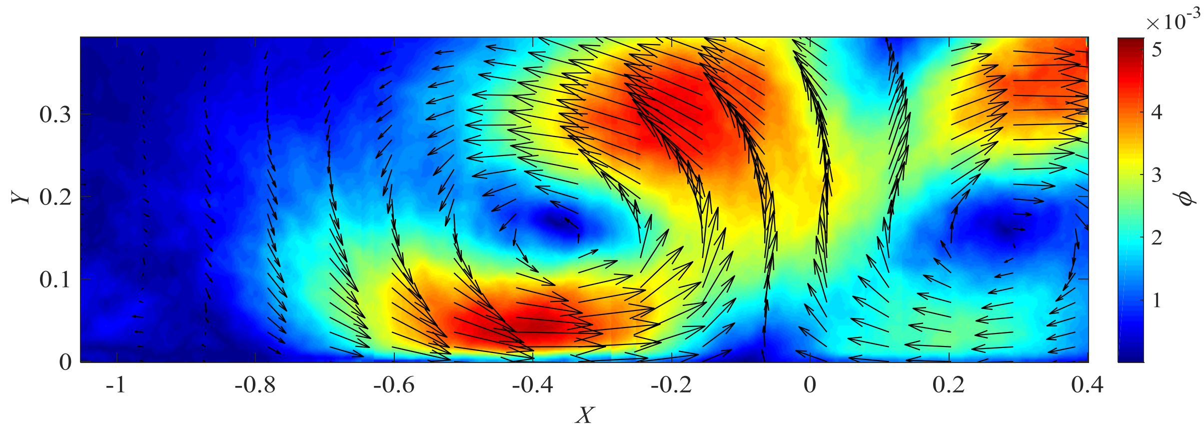

(b) ϕ^5

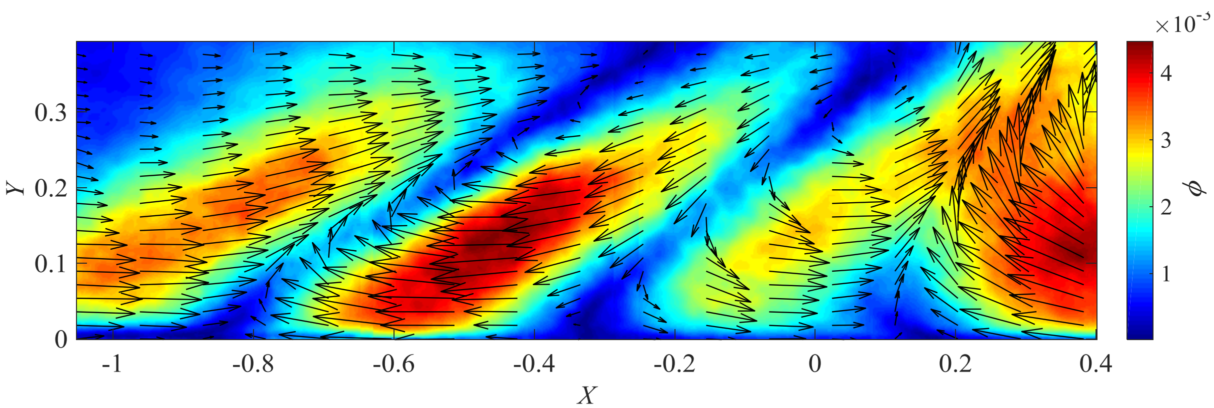

(c) ϕ^6

Figure 5.22 The normalized POD, (a) fourth, (b) fifth and (c) sixth modes with energy portions of 4%, 3.8% and 3% respectively.

5.5 Conclusion

The results from planar PIV measurements are presented in this chapter. To summarize, the results suggest that a recirculation region has appeared downstream of the FOV, and similar to two-dimensional flow separation, the probability of backward motion increases from the upstream to the downstream of the FOV. There are also similarities between the distributions of Reynolds shear stresses of this three-dimensional separated flow and the ones reported by the studies on two-dimensional flow separation. The distributions of third-order moments and turbulence productions suggest that turbulence is being convected away from the high-turbulence region. A high-speed structures is detected upstream of the detachment point for the instant of single-detachments in this analysis and it is being convected upstream for the instants ahead of the single-detachment events. This coherent structure is also monitored in the quadrant analysis. The POD analysis reveals the most energetic motions in the flow, which are associated to the movement and the strength of the shear layer.

Chapter 6 Three-dimensional flow field

The three-dimensional properties of the separated flow are investigated using Tomo-PIV measurements. As discussed in chapter 3, the measurement volume contains the region from the wall to 12 mm (Y=0.72H) away from the wall, 75 mm (ΔX=0.45H) in streamwise, and 70 mm (ΔZ=0.42H) in spanwise directions. Although strong structures occur further from the wall as discussed in Chapter 5, the structures captured in the conditional averaging of planar vector fields have strong signatures close to the wall (Y = 0 to 0.1H), and their existence can be confirmed in this section. The origin of the coordinate system is located at the detachment point where $\partial\langle U\rangle/\partial y=\partial\langle W\rangle/\partial y=0$ at the wall, which coincides with center of the vortex. The coordinate system is normalized by H=165 mm. The flow decelerates upstream until it detaches from the wall at X=0, and a recirculation zone forms and extends downstream of the FOV.

6.1 Mean flow field

The magnitude of average velocity, $|\boldsymbol{U}| = (\langle U\rangle^2 + \langle V\rangle^2)^{1/2}$, is shown in Figure 6.1 to compare its pattern with the one captured by planar PIV measurement. However, the vector field is averaged over Z planes of −0.01H to 0.01H to increase the convergence of the flow and reduce the effect of random noise, and at the same time it still represents the cross section flow at Z=0. Same normalization of the coordinate system used for planar field is applied here. The maximum magnitude of velocity is 0.025 m/s, which occurs upper left corner of the FOV. The white contour shows the region with almost zero velocity. The backward flow occurs downstream of the separation line with maximum magnitude of 0.01 m/s appears downstream of the white contour. The velocity vector field at Z=0 plane is shown in Figure 6.2. Due to the finite spatial resolution and presence of ghost particles in MART reconstruction (Elsinga et al. 2006), the velocity does not converge to zero at the wall and a region with significant wall-normal velocity has appeared upstream of the FOV. The backflow region forms at $X > 0$ and grows in wall-normal directions and reaches about Y=0.04H at X=0.2H.

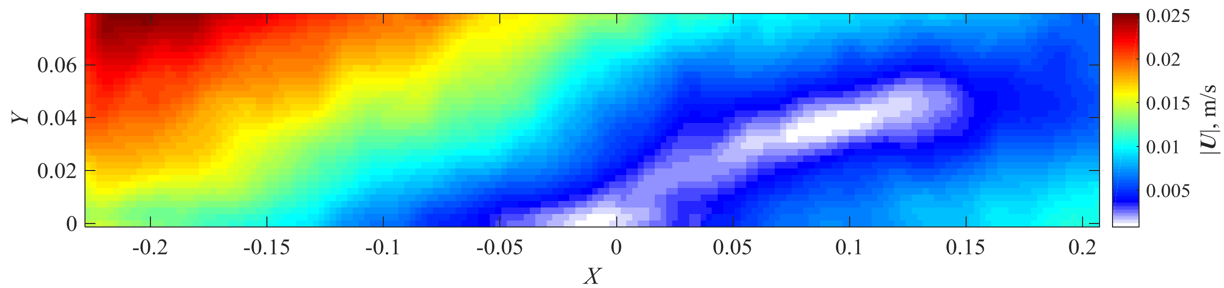

Figure 6.1 Magnitude of velocity, $|\boldsymbol{U}|$ (m/s) averaged over Z=−0.01H to 0.01H. The streamwise velocity decreases along streamwise direction, and close to the wall, it reaches almost zero and backward flow appears more downstream.

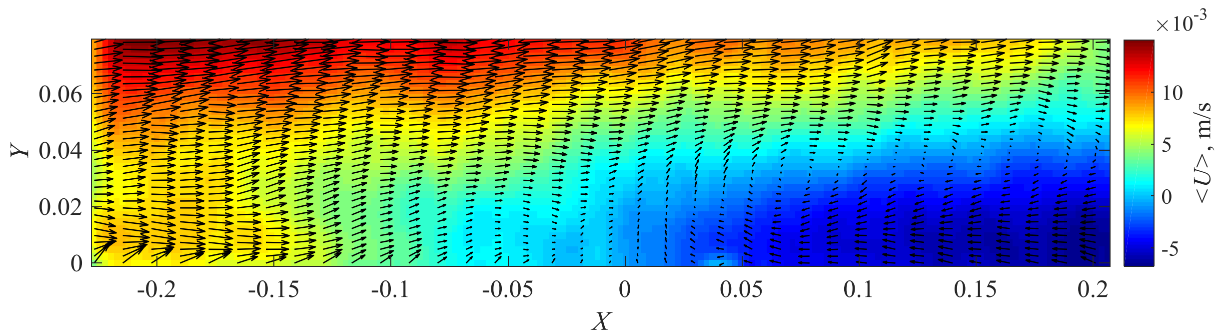

Figure 6.2 Mean velocity vector field with background colormap of streamwise velocity $<U>$ (m/s) averaged over Z=−0.01H to 0.01H. The vector field is spatially decimating by the factor of 2 in streamwise direction for better visualization.

The three-dimensional streamlines of velocity are shown in Figure 6.3. The rotational movement of the streamlines around a center point shows a tornado like flow structure appears in this view, which is a vortex with the axis in Y direction and is inclined toward X direction. The XZ views of the flow vector field are shown in Figure 6.4. This view also shows the rotational motion with Y axis of rotation and suggest that the change in the direction of streamwise velocity occurs at different streamwise locations for different spanwise locations. Strong forward flow exists upstream and at negative Z values, and strong backflow appears downstream at positive Z values. The center of the foci appears at X=0.04 and Z=0 close to the wall (Y=0.01) as shown in Figure 6.4 (a), and it has moved in X and Z directions for Y=0.06 and reaches X=0.1 and Z= −0.04. This large structure indicates the three-dimensional nature of the separated flow. In three-dimensional separated flows, foci structures saddle points and node points play critical roles in describing the flow patterns close to the wall (Délery, 2013). Duquesne et al. (2015) also reported several saddle and foci structures appearing at the diffuser wall of a turbine. In the three-dimensional separation bubble model proposed by Surana et al. (2006), among different separation flow patterns, two spiral flow structures appear at the separation line. In this model, the zero-friction lines connect the two spiral structures, and a detachment line forms between the two structures and terminates at the center of the spiral structures (Surana et al. 2006).

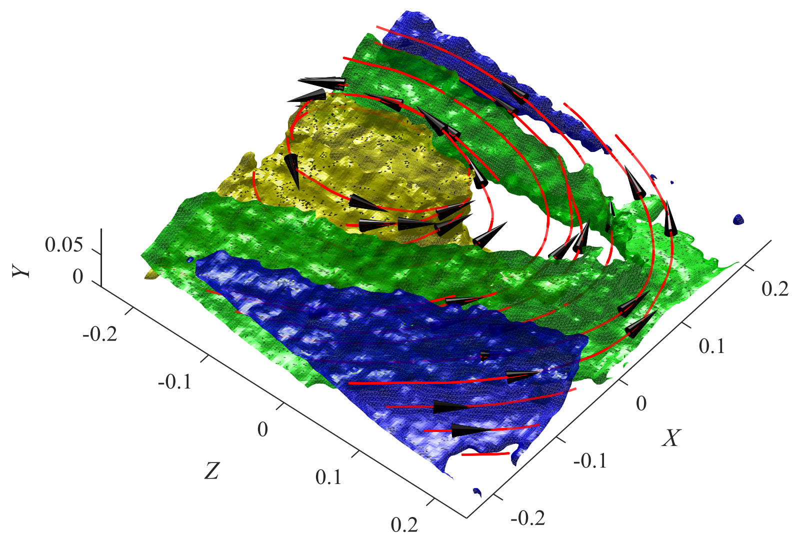

Figure 6.3 Tomo-PIV FOV with contours of $|\boldsymbol{U}|$=0.025 m/s (blue), $|\boldsymbol{U}|$=0.015 m/s (green) and $|\boldsymbol{U}|$=0.005 m/s (yellow).

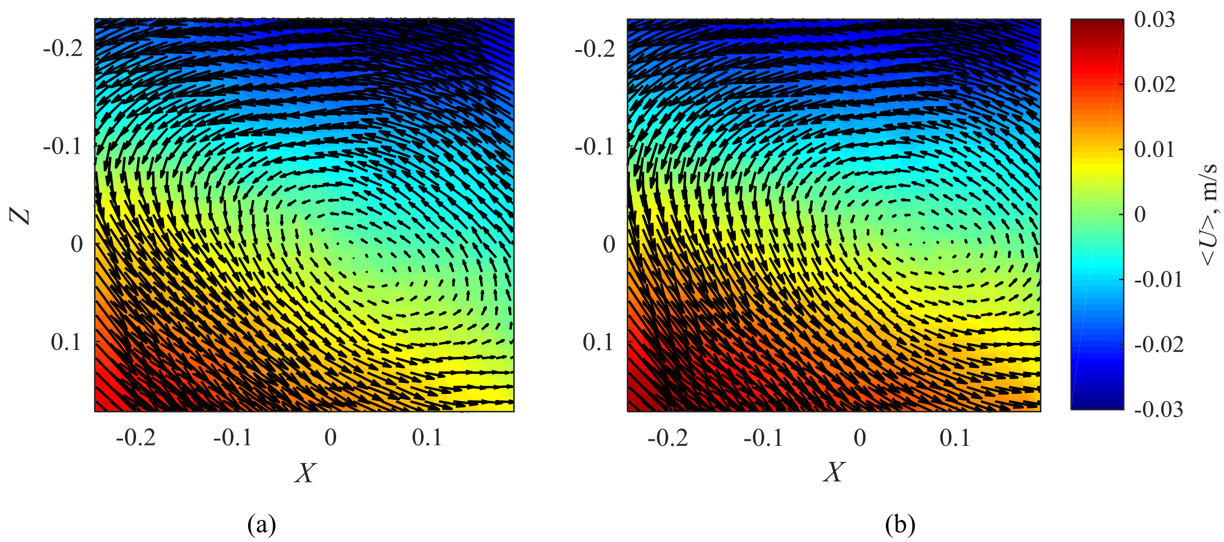

Figure 6.4 Mean velocity vector field with background colormap of streamwise velocity, $<U>$ (m/s) at (a) Y=0.01H (XZ plane) and (b) Y=0.03H (XZ plane). The vector field is spatially down sampled by the factor of 2 for better visualization.

The distribution of γ is shown in Figure 6.5. The distribution is averaged over the entire data points along the Z direction. Close to the wall, γ varies from 52% to 62%. In contrast to planar PIV results and the study by Simpson et al. (1996), at the detachment point, γ is 55%, and the detachment located upstream of TD point. This variation was explained before in the planar results (chapter 5.1) and is associated with the asymmetry of probability distribution of velocity at the detachment point.

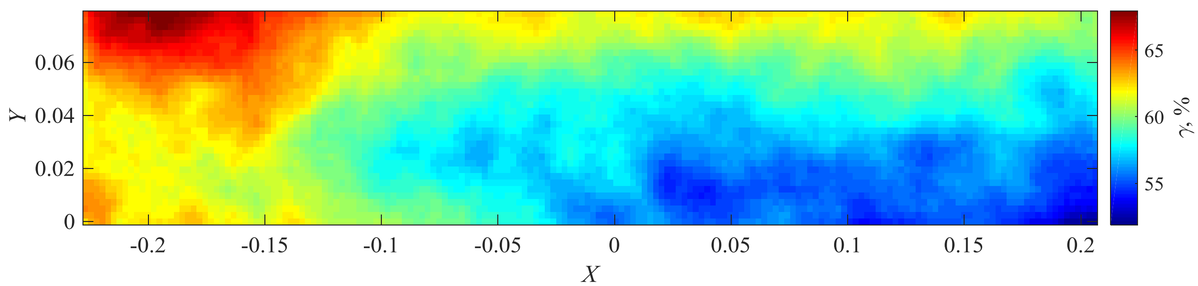

Figure 6.5 Distribution of γ (%) averaged along Z direction. The γ values at the wall appears between 52% to 62% in the FOV. The detachment point located upstream of γ=50%.

6.2 Three-dimensional characterization of structures at separation instants

Similar to the conditional averaging procedure performed for planar data and utilizing considerations explained in chapter 4.2, single-detachment tomographic flow fields are found among the rest of the flow fields. The detected flow fields are analyzed in order to extract the involved structures. In this case, the flow fields help characterize three-dimensional properties of these structures. Similar to the analysis performed for planar flow fields, the velocity fields captured at Δt and $2\Delta t$ before single-detachment flow fields are also averaged to track and detect potential structures in time.

6.2.1 Single-detachment vector fields

The moving windows as explained in chapter 4.2 are assigned to each flow field with single-detachment to capture velocity field within $-0.15H < X < 0.2H$. Similar to two-dimensional conditional averaging, the detachment points on Z=0 plane are assigned to the origin of the moving windows; therefore, by averaging over the moving windows, the detachment points stay at the origin and the average properties of the structures appear around the detachment points.

Figure 6.6 shows the conditionally average of instantaneous velocity vector field, $\boldsymbol{U_c}$ containing the three componenets of velocity. As expected, the flow detaches from the wall at around X=0, and backflow appears downstream as shown in Figure 6.6 (a). The structures appear at the flow detachments are not symmetric in Z direction as shown in Figure 6.6 (b). The orientation of the three-dimensional contours of streamwise velocity is shown in Figure 6.6 (c). The streamwise velocity has general decrease in X direction; however, the contours have angles with both X and Z axes.

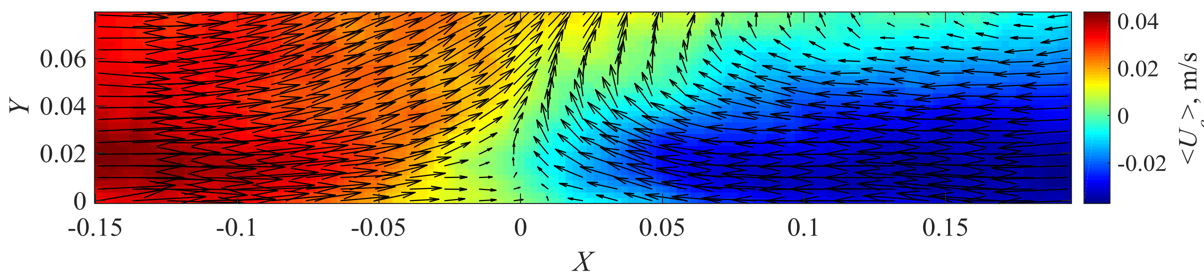

(a)

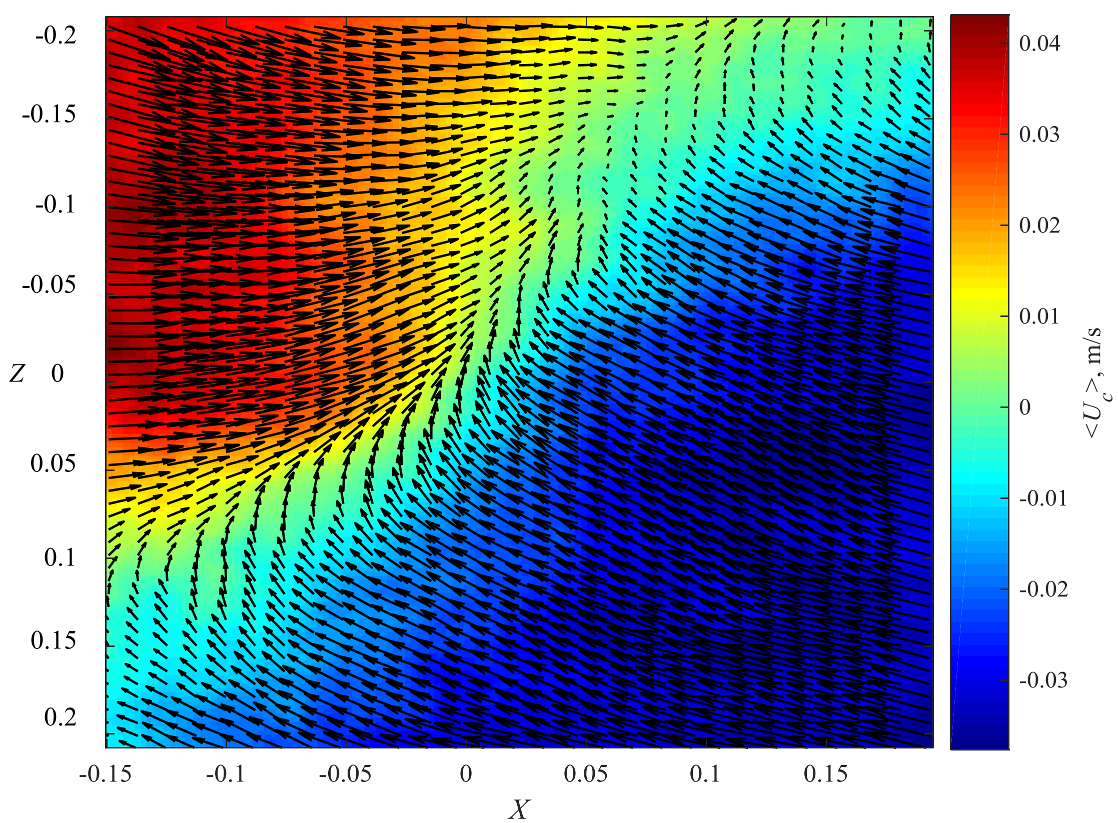

(b)

Figure 6.6 Conditional average of instantaneous flow field for single-detachment velocity fields shown in (a) *XY* (*Z*=0) plane with background map of <U_c> and (b) *XZ* plane (*Y*=0.03).

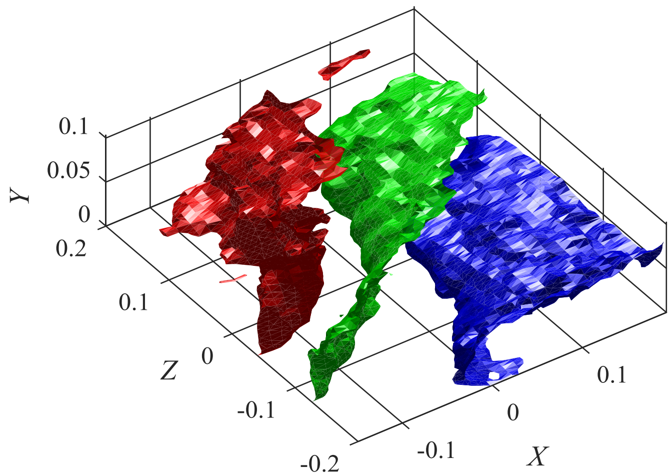

Figure 6.7 Conditional average of instantaneous flow field for single-detachment velocity fields shown in three-dimensional contours of streamwise velocity. Detachment is located at X=0. Red contour shows iso-surface of streamwise velocity of $<U_c>$=0.02 m/s, green shows $<U_c>$=0, and blue shows $<U_c>$=−0.02 m/s.

Conditional averaging over fluctuation components of velocity vector field, $\boldsymbol{u}_c$, contains three components of fluctuation velocity. However, $\boldsymbol{u}_c$ represents almost symmetric vector field with respect to Z=0 plane as shown in Figure 6.8. The velocity vector field of $\boldsymbol{u}_c$ at Z=0 plane is shown in Figure 6.8 (a). The xy view of $\boldsymbol{u}_c$ shows almost same vector pattern of $\boldsymbol{U}_c$ distribution as shown in Figure 6.6 (a). This velocity field suggests that a region upstream of the detachment point has positive streamwise fluctuation velocity ($u=U - <U> > 0$) for single-detachment flow fields where $<U>$ is average streamwise velocity. Although fluctuation vector field contains positive w component, which shows antisymmetric feature of the field, the u component shows almost symmetric patterns with respect to Z=0 plane. Contours of u components also have almost symmetric orientations as shown in Figure 6.6 (c). It is also possible to observe the coherence and extend of the high-speed and low-speed regions in spanwise direction.

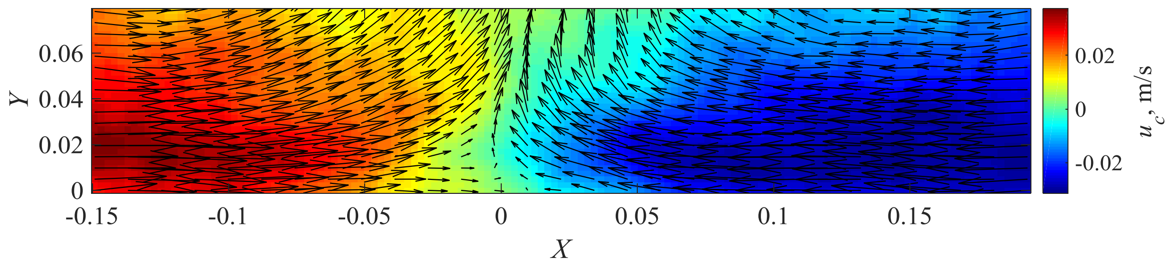

(a)

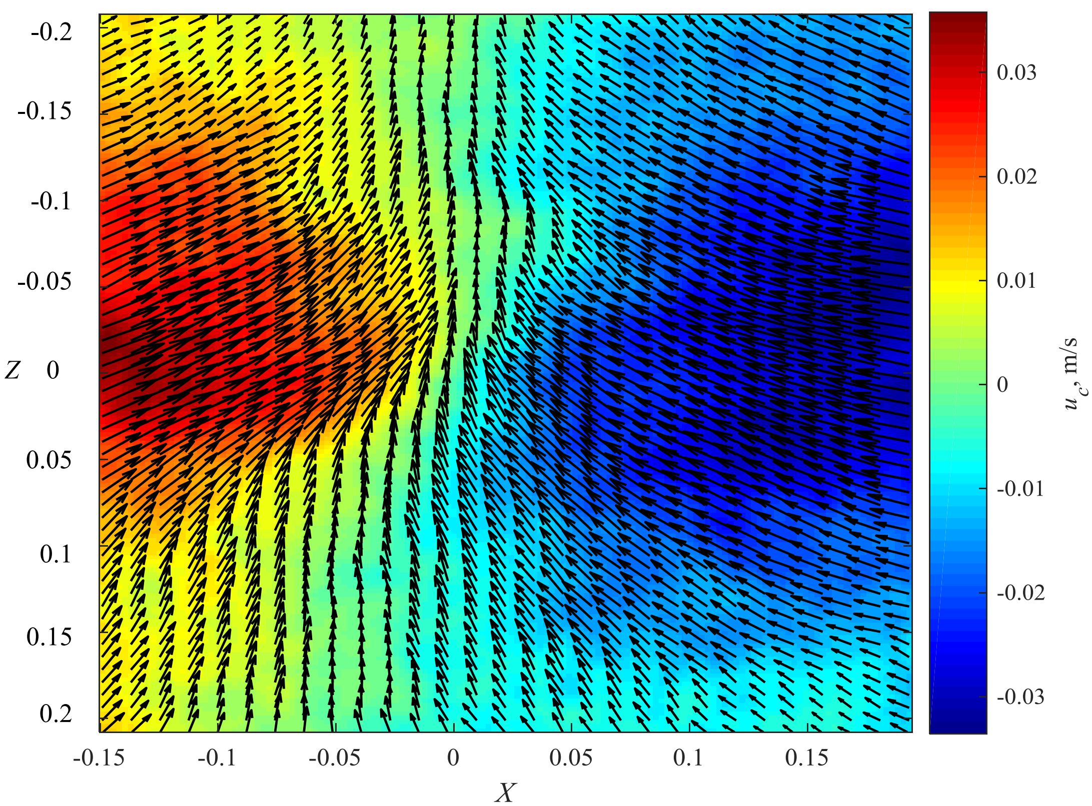

(b)

Figure 6.8 Conditional average of fluctuation velocity field for single-detachment vector fields shown in (a) *XY* plane (*Z*=0) with background map of u_c and (b) *XZ* plane (*Y*=0.03*H*).

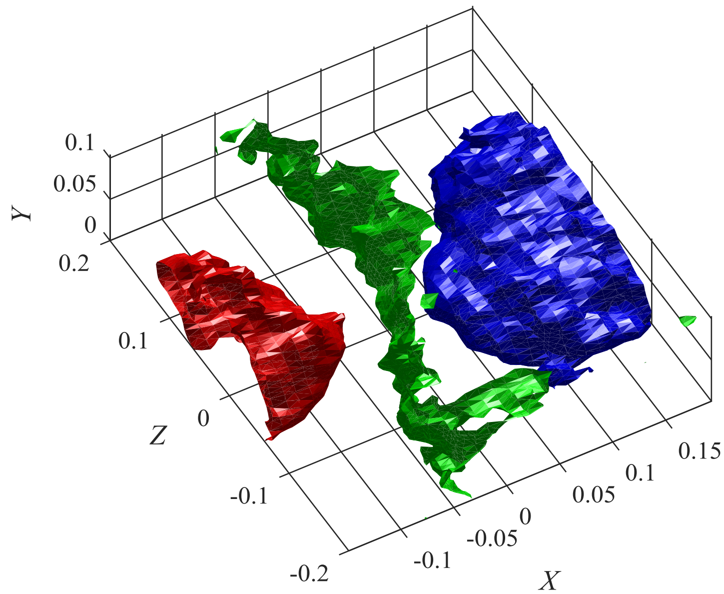

Figure 6.9 Conditional averaged fluctuation velocity, $\boldsymbol{u_c}$, for single-detachment vector fields shown in three-dimensional contours of streamwise fluctuation component. Red contour shows iso-surface of u_c=0.02 m/s, green shows u_c=0 and blue shows $u_c = -0.02$ m/s.

6.2.2 Flow fields captured at $t_0 - \Delta t$

Single-detachment flow fields are tracked in time to provide insight to how the detected structures have evolved before flow detachments. Considering the single-detachment flow fields occur at t_0, conditional averaging of vector fields captured at $t_0 - \Delta t$ are shown in Figure 6.10 and Figure 6.12 for instantaneous and fluctuating flow fields, respectively. The instantaneous flow field as shown in Figure 6.10 (a) shows that the detachment point has convected upstream compared with the flow pattern captured at t_0 as shown in Figure 6.6 (a). Although the flow pattern remains almost the same comparing Figure 6.6 and Figure 6.10, the detachment point has obviously moved upstream. The orientations of the streamwise velocity contours show also that the detachment line has moved upstream as shown in Figure 6.10 (c). Conditional averaging over fluctuation components as depicted in Figure 6.10 also shows a similar pattern. The fluctuation flow field as shown in Figure 6.10 (a) proves the existence of a high-speed region (u_c>0) convected upstream of the flow detachment. This high-speed region, which has also been detected in planar measurements, is a consistent structure appearing upstream of bin −1 flow detachments and also can be the structure that initiates flow detachment or pushes the flow detachment downstream. The *XZ* view of the fluctuation pattern also shows the convected high-speed region as shown in Figure 6.10 (b). Similar to Figure 6.6 (b), the w component has considerable positive values, which suggests that the detected structure is antisymmetric in spanwise direction. However, the u component does not show any specific orientation in spanwise direction as shown in Figure 6.10 (c). The orientation of the u-component contours shows that the low-speed and high-speed regions detected in Figure 6.6 (c) have convected upstream for $t_0-\Delta t$ vector fields as shown in Figure 6.10 (c).

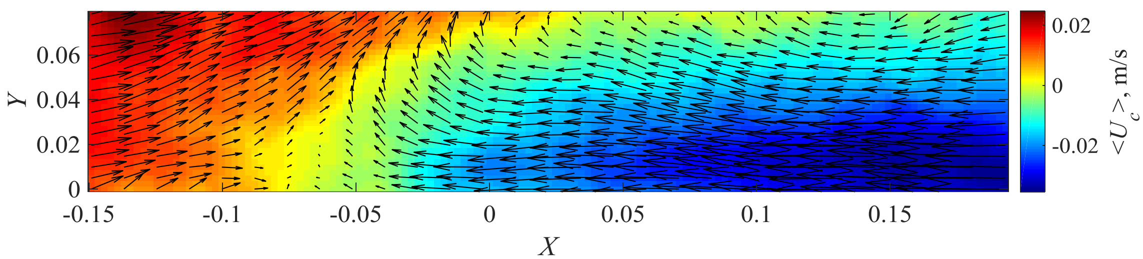

(a)

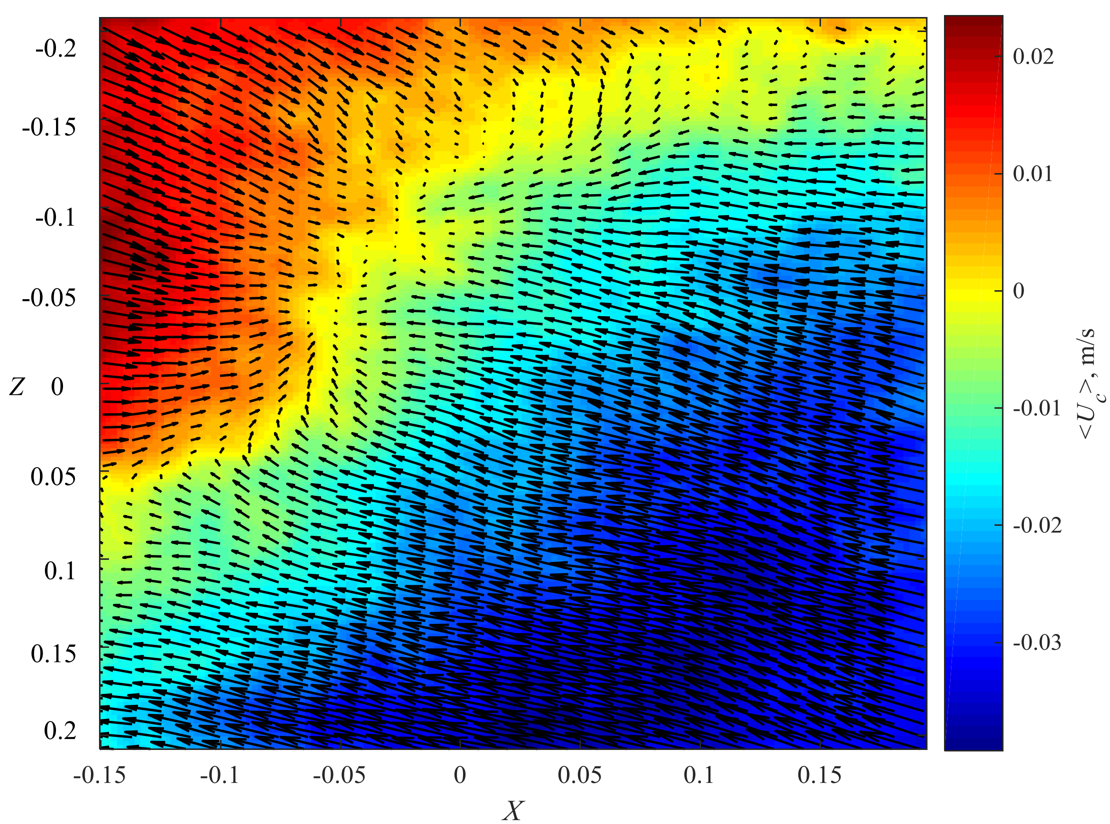

(b)

Figure 6.10 Conditional averaged of instantaneous velocity vector field, $\boldsymbol{U}_{\mathrm{c}}$ at $t_0-\Delta t$ shown in (a) XY plane (Z=0) with background map of $<U_c>$ and (b) XZ plane (Y=0.03H). Red contour shows iso-surface of streamwise velocity of $<U_c>$=0.02 m/s, green contour shows $<U_c>$=0 contour, and blue contour shows $<U_c>$= −0.02 m/s.

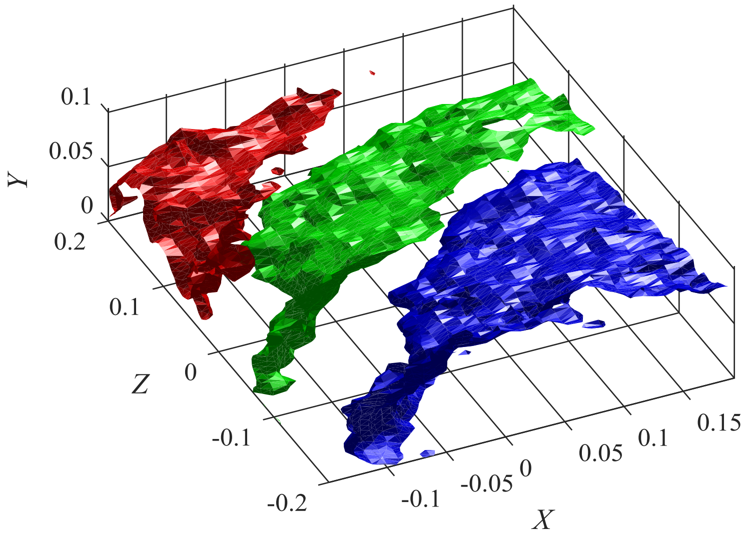

Figure 6.11 Conditional averaged of instantaneous velocity vector field at $t_0-\Delta t$ shown in three-dimensional contours of streamwise fluctuation component. Red contour shows iso-surface of streamwise velocity of $\langle U_c\rangle=0.02$ m/s, green contour shows $\langle U_c\rangle=0$ contour, and blue contour shows $\langle U_c\rangle=-0.02$ m/s.

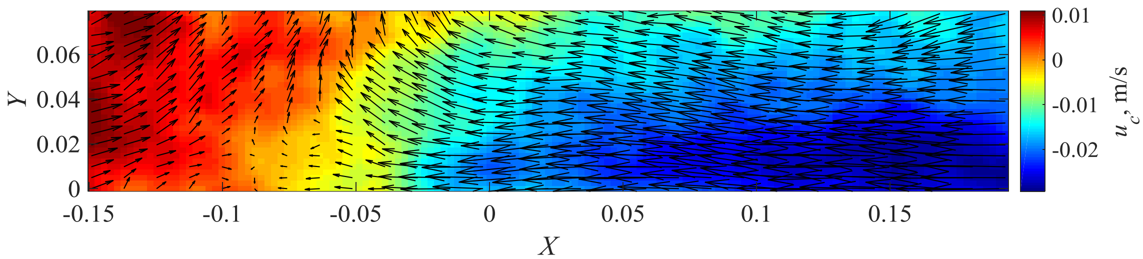

(a)

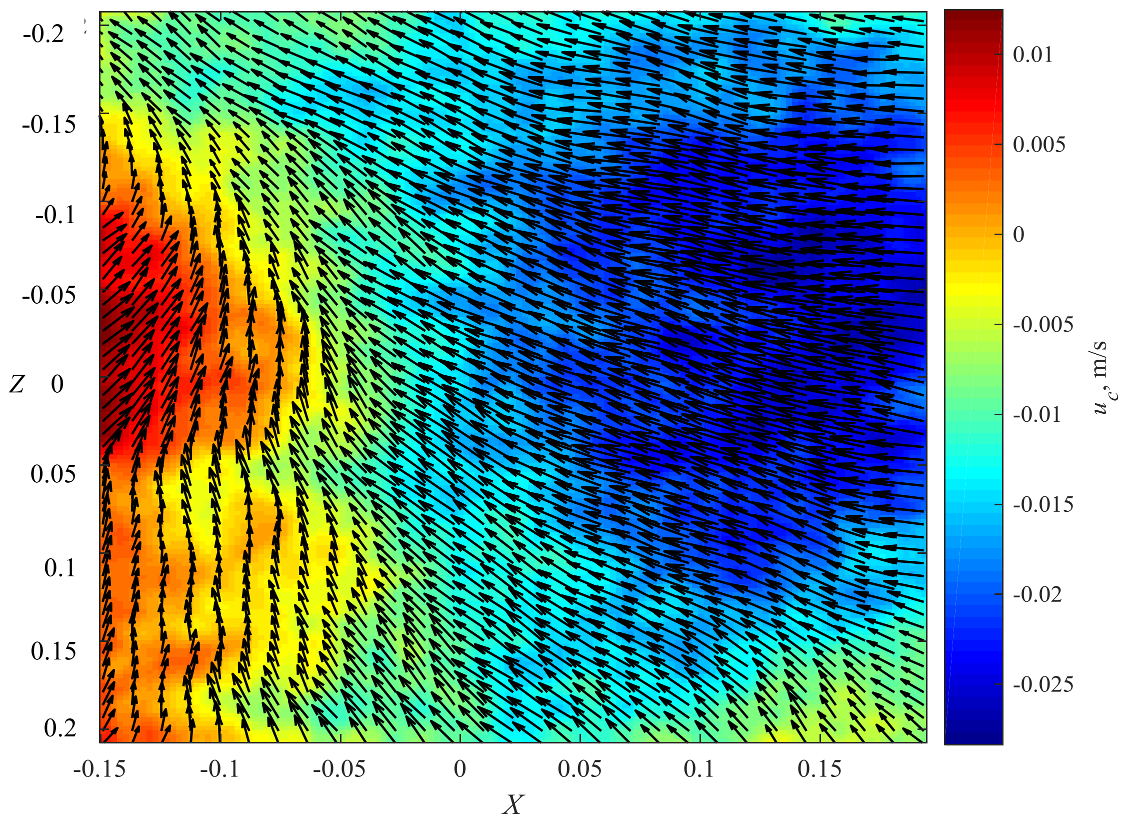

(b)

Figure 6.12 Conditional average of fluctuation velocity flow field, $\boldsymbol{u}_c$ at $t_0-\Delta t$ shown in (a) XY plane (Z=0) with background map of u_c, and (b) XZ plane (Y=0.03).

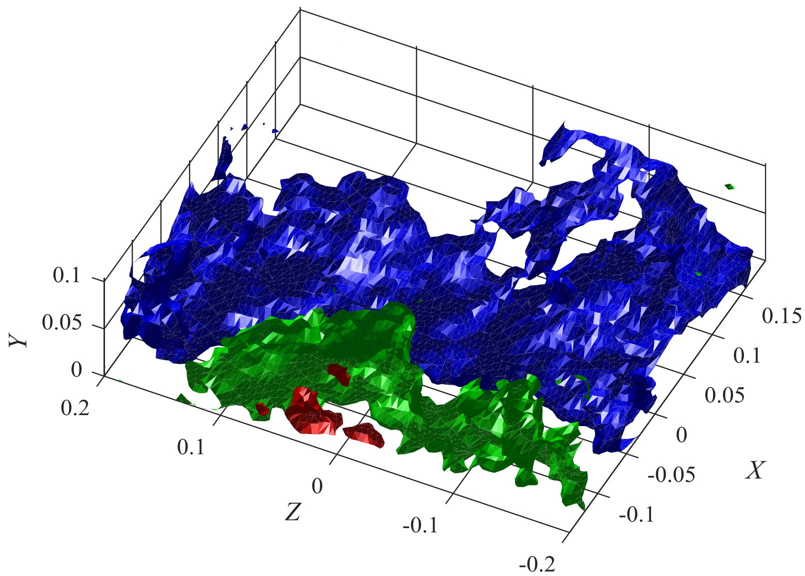

Figure 6.13 Conditional average of fluctuation velocity flow field, $\boldsymbol{u}_c$ at $t_0-\Delta t$ shown in three-dimensional contours of streamwise fluctuation component, red contour shows iso-surface of u_c=0.01 m/s, green shows u_c=0, and blue shows u_c =−0.01 m/s.

6.2.3 Flow field captured at $t_0 - 2\Delta t$

By investigating the flow fields captured 2Δ*t* before the single-detachment flow fields; it is possible to track the structures further in time. For flow fields captured at $t_0-2\Delta t$, the detachment structure has convected more upstream and it is mostly out of the FOV as depicted in Figure 6.14 (a); therefore, a backflow region has appeared and covered almost the entire FOV. Fluctuation components as shown in Figure 6.16 also suggest a low-speed region covering the entire FOV. Figure 6.16 (b) still suggests asymmetry with respect to *Z*=0 plane. Comparing with Figure 6.5 (c), Figure 6.10 (c) and Figure 6.14 (c) proposes that the streamwise contours have convected upstream keeping almost same orientation, and they still show asymmetry in spanwise direction. This can suggest that the detected structure is being pushed downstream and also in –*Z* direction likely keeping its shape and orientation. However, the contours are more inclined toward *X* direction in flow fields captured at $t_0-2\Delta t$, suggesting that the backflow is weaker and the backflow region is shallower in previous flow fields. Same evolution can also be observed in conditional averaging analysis of planar flow fields. Figure 6.16 shows almost same pattern for fluctuation components. Figure 6.16 (b) suggests a relative symmetry for fluctuation components at least close to Z=0 line at the wall in the low-speed region. The detected high-speed region in t_0 and $t_0-\Delta t$ FOVs vector fields is expected to appear upstream of the FOV in Figure 6.16 (b) and Figure 6.16 (c).

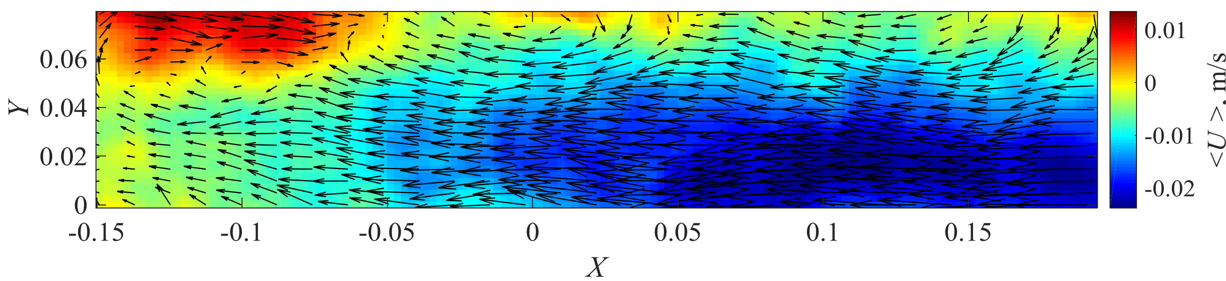

(a)

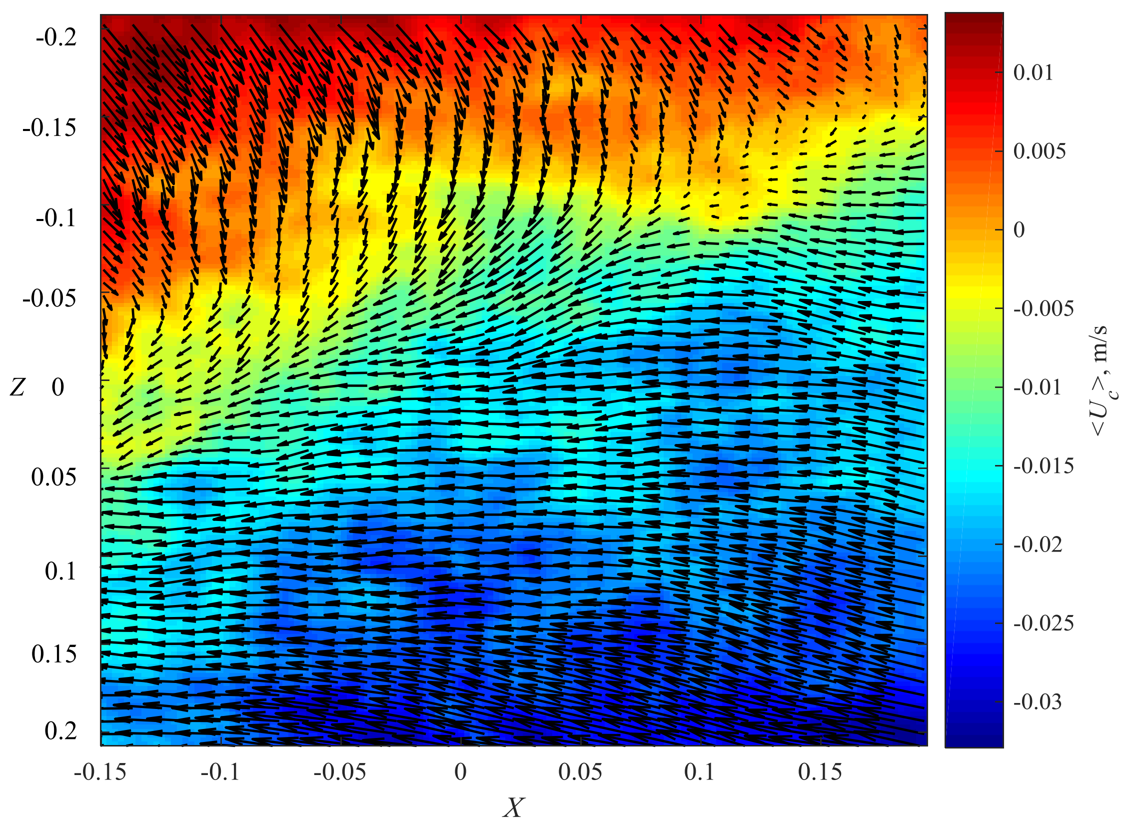

(b)

Figure 6.14 Conditional average of instantaneous velocity flow $\boldsymbol{U}_c$ field at $t_0-2\Delta t$ shown in (a) XY plane (Z=0) with background map of u_c and (b) XZ plane (Y=0.03H). Primary separation occurred at X=0.

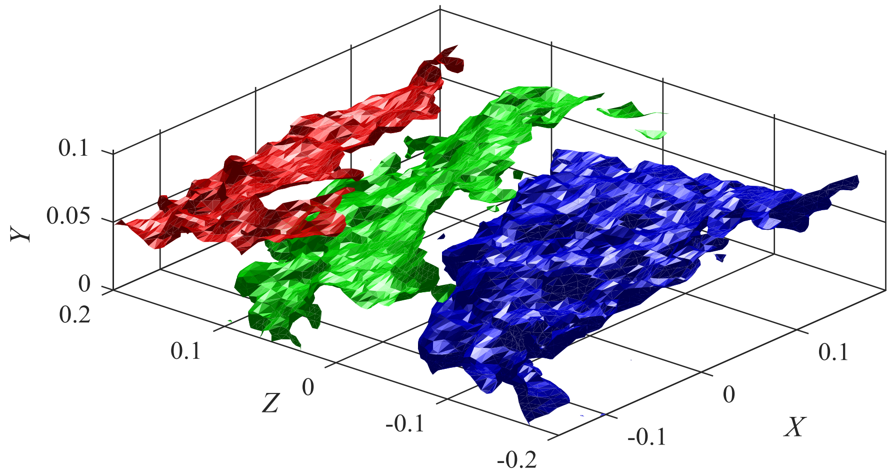

Figure 6.15 Conditional average of instantaneous velocity flow field $\boldsymbol{U}_c$ at $t_0-2\Delta t$ shown in three-dimensional contours of u_c. Red contour shows iso-surface of streamwise velocity of $\langle U_c \rangle = 0.02$ m/s, green contour shows $\langle U_c \rangle = 0$, and blue contour shows $\langle U_c \rangle = -0.02$ m/s.

Similar to the results of conditional averaging applied to planar flow fields, a region containing strong positive u fluctuations appears upstream of the detachment points and convects upstream for the flow fields captured at $t_0-\Delta t$ and $t_0-2\Delta t$. It can be argued that a high-speed region can initiate strong flow detachment or push the separation line downstream. This movement of the separation line is also represented by the first POD mode as it will be discussed, and it also shows that single-detachment vector fields. These single-detachment events are the most frequent feature of the entire vector fields as explained in section 4.2.2, and they contain the movement of the shear layer, which is also the most energetic motion in the flow.

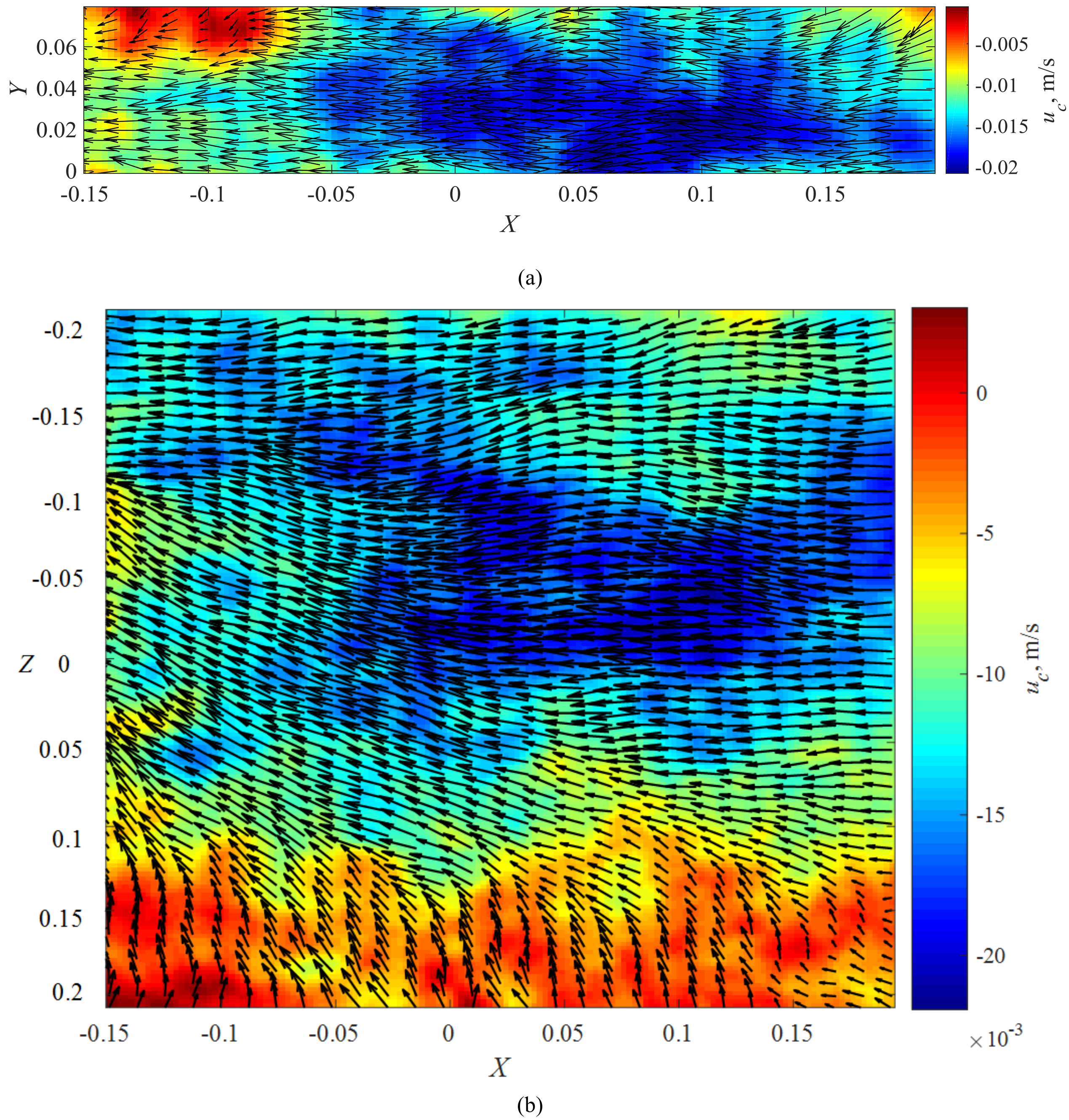

Figure 6.16 Conditional average of fluctuation velocity flow field $\boldsymbol{u}_{\mathrm{c}}$ at $t_0-2\Delta t$ shown in (a) *XY* plane (Z=0) with background map of u_{c} and (b) *XZ* plane (Y=0.03H). Primary separation occurred at X=0.

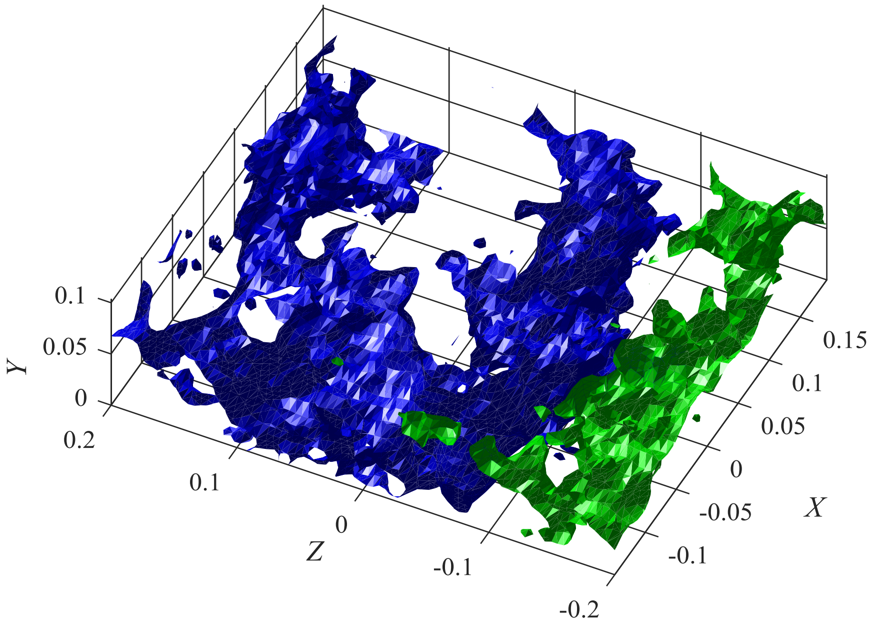

Figure 6.17 Conditional average of fluctuation velocity flow field $\boldsymbol{u}_{\mathrm{c}}$ at $t_0-2\Delta t$ shown in three-dimensional contours of u_{c}. Red contour shows iso-surface of u_c=0.01 m/s, green contour shows u_c=0, and blue contour shows $u_c = -0.01$ m/s.

6.3 POD results

To investigate the significant motions and structures in tomographic flow fields, POD technique has been used here. As explained in section 4.4, the matrix $U_{\boldsymbol{g}}$ is constructed using all the available flow fields (1,500). However the velocity matrices have been decimated by the factor of 2 in order to decreases calculation expenses as $U_{\boldsymbol{g}}$ contain massive three-dimensional flow matrices.

Figure 6.18 depicts the first POD mode. As explained for planar POD results, the first POD mode is expected to be a uniform flow field, which represents breathing motion of the flow. Figure 6.18 (b) shows that this uniform motion has also a significant component in spanwise direction, suggesting that the movement of the separation line happens in both X and Z directions.

Second POD mode is shown in Figure 6.21. Similar to the first mode, a uniform vector field has appeared. However, the vector field is not completely uniform, and it is distorted and mostly inclined toward Z direction upstream of the FOV ($X= - 0.2$) and it is inclined toward $-X$ direction at downstream of the FOV ($X= - 0.2$) as shown in Figure 6.21 (b). Modes 1 and 2 can suggest that most of the kinetic energy of the flow belongs to streamwise and spanwise uniform motions in the flow.

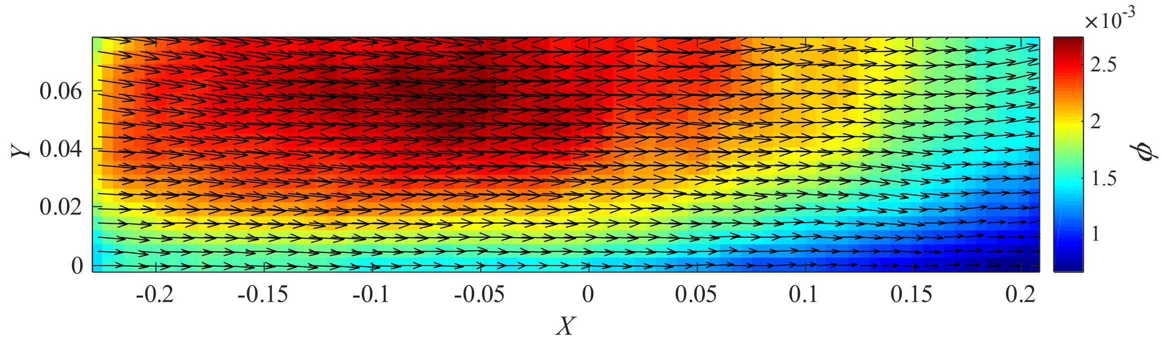

(a)

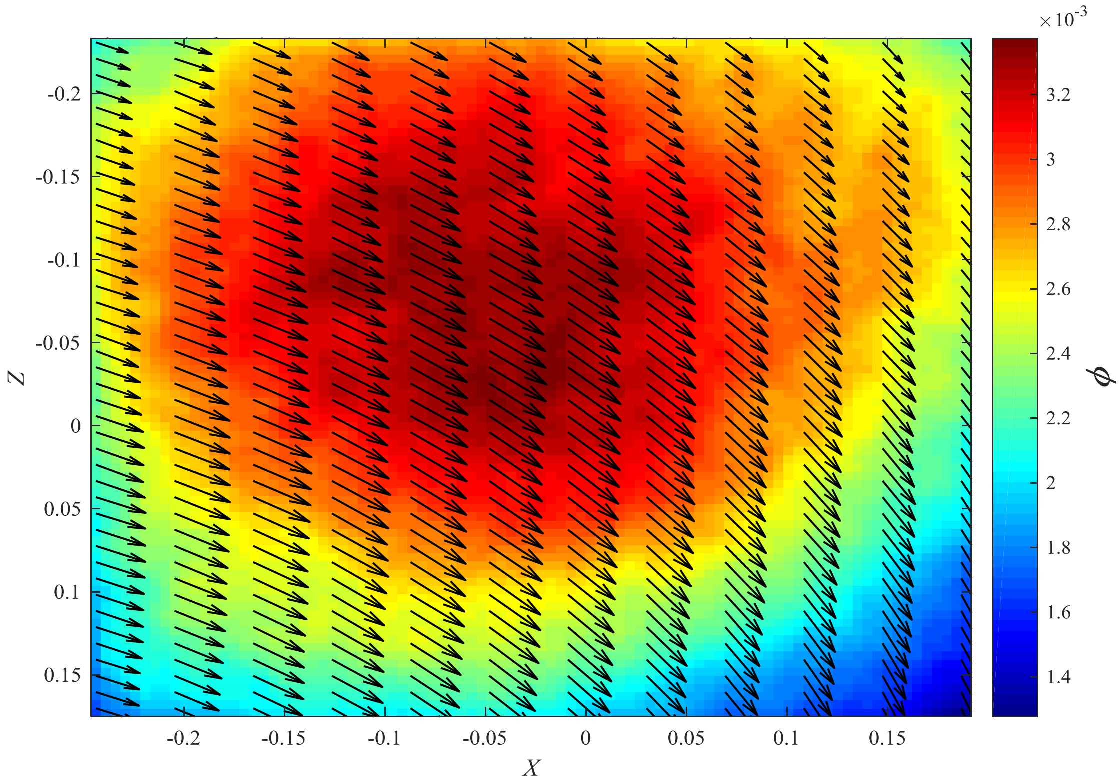

(b)

Figure 6.18 First POD mode (ϕ^1) shown in (a) *XY* plane at *Z*=0 and (b) *XZ* plane at *Y*=0.03*H*. A uniform vector field represents breathing motion. Background map shows the magnitude of vectors.

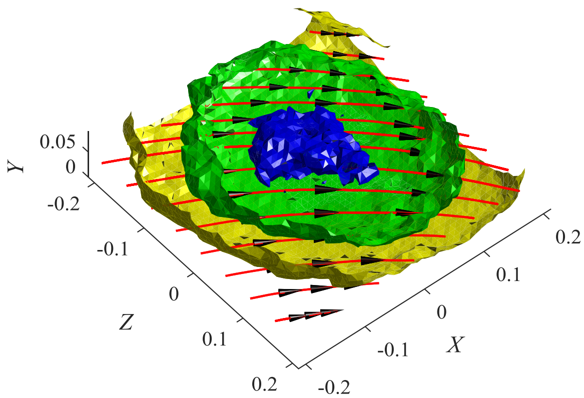

Figure 6.19 First POD mode (ϕ^1) shown in streamlines and contours of $|\boldsymbol{\phi}^1|=0.0035U_c$ (blue), $|\boldsymbol{\phi}^1|=0.003U_c$ (green) and $|\boldsymbol{\phi}^1|=0.0025U_c$ (yellow).

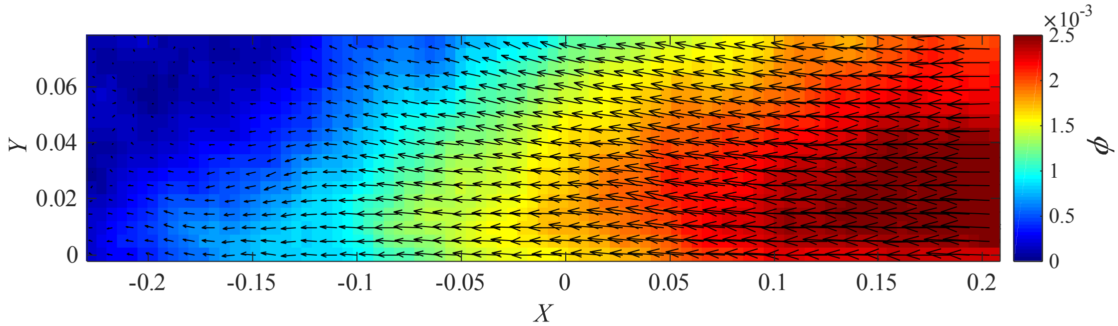

(a)

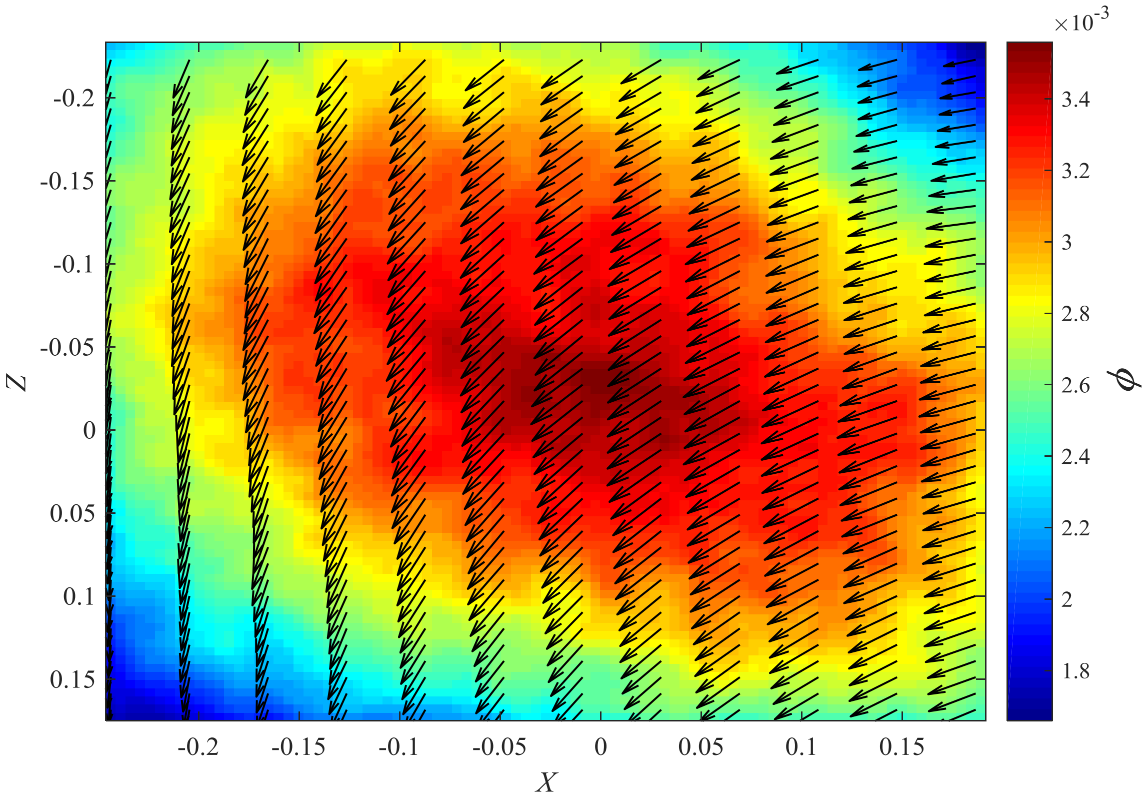

(b)

Figure 6.20 Second POD mode (ϕ^2) shown in (a) *XY* plane at *Z*=0 and (b) *XZ* plane at *Y*=0.03*H*. A uniform vector field represents breathing motion. Background map shows the magnitude of vectors.

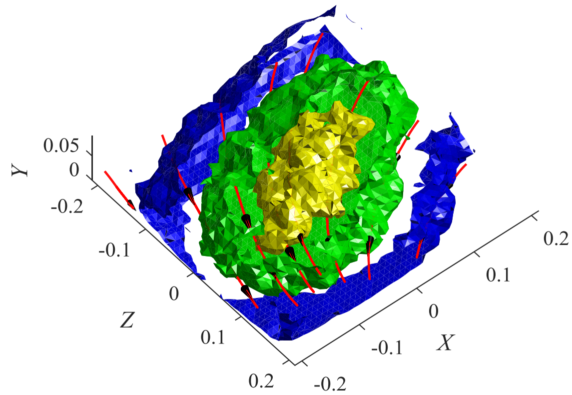

(c)

Figure 6.21 Second POD mode (ϕ^2) shown in three-dimensional streamlines and contours of $|\boldsymbol{\phi}^2|$=0.0033 U_c (blue), $|\boldsymbol{\phi}^2|$=0.003 U_c (green) and $|\boldsymbol{\phi}^2|$=0.0025 U_c (yellow). Background map shows the magnitude of vectors.

Third POD mode represents a focus point or a large vortex motion as shown in Figure 6.22. This shows that foci structures occur frequently in the vector fields. The center of the foci is located around $Z = -0.025$ and $X = -0.075$ and it moves slightly at different Z locations.

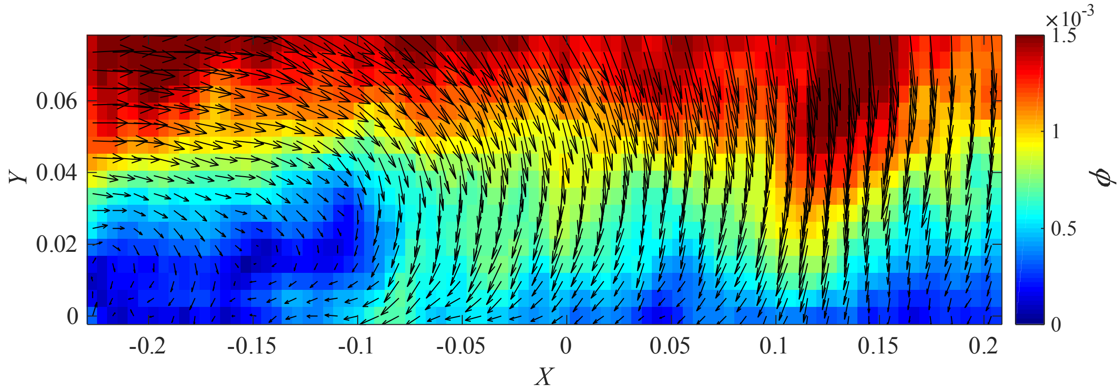

(a)

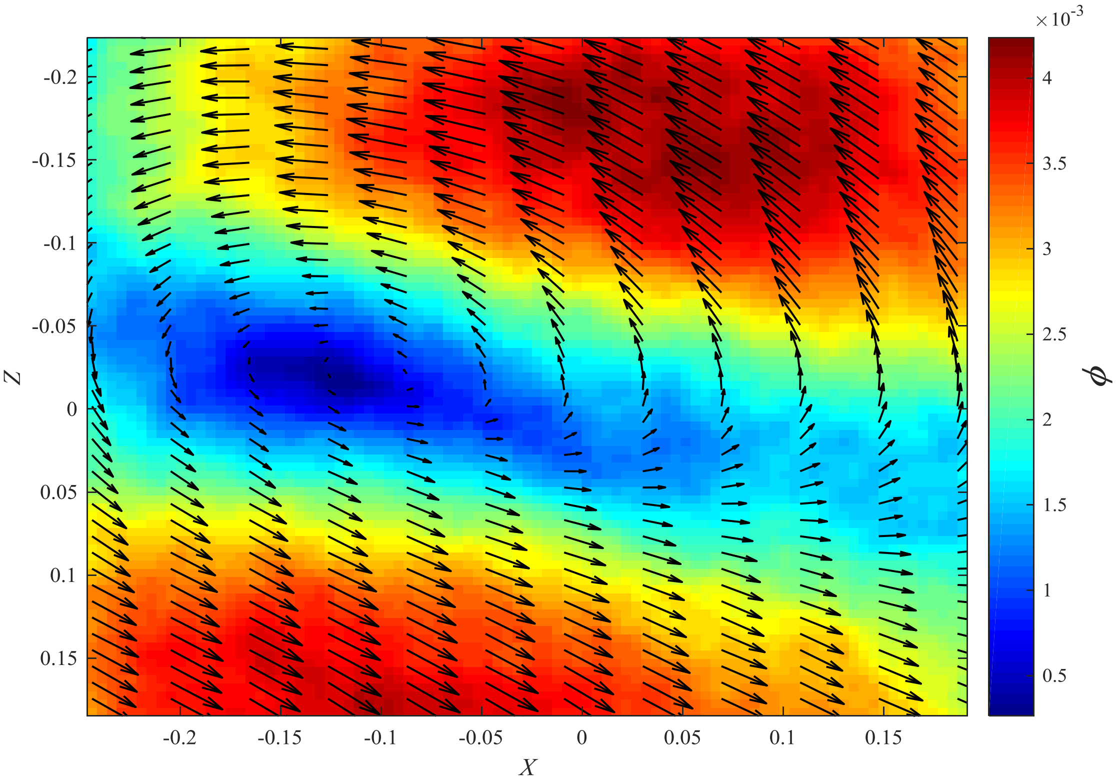

(b)

Figure 6.22 Third POD mode (ϕ^3) shown in (a) *xy* plane at *Z*=0 and (b) *xz* plane at *Y*=0.03. A large vortex with the axis of rotation directed towards *Y* has appeared. Background map shows the magnitude of vectors.

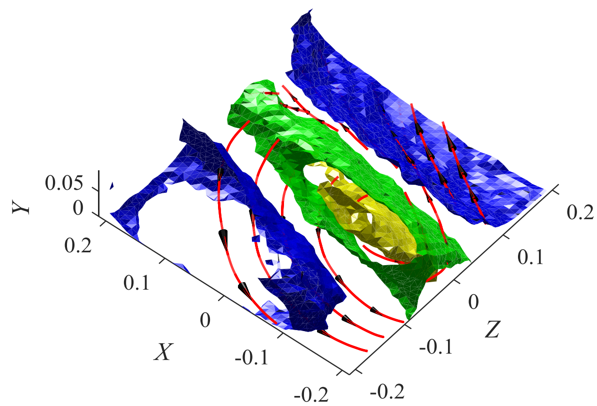

Figure 6.23 Third POD mode (ϕ^3) shown in three dimensional stream liens and contours of $|\boldsymbol{\phi}^3|$=0.003 U_c (blue), $|\boldsymbol{\phi}^3|$=0.0015 U_c (green) and $|\boldsymbol{\phi}^3|$=0.0008 U_c (yellow).

Figure 6.24 shows the fourth POD mode, which is similar to the second POD mode found for planar vector fields (shedding motion). As explained in chapter 5.4, the second POD mode of planar vector fields represents the strength of the shear layer and the vortex shedding phenomena. This mode shows that the shedding motion has occurred for different Z values at almost same streamwise locations as shown in Figure 6.24 (b).

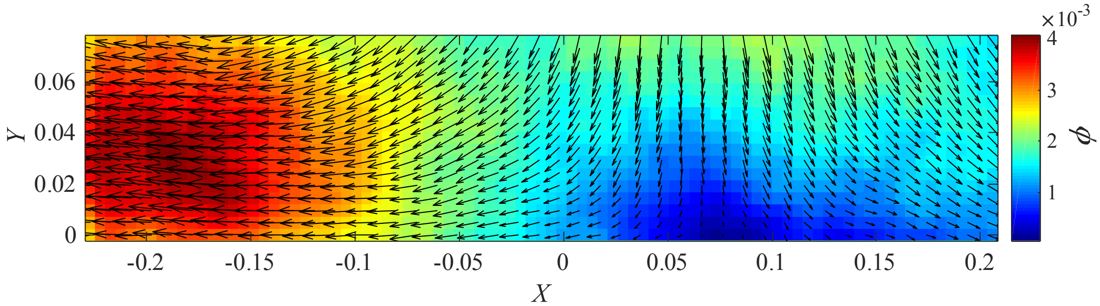

(a)

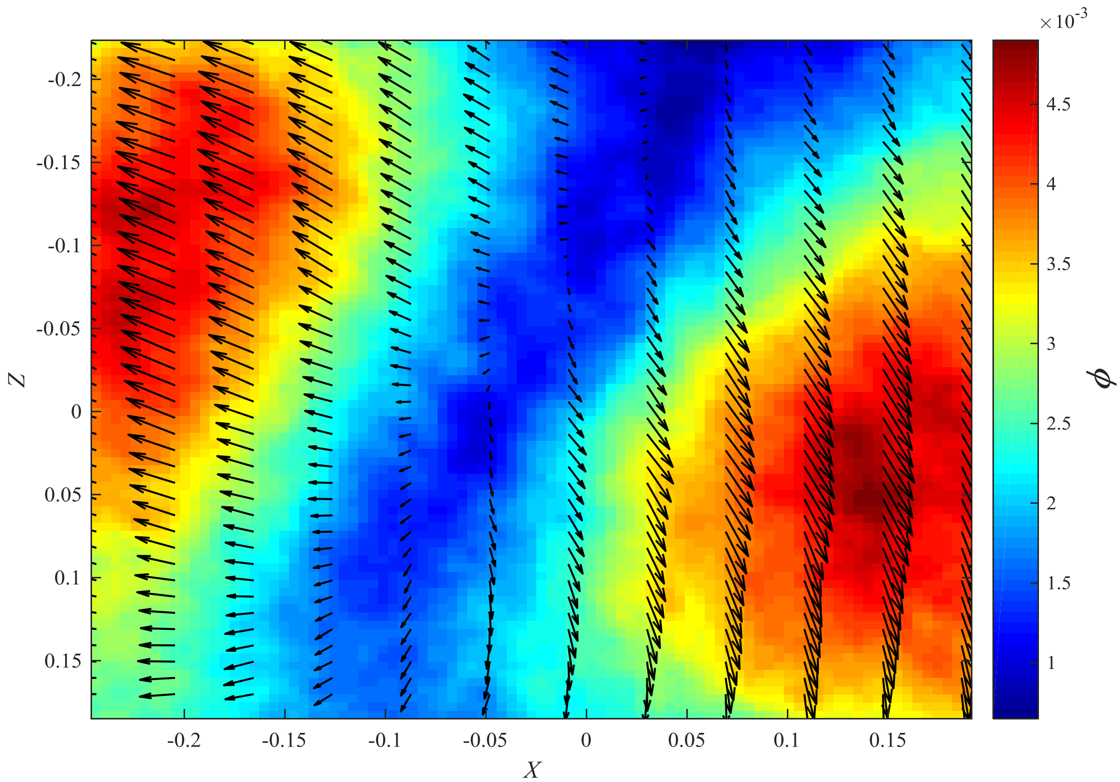

(b)

Figure 6.24 Fourth POD mode (ϕ^4) shown in (a) *XY* plane at *Z*=0 and (b) *XZ* plane at *Y*=0.03*H*. A three-dimensional shedding motion has appeared. Background maps shows the magnitude of vectors.

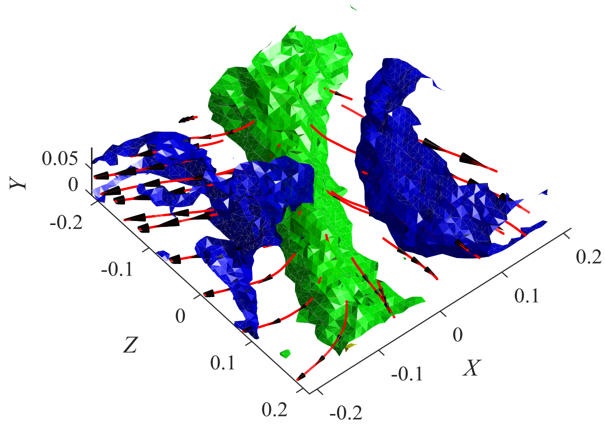

Figure 6.25 Fourth POD mode (ϕ^4) shown in three-dimensional streamlines and contours of $|\boldsymbol{\phi}^4|$=0.003 U_c (blue), $|\boldsymbol{\phi}^4|$=0.0015 U_c (green) and $|\boldsymbol{\phi}^4|$=0.0008 U_c (yellow).

Figure 6.26 shows the fifth POD mode. At positive *Z* values, the flow has similar structure as the shedding-motion mode (fourth mode). Figure 6.26 (a) also suggests a spanwise vortex located upstream of the FOV. However, for negative *Z* values, the vectors have strong inclination toward *Z* and –*Z* directions, which proposes a large vortex motion located at around Z=−0.14 and *X*=−0.05*H* as shown in Figure 6.26 (b).

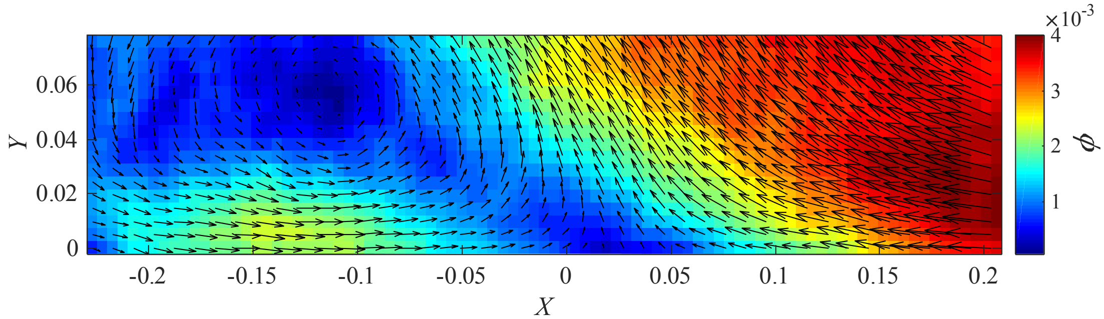

(a)

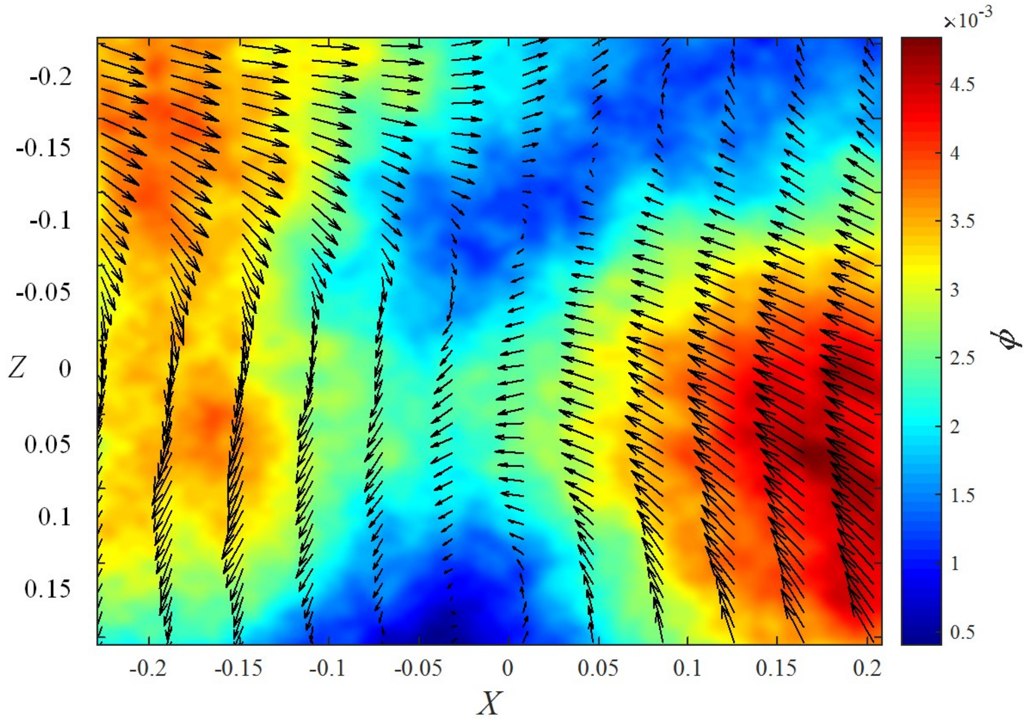

(b)

Figure 6.26 Fifth POD mode (ϕ^5) shown in (a) *XY* plane at *Z*=0 and (b) *XZ* plane at *Y*=0.03*H*. Background maps show the vector length.

A saddle point appears in the sixth POD mode as shown in Figure 6.27. This shows that saddle points are also frequent structures as reported in previous studies (Duquesne et al. 2015). The stagnation point of the saddle point appears at around *Z*=0 and *X*=0.025*H*.

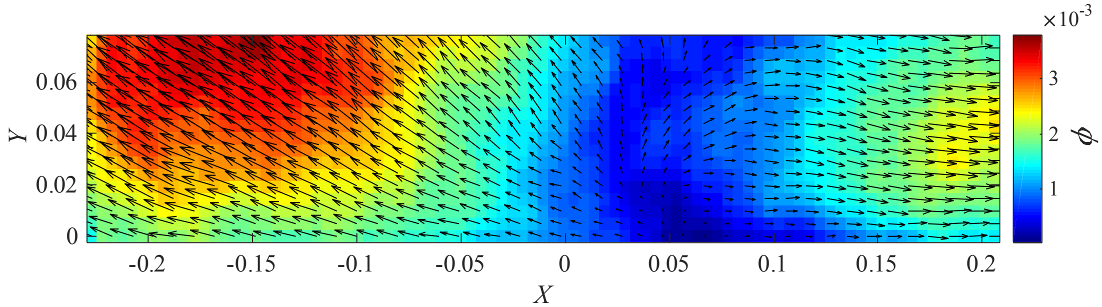

(a)

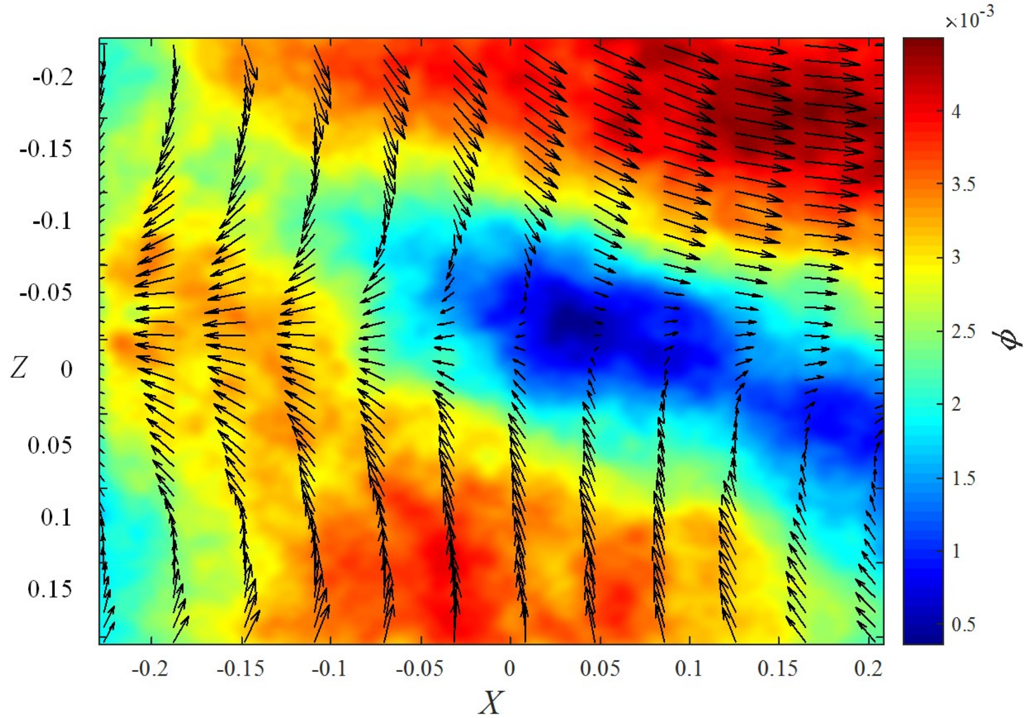

(b)

Figure 6.27 Sixth POD mode (ϕ^6) shown in (a) *XY* plane at *Z*=0 and (b) *xz* plane at *Y*=0.03*H*. A saddle point appears with stagnation located at around *Z*=0 and *X*=0.05*H*. Background map shows the vector length.

6.4 Reconstruction based on conditionally averaged POD coefficients

To better characterize the formation of the separation, a correlation between the variations of the strength of each POD mode and the occurrence of single-detachment flow instants is sought. For each single-detachment flow instant captured at the time, t_0, the vector fields captured at $t_0 \pm \Delta t$ are also selected. First, the POD coefficients (a_n) of the selected vector fields at different time instants are averaged. Different time instants are represented by T as defined by $t = t_0 + T \times \Delta t$. Therefore, different values of T, for instance T=2, show the vector fields captured at $t+2\Delta t$. The conditional averaging of a_1 to a_4 for positive and negative values of T is plotted in Figure 6.28.

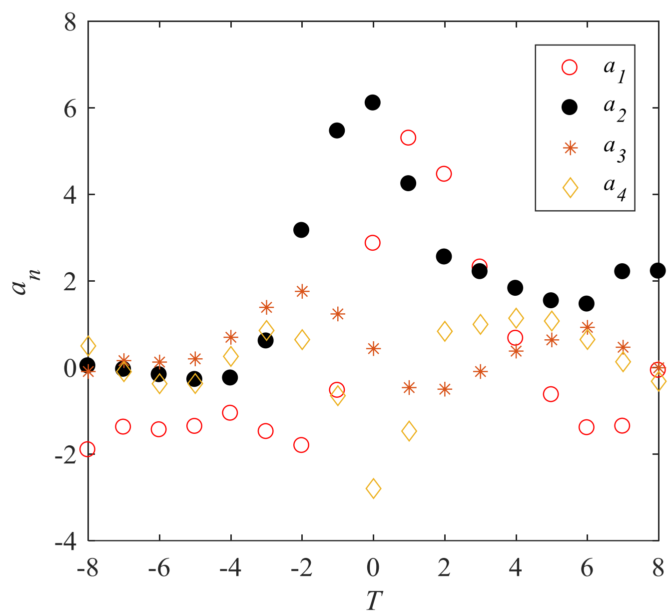

Figure 6.28 Conditional averaging over POD coefficients (a_n) before and after the instant of single-detachments.

It can be seen that for T<0, a_2 is greater than a_1, which means that the flow contains stronger backward motion, and for T>0, a_1 is greater than a_2, which means the flow contains stronger forward motion. This result is consistent with the results of conditional averaging over vector fields as the shear layer moves upstream for T<0 and a larger area of the FOV contains backward motion. The coefficient a_3 has two peaks before and after the instant of single detachment, which can indicate the semi-periodic nature of these modes and their phase differences. The minimum of a_4 at T=0 is also consistent to the conditional average vector field, because a_4 has similar pattern to a shear layer as shown in Figure 6.24, and strong shear layer and high velocity gradient occur at T=0 for single-detachments as shown in Figure 6.6. The negative sign of a_4 is due to the opposite direction that the mode 4 vector field has with respect to a shear layer as shown in Figure 6.24.

The mode coefficients (a_i) calculated in the previous conditional averaging as shown in Figure 6.28 are used to visualize the development of the flow structure at the instant of single-detachments. The flow field is reconstructed using the first four POD modes from $T = -3$ to $T = 2$ as shown in Figure 6.29. It can be seen that the center of the vortex is located around X=0.1H and Z=0.1H at $T=-3$, and it causes backward motion in the entire FOV as shown in Figure 6.29 (a). For $T = -2$, the orientation of the vortex has changed, and its axis is deflected towards X direction, as a result, an upward motion appear at the center of the FOV as shown in Figure 6.29 (b). This trend continues for $T = -1$, and the axis of the vortex is almost directed vertically, and it supplies strong upward motion at the center of FOV as shown in Figure 6.29 (c). At the instant of single-detachments, $T = 0$, a forward motion appears upstream around $X = -0.1H$ and Z=0.1H, and a backward motion appears downstream of the FOV around X=0.1H and $Z = -0.1H$ as shown in Figure 6.29 (d). This structure has similarity with an inclined shear layer, which is consistent with the strong magnitude of a_4 (shear-layer POD structure) at T=0 as shown in Figure 6.28. At T=1, forward motions becomes stronger and occupy almost the entire FOV, however, the streamlines are bended in a way that a vortex exists upstream at the left corner of the FOV as shown in Figure 6.29 (e). At T=2, the center of a vortex appears at the same corner, and the forward motions becomes stronger as shown in Figure 6.29 (f). These results are consistent with the previous conditional averaging on instantaneous flow fields as shown in Figure 6.28, in which a strong forward motion appears upstream of planar and tomographic FOVs and convects downstream and upstream for time instants of T>0 and T<0 respectively.

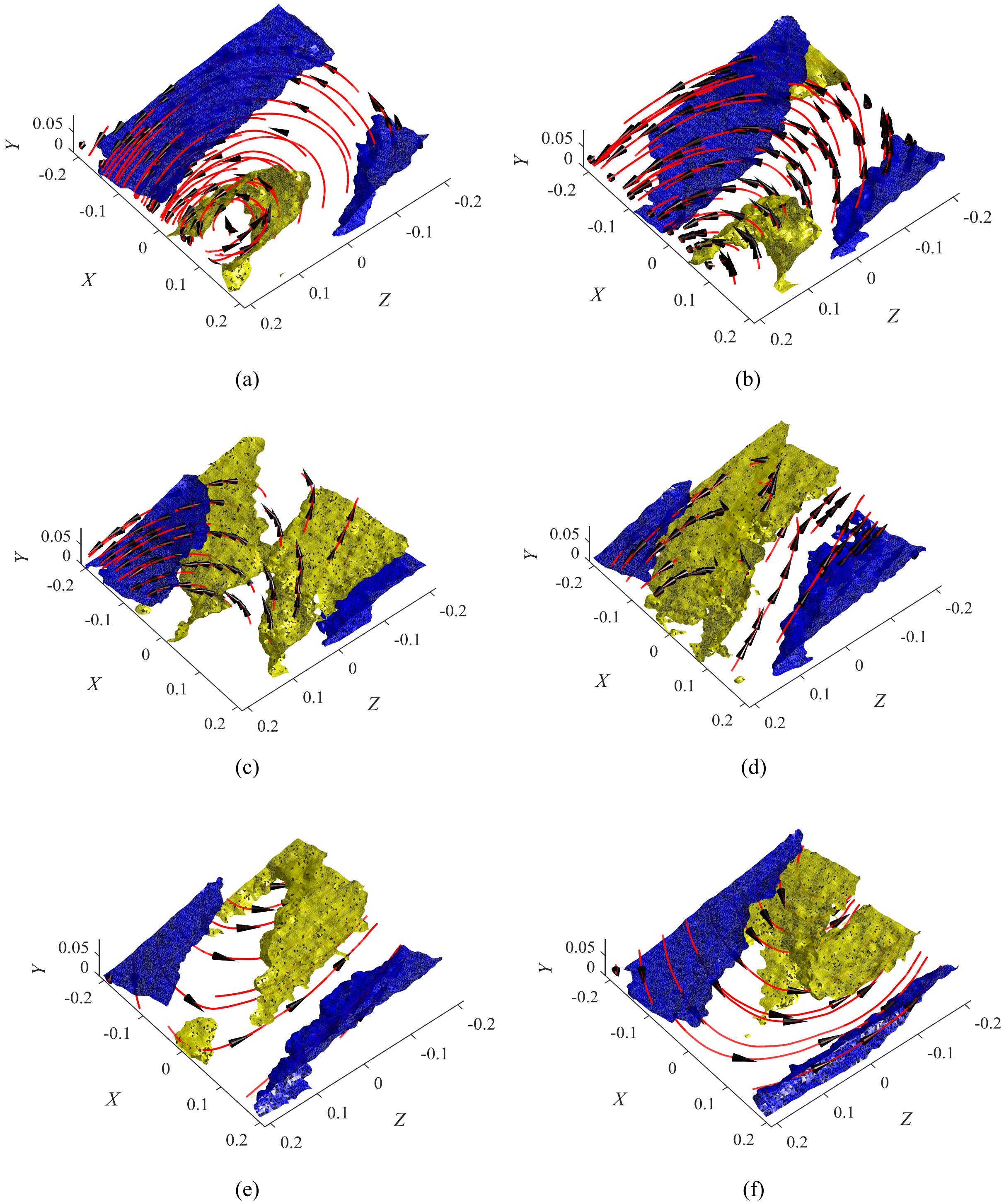

Figure 6.29. Reconstructed flow structures before and after the instants of single detachments (T=0) captured at (a) T=−3 with contours of $|\boldsymbol{U}|$=0.067U_c (blue) and 0.044U_c (yellow) (b) T=−2 with contours of $|\boldsymbol{U}|$=0.044U_c (blue) 0.0156U_c (yellow) (c) T=−1 with contours of $|\boldsymbol{U}|$=0.067U_c (blue) and 0.044U_c (yellow) (d) T=0 with contours of $|\boldsymbol{U}|$=0.067U_c (blue) and 0.044U_c (yellow) (e) T=1 with contours of $|\boldsymbol{U}|$=0.044U_c (blue) and 0.011U_c (yellow) (f) T=2 with contours of $|\boldsymbol{U}|$=0.044U_c (blue) and 0.0156U_c (yellow).

6.5 Conclusion

As a conclusion, Tomo-PIV measurement has provided a three-dimensional understanding of the separated flow. The mean flow shows a large vortex that appears at vicinity of the flow detachment. By performing conditional averaging over the single-detachment flow fields, similar high-speed structure observed in planar PIV measurements appears in tomographic FOV. This structure is being convected upstream for the flow fields captured ahead of the instant of single-detachments. The reconstructed flow fields by the first four POD modes provide an understanding of the development of the flow structure at the instant of single-detachments.

Chapter 7 Conclusion

Three-dimensional flow separation on a flat plate has been investigated using PIV techniques. Planar PIV measurements using four cameras provide a large FOV with high spatial dynamic range. The two-dimensional average flow field shows forward flow upstream of the FOV and flow detachment accompanying a recirculation region downstream of the FOV. The characteristics of the distributions of turbulent statistics and velocity profile have strong similarities with those reported for two-dimensional flow separation in the literature.

Planar instantons flow fields are categorized based on the number of the flow detachments and reattachments. The flow fields with single flow detachment are selected for conditional averaging, and their characteristics have been investigated. A high-speed region has been found upstream of flow detachment accompanying a low-speed region downstream of flow detachment point. This flow structure is found to be convected in time and it represents the movement of the shear layer. Similarly, the quadrant analysis suggests the high probability of strong positive u fluctuations appearing right upstream of the detachment point of the aforementioned flow fields.

The energetic flow motions are investigated by the POD analysis on planar flow fields. They include the breathing motion and the shear layer flow structure (shedding motion) and contain 22% and 11% of the total kinetic energy respectively. These two motions are also investigated in previous research studies and associated with low-frequency pressure fluctuations.

Tomo-PIV also provides three dimensional understanding of the flow in a smaller volume close at the detachment point. A large vortex has appeared in the mean flow field in the vicinity of the separation line. This large vortex with the rotation axis directed towards Y direction suggests that a critical point named a foci point has appeared in the flow. The vortex provides a strong backward flow at negative Z values and strong forward flow at positive Z values. However, instantaneous flow fields contain backward and forward motions distributed in the entire FOV.

Similar conditional averaging on tomographic velocity fields shows similar high-speed structure appearing upstream of flow detachments. This structure also contains strong *Z* component, and its movement in time is towards both *X* and *Z* directions.

The first two tomographic POD modes are semi-uniform flow fields directed towards *X* and *Z* directions. This result is consistent with the first planar POD mode. A foci structure has appeared in the third tomographic POD mode, which is similar to the mean flow field. This shows that this structure is not only the feature of the mean flow field but also a flow feature that contains significant kinetic energy among individual vector fields. The shear-layer structure has appeared in the fourth tomographic POD mode, and its *XY* cross section has similar pattern to the second planar POD mode. The two-dimensional shear layer appeared in the second planar POD mode has repeated for almost each *Z* plane of its corresponding three-dimensional mode. However, the stagnation point of the shear layer is moving in *X* direction for different planes.

Reconstruction of flow fields using the first four tomographic POD modes is conducted based on the POD coefficients of the flow instants occurred before and after the single-detachment (bin 1) flow fields. The reconstructed flow fields reveal the development of the flow structure before and after the instant of flow separation. It can be seen that the movement of the axis of the mean flow vortex upstream and downstream of the FOV contributes to the high-speed region appearing upstream of the detachment point. At the instant of single flow detachment, a strong shear-layer structure appears in the reconstructed flow field accompanying strong motion in *Y* direction. In addition, the axis of rotation for the vortex structure is strongly deflected toward *X* and *Z* directions before and after the instant of single-detachments.

Recommendations for future research:

According to the literature, there are connections between pressure fluctuations at the wall, the occurrence of POD modes and the energetic motions of the flow including movements of the separation line. A time-resolve Tomo-PIV measurement with high acquisition frequency according to the frequencies reported by Mohammed-Taifour et al. (2015) provides much more details of the frequency of the captured three-dimensional POD modes in addition to their contributions on the occurrence of flow detachment and pressure variations at the wall. Such a study can reveal more insights into the predicted cyclic nature of each mode and also the evolvement of each structure, in addition to the connections between these structures and variation of the wall pressure.

Future studies can improve control techniques by revealing the relation between pressure variation (and also the resulted drag forces) and the movement of the detachment line for instantons flow structures. Therefore, one of the goals can be postponing or delaying flow separation by slightly alternating the flow structure according to their instantaneous configuration.

References

Adrian, R.J., 1977. On the role of conditional averages in turbulence theory. *Turbulence in Liquids*, 1, pp.323-332.

Adrian, R.J., 2007. Hairpin vortex organization in wall turbulence a. *Physics of Fluids*, *19*(4), p.041301.

Adrian, R.J., Jones, B.G., Chung, M.K., Hassan, Y., Nithianandan, C.K. and Tung, A.C., 1989. Approximation of turbulent conditional averages by stochastic estimation. *Physics of Fluids* A: Fluid Dynamics, 1(6), pp.992-998.

Adrian, R.J., Meinhart, C.D. and Tomkins, C.D., 2000. Vortex organization in the outer region of the turbulent boundary layer. *Journal of Fluid Mechanics*, 422, pp.1-54.

Agarwal, N.K. and Simpson, R.L., 1990. Backflow structure of steady and unsteady separating turbulent boundary layer. *AIAA J*, *28*(10), pp.1764-1771.

Alving, A.E. and Fernholz, H.H., 1996. Turbulence measurements around a mild separation bubble and downstream of reattachment. *Journal of Fluid Mechanics*, *322*, pp.297-328.

Ashjaee, J. and Johnston, J.P., 1980. Straight-walled, two-dimensional diffusers-transitory stall and peak pressure recovery. *Journal of Fluids Engineering*, *102*(3), pp.275-282.

Atkinson, C., Coudert, S., Foucaut, J.M., Stanislas, M. and Soria, J., 2011. The accuracy of tomographic particle image velocimetry for measurements of a turbulent boundary layer. *Experiments in fluids*, 50(4), pp.1031-1056.

Baskaran, V., Smits, A.J. and Joubert, P.N., 1987. A turbulent flow over a curved hill Part 1. Growth of an internal boundary layer. *Journal of Fluid Mechanics*, *182*, pp.47-83.

Berkooz, G., Holmes, P. and Lumley, J.L., 1993. The proper orthogonal decomposition in the analysis of turbulent flows. *Annual Review of Fluid Mechanics*, 25(1), pp.539-575.

Blackwelder, R.F. and Kaplan, R.E., 1976. On the wall structure of the turbulent boundary layer. *Journal of Fluid Mechanics*, 76(01), pp.89-112.

Castillo, L. and George, W.K., 2001. Similarity analysis for turbulent boundary layer with pressure gradient: outer flow. *AIAA Journal*, 39(1), pp.41-47.

Cherry, E.M., Elkins, C.J. and Eaton, J.K., 2008. Geometric sensitivity of three-dimensional separated flows. *International Journal of Heat and Fluid Flow*, *29*(3), pp.803-811.

Cherry, N.J., Hillier, R. and Latour, M.E.M., 1984. Unsteady measurements in a separated and reattaching flow. *Journal of Fluid Mechanics*, 144(1), p.13.

Clauser, F.H., 1956. The turbulent boundary layer. *Advances in Applied Mechanics*, *4*, pp.1-51.

Corino, E.R. and Brodkey, R.S., 1969. A visual investigation of the wall region in turbulent flow. *Journal of Fluid Mechanics*, *37*(1), pp.1-30.

Cuvier, C., Foucaut, J.M., Braud, C. and Stanislas, M., 2014. Characterisation of a high Reynolds number boundary layer subject to pressure gradient and separation. *Journal of Turbulence*, *15*(8), pp.473-515.

De Silva, C.M., Baidya, R., Khashehchi, M. and Marusic, I., 2012. Assessment of tomographic PIV in wall-bounded turbulence using direct numerical simulation data. *Experiments in Fluids*, *52*(2), pp.425-440.

Délery, J., 2013. *Three-dimensional separated flows topology: singular points, beam splitters and vortex structures*. John Wiley & Sons, p.4.

Délery, J.M., 2001. Robert Legendre and Henri Werlé: Toward the elucidation of three-dimensional separation. *Annual Review of Fluid Mechanics*, *33*(1), pp.129-154.

Dengel, P. and Fernholz, H.H., 1990. An experimental investigation of an incompressible turbulent boundary layer in the vicinity of separation. *Journal of Fluid Mechanics*, *212*, pp.615-636.

Dianat, M. and Castro, I.P., 1991. Turbulence in a separated boundary layer. *Journal of Fluid Mechanics*, *226*, pp.91-123.

Duquesne, P., Maciel, Y. and Deschênes, C., 2015. Unsteady flow separation in a turbine diffuser. *Experiments in Fluids*, 56(8), p.156.

Elsinga, G.E., Scarano, F., Wieneke, B. and van Oudheusden, B.W., 2006. Tomographic particle image velocimetry. *Experiments in Fluids*, 41(6), pp.933-947.

Fairlie. B. D. (1973). A study of separation in turbulent boundary layers. P1i.D. Thesis. Univ. of Melbourne, Melbourne.

Gad-el-Hak, M., 2000.: Flow control: passive, active, and reactive flow management. *Oxford: University Press*, p.150.

Hain, R., Scharnowski, S., Reuther, N., Kähler, C.J., Schröder, A., Geisler, R., Agocs, J., Röse, A., Novara, M., Stanislas, M. and Cuvier, C., 2016. Coherent large scale structures in adverse pressure gradient turbulent boundary layers. 18th International Symposium on the Application of Laser and Imaging Techniques to Fluid Mechanics, *Lisbon*, *Portugal*, JULY 4 – 7, 2016.

Herman, G.T. and Lent, A., 1976. Iterative reconstruction algorithms. *Computers in biology and medicine*, *6*(4), pp.273-294.

Holmes, J.L., 1998. Lumley, and G. Berkooz. Turbulence, Coherent Structures. *Dynamical Systems and Symmetry. Cambridge University Press, Cambridge*.

Kähler, C.J., 2004. The significance of coherent flow structures for the turbulent mixing in wall-bounded flows (Doctoral dissertation, DLR, Dt. Zentrum für Luft-und Raumfahrt).

Kim, H., Westerweel, J. and Elsinga, G.E., 2012. Comparison of Tomo-PIV and 3D-PTV for microfluidic flows. *Measurement Science and Technology*, *24*(2), p.024007.

Kitsios, V., Atkinson, C., Sillero, J.A., Borrell, G., Gungor, A.G., Jiménez, J. and Soria, J., 2015. Boundary condition development for an adverse pressure gradient turbulent boundary layer at the verge of separation. *Advances in Computation, Modeling and Control of Transitional and Turbulent Flows*, p.269.

Kiya, M. and Sasaki, K., 1983. Structure of a turbulent separation bubble. *Journal of Fluid Mechanics*, *137*, pp.83-113.

Kline, S.J., Reynolds, W.C., Schraub, F.A. and Runstadler, P.W., 1967. The structure of turbulent boundary layers. *Journal of Fluid Mechanics, 30*(4), pp.741-773.

Krogstad, P.A. and Kaspersen, J.H., 2002. Structure inclination angle in a turbulent adverse pressure gradient boundary layer. *Journal of Fluids Engineering*, *124*(4), pp.1025-1033.

Krogstad, P.Å. and Skåre, P.E., 1995. Influence of a strong adverse pressure gradient on the turbulent structure in a boundary layer. *Physics of Fluids*, *7*(8), pp.2014-2024.

Le, H., Moin, P. and Kim, J., 1997. Direct numerical simulation of turbulent flow over a backward-facing step. *Journal of Fluid Mechanics*, *330*, pp.349-374.

Lee, J.H. and Sung, H.J., 2008. Effects of an adverse pressure gradient on a turbulent boundary layer. *International Journal of Heat and Fluid Flow*, *29*(3), pp.568-578.

Lee, J.H. and Sung, H.J., 2009. Structures in turbulent boundary layers subjected to adverse pressure gradients. *Journal of Fluid Mechanics*, *639*, pp.101-131.

Lumley, J. L. 1967. The structure of inhomogeneous turbulence. In *Atmospheric Turbulence and Wave Propagation*, ed. A. M. Yaglom, V. I. Tatarski, pp. 166-78. Moscow: Nauka

Malm, J., Schlatter, P. and Henningson, D.S., 2012. Coherent structures and dominant frequencies in a turbulent three-dimensional diffuser. *Journal of Fluid Mechanics*, *699*, pp.320-351.

Marquillie, M., Laval, J.P. and Dolganov, R., 2008. Direct numerical simulation of a separated channel flow with a smooth profile. *Journal of Turbulence*, (9), p.N1.

Menter, F.R., 1996. A comparison of some recent eddy-viscosity turbulence models. *Journal of Fluids Engineering*, *118*(3), pp.514-519.

Menter, F.R., 1996. A comparison of some recent eddy-viscosity turbulence models. *Journal of Fluids Engineering*, *118*(3), pp.514-519.

Mohammed-Taifour, A. and Weiss, J., 2016. Unsteadiness in a large turbulent separation bubble. *Journal of Fluid Mechanics*, *799*, pp.383-412.

Na, Y. and Moin, P., 1998. Direct numerical simulation of a separated turbulent boundary layer. *Journal of Fluid Mechanics*, *370*, pp.175-201.

Novara, M. and Scarano, F., 2013. A particle-tracking approach for accurate material derivative measurements with tomographic PIV. *Experiments in Fluids*, *54*(8), p.1584.

Ohlsson, J., Schlatter, P., Fischer, P.F. and Henningson, D.S., 2010. Direct numerical simulation of separated flow in a three-dimensional diffuser. *Journal of Fluid Mechanics*, *650*, pp.307-318.

Perry, A.E. and Fairlie, B.D., 1975. Critical points in flow patterns. *Advances in Geophysics*, *18*, pp.299-315.

Perry, A.E. and Schofield, W.H., 1973. Mean velocity and shear stress distributions in turbulent boundary layers. *The Physics of Fluids*, *16*(12), pp.2068-2074.

Prandtl, L. 1904. Über flüssigkeitsbewegung bei sehr kleiner reibung. *In Third International Math Congress*, Heidelberg, pages 484 491.Quarterly Applied Mathematics. 45 (3), 561–571.

Prasad, A.K., 2000. Particle image velocimetry. *CURRENT SCIENCE-BANGALORE-*, *79*(1), pp.51-60.

Raffel, M., Willert, C.E. and Kompenhans, J., 2007. *Particle image velocimetry: a practical guide*. Springer Science & Business Media.

Raffel, M., Willert, C.E., Wereley, S. and Kompenhans, J., 2013. *Particle image velocimetry: a practical guide*. Springer.

Robinson, S.K., 1991. Coherent motions in the turbulent boundary layer. *Annual Review of Fluid Mechanics*, *23*(1), pp.601-639.

Scarano, F. and Poelma, C., 2009. Three-dimensional vorticity patterns of cylinder wakes. *Experiments in Fluids*, *47*(1), p.69.

Scarano, F., 2012. Tomographic PIV: principles and practice. *Measurement Science and Technology*, 24(1), p.012001.

Schlichting, H., 1979. *Boundary-Layer Theory*, 7th ed McGraw-Hill. New York, p.638.

Sigurdson, L.W., 1995. The structure and control of a turbulent reattaching flow. *Journal of Fluid Mechanics*, *298*, pp.139-165.

Simpson, R.L., 1983. A model for the backflow mean velocity profile. *AIAA Journal*, *21*(1), pp.142-143.

Simpson, R.L., 1987. Two-dimensional turbulent separated flow. *AIAA Journal* 25(6), pp.775-776.

Simpson, R.L., 1989. Turbulent boundary-layer separation. *Annual Review of Fluid Mechanics, 21*(1), pp.205-232.

Simpson, R.L., 1996. Aspects of turbulent boundary-layer separation. *Progress in Aerospace Sciences*, *32*(5), pp.457-521.

Simpson, R.L., Chew, Y.T. and Shivaprasad, B.G., 1981. The structure of a separating turbulent boundary layer. Part 1. Mean flow and Reynolds stresses. *Journal of Fluid Mechanics*, *113*, pp.23-51.

Simpson, R.L., Strickland, J.H. and Barr, P.W., 1977. Features of a separating turbulent boundary layer in the vicinity of separation. *Journal of Fluid Mechanics*, *79*(3), pp.553-594.

Sirovich, L., 1987. Turbulence and the dynamics of coherent structures. I. Coherent structures. *Quarterly of Applied Mathematics*, *45*(3), pp.561-571.

Skåre, P.E. and Krogstad, P.Å., 1994. A turbulent equilibrium boundary layer near separation. *Journal of Fluid Mechanics*, *272*, pp.319-348.

Skote, M. and Henningson, D.S., 2002. Direct numerical simulation of a separated turbulent boundary layer. *Journal of Fluid Mechanics*, *471*, pp.107-136.

Song, S. and Eaton, J., 2002. The effects of wall roughness on the separated flow over a smoothly contoured ramp. *Experimental Fluids*, 33(1), pp.38-46.

Song, S., DeGraaff, D.B. and Eaton, J.K., 2000. Experimental study of a separating, reattaching, and redeveloping flow over a smoothly contoured ramp. *International Journal of Heat and Fluid Flow*, *21*(5), pp.512-519.

Song, S., DeGraaff, D.B. and Eaton, J.K., 2000. Experimental study of a separating, reattaching, and redeveloping flow over a smoothly contoured ramp. *International Journal of Heat and Fluid Flow*, *21*(5), pp.512-519.

Surana, A., Grunberg, O. and Haller, G., 2006. Exact theory of three-dimensional flow separation. Part 1. Steady separation. *Journal of Fluid Mechanics*, *564*, pp.57-103.

Thompson, B.E. and Whitelaw, J.H., 1985. Characteristics of a trailing-edge flow with turbulent boundary-layer separation. *Journal of Fluid Mechanics*, 157, pp.305-326.

Tobak, M. and Peake, D.J., 1982. Topology of three-dimensional separated flows. *Annual review of Fluid Mechanics*, *14*(1), pp.61-85.

Townsend, A.A., 1980. *The Structure of Turbulent Shear Flow*. Cambridge university press.

Troutt, T.R., Scheelke, B. and Norman, T.R., 1984. Organized structures in a reattaching separated flow field. *Journal of Fluid Mechanics*, *143*, pp.413-427.

Tulapurkara, E.G., Khoshnevis, A.B. and Narasimhan, J.L., 2001. Wake-boundary layer interaction subject to convex and concave curvatures and adverse pressure gradient. *Experiments in Fluids*, *31*(6), pp.697-707.

Wallace, J.M., 2016. Quadrant analysis in turbulence research: history and evolution. *Annual Review of Fluid Mechanics*, *48*, pp.131-158.

Wallace, J.M., Eckelmann, H. and Brodkey, R.S., 1972. The wall region in turbulent shear flow. *Journal of Fluid Mechanics*, *54*(1), pp.39-48.

Wasistho, B. and Squires, K.D., 2005. Prediction of turbulent separation over a backward-facing smooth ramp. *Journal of Turbulence*, (6), p.N1.

Webster, D.R., DeGraaff, D.B. and Eaton, J.K., 1996. Turbulence characteristics of a boundary layer over a two-dimensional bump. *Journal of Fluid Mechanics*, *320*, pp.53-69.

Werle, H., 1973. Hydrodynamic flow visualization *Annual Review of Fluid Mechanics, 5*(1), pp.361-386.

Westerweel, J. and Scarano, F., 2005. Universal outlier detection for PIV data. *Experiments in Fluids*, *39*(6), pp.1096-1100.

Westerweel, J., Dabiri, D. and Gharib, M., 1997. The effect of a discrete window offset on the accuracy of cross-correlation analysis of digital PIV recordings. *Experiments in Fluids*, *23*(1), pp.20-28.

Wieneke, B., 2008. Volume self-calibration for 3D particle image velocimetry. *Experiments in Fluids*, *45*(4), pp.549-556.

Zagarola, M.V., Perry, A.E. and Smits, A.J., 1997. Log laws or power laws: The scaling in the overlap region. *Physics of Fluids*, *9*(7), pp.2094-2100.

Appendix A

The NCC maps for two pairs of windows, which are selected in the overlap regions of fields 2 and 3, and the overlap regions of fields 3 and 4 are shown in Figure Ap. 1 (a) and (b), and Figure Ap. 2 (a) and (b) respectively. The orientations of NCC maps have become more symmetric and their peaks have moved closer to the center of the maps after applying the corrections as shown in Figure Ap. 1 (c) and (d), and Figure Ap. 2 (c) and (d) respectively.

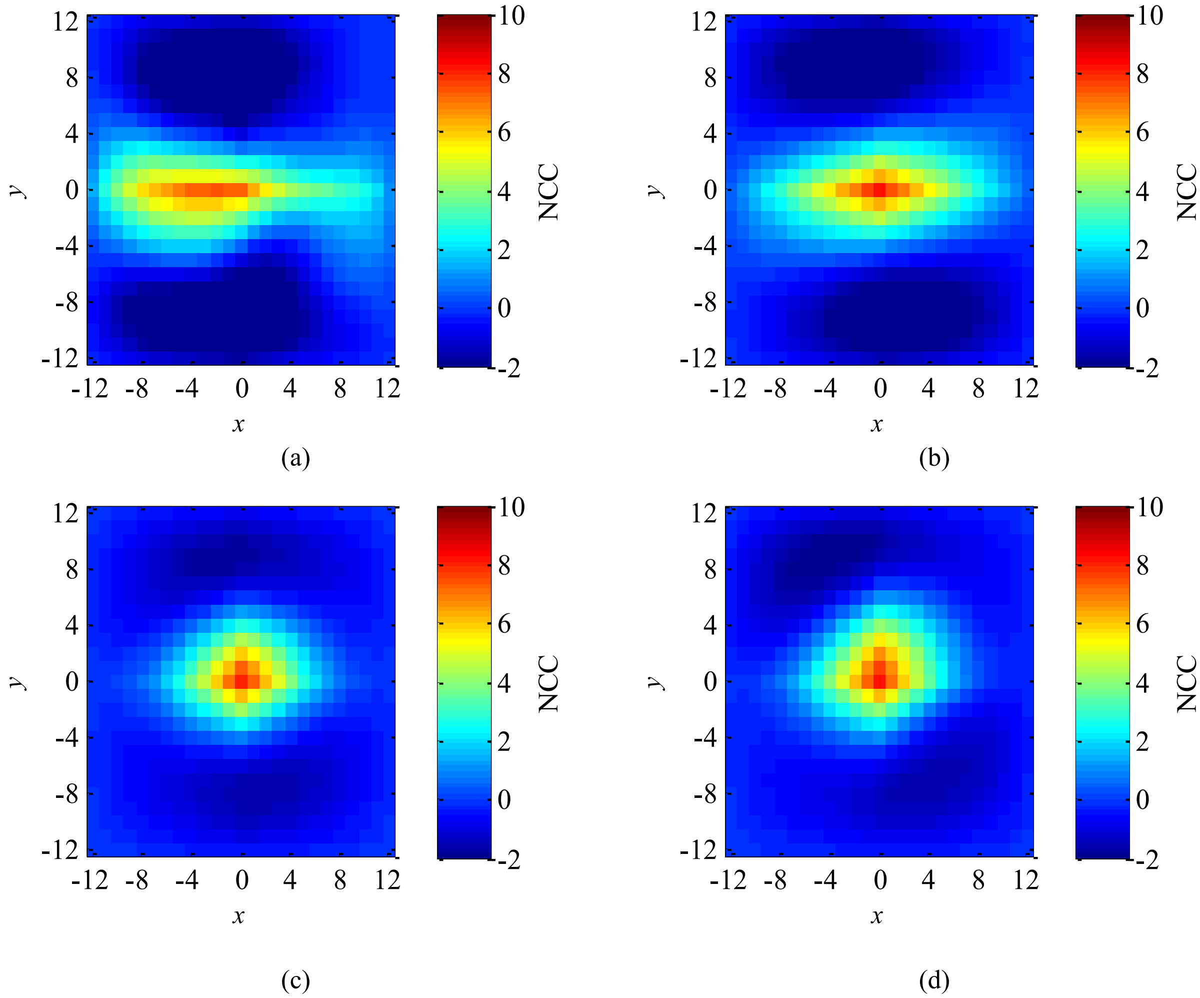

Figure Ap. 1 Average NCC maps for (a) window 1 (b) window 2 before applying corrections for camera fields 3 and 4; and corresponding windows after applying corrections (c) and (d).

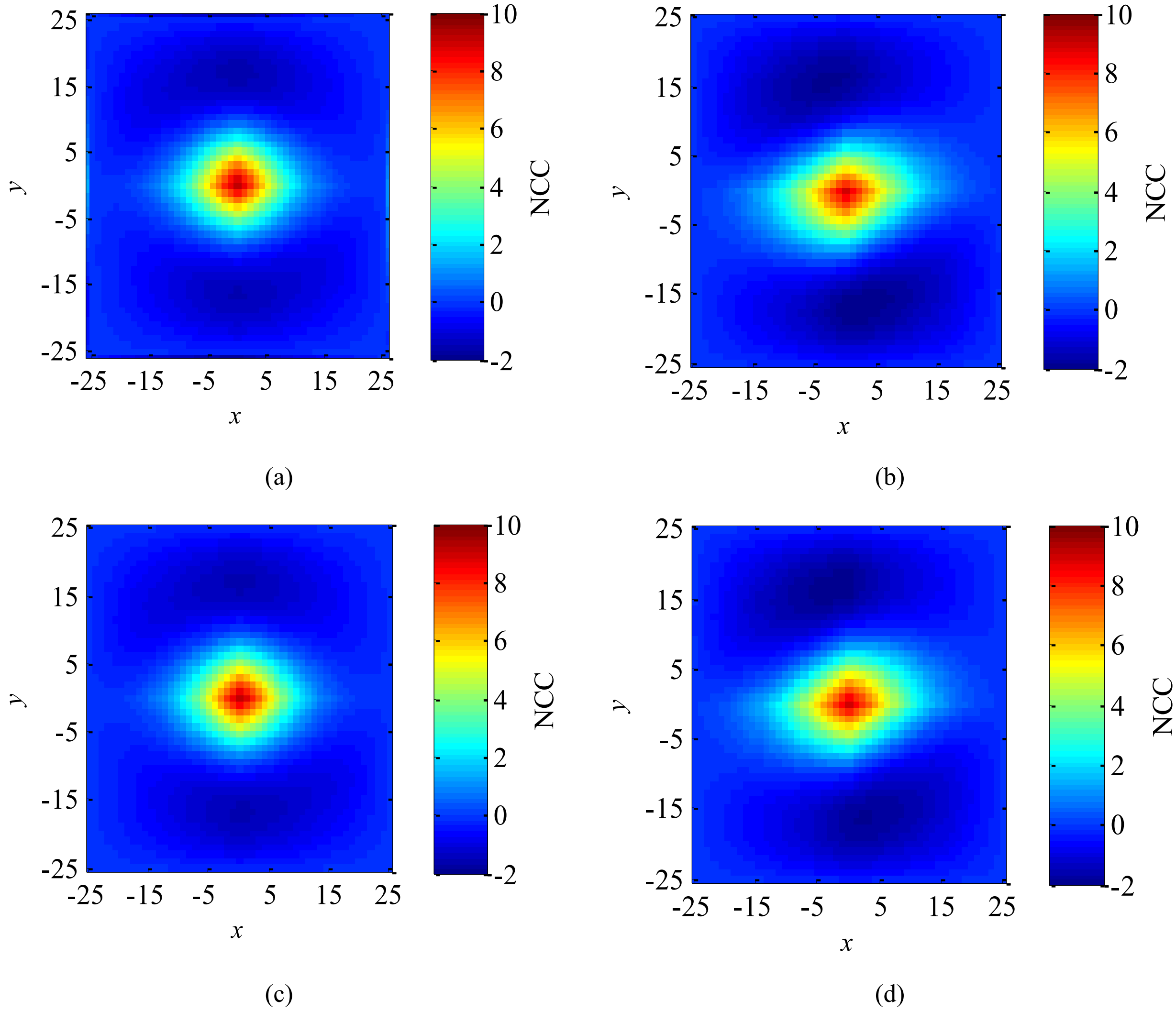

Figure Ap. 2 Average NCC maps for (a) *window 1* (b) *window 2* before applying corrections for camera fields 2 and 3; and corresponding windows after applying corrections (c) and (d).

The locations of the monitoring points for calculating $<\Delta V_d>$ at the overlap regions of fields 2 and 3 and fields 4 and 5 are provided in Table Ap. 1 and Table Ap. 2.

Table Ap. 1 Locations of the monitored points selected in field 2&3 overlap region with respect to the separation point.

	Point 6	Point 7	Point 8	Point 9	Point 10
x (mm)	−44.34	−44.34	−44.34	−44.34	−44.34
y (mm)	2.47	14.3	26.0	37.83	49.6
$<\Delta V_d>$ (m/s)	−0.0011	−0.0014	−0.0014	7.4×10^{-4}	−0.0022
$<\Delta V_d>/<U>$ (%)	6.0	3.0	1.6	0.70	1.5
Standard deviation of ΔV_d	0.0132	0.0131	0.0159	0.0159	0.0140

Table Ap. 2 Locations of the monitored points selected in the overlap region of field 3 and 4 with respect to the separation point.

	Point 11	Point 12	Point 13	Point 14	Point 15
x (mm)	−107.3	−107.3	−107.3	−107.3	−107.3
y (mm)	2.47	14.3	26.0	37.83	49.6
$<\Delta V_d>$ (m/s)	0.0024	0.0056	0.0054	0.0029	5.68×10^{-5}
$<\Delta V_d>/<U>$ (%)	6.3	8.1	3.8	1.3	0.02
Standard deviation of ΔV_d	0.0197	0.0236	0.0194	0.0162	0.0113

ΔV_d versus the velocity field number (N) at the 15 mentioned locations in the overlap regions of four cameras are plotted for 500 flow fields in Figure Ap. 3, Figure Ap. 4, Figure Ap. 5, Figure Ap. 6, Figure Ap. 7 and Figure Ap. 8.

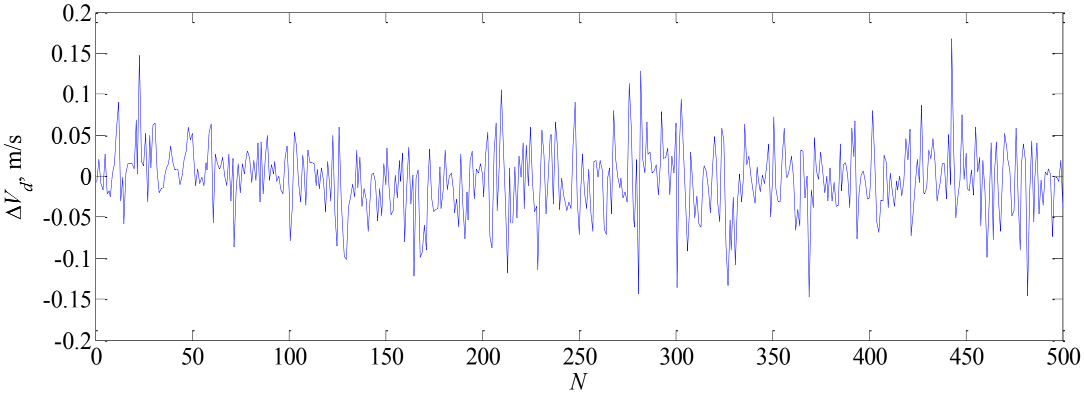

(a)

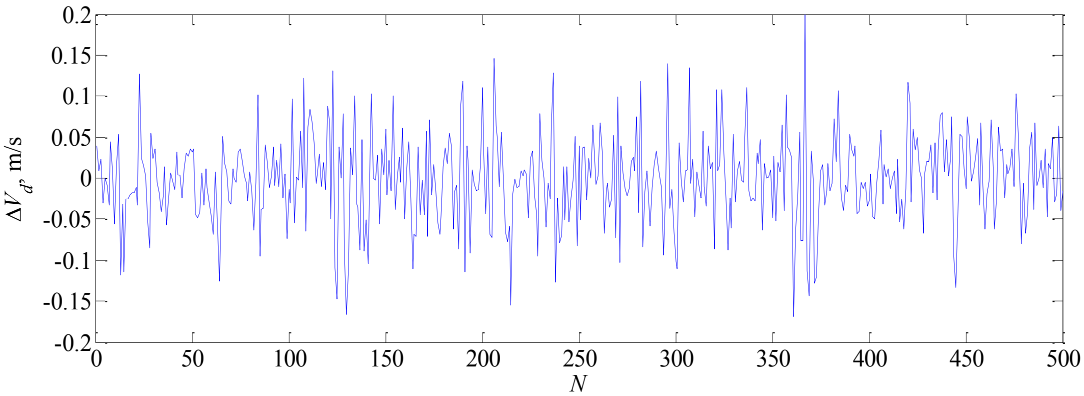

(b)

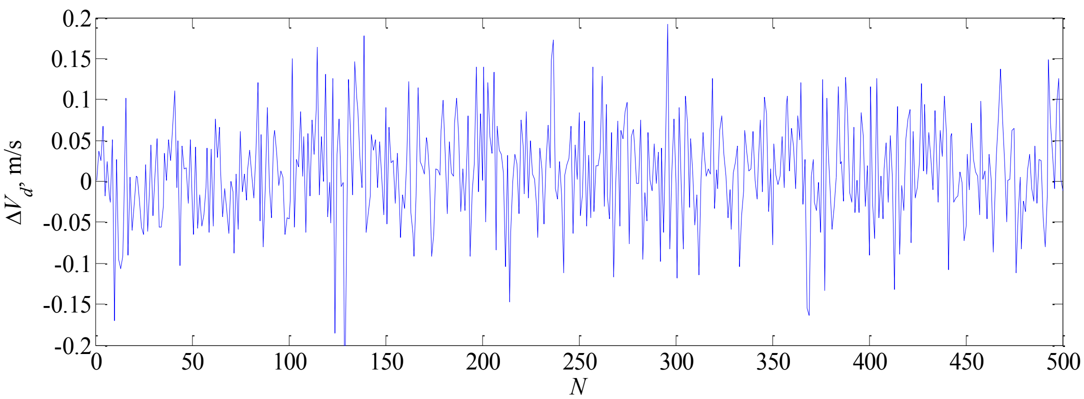

(c)

Figure Ap. 3 Velocity differences in the overlap region, ΔV_d, at points (a) 1, (b) 2 and (c) 3.

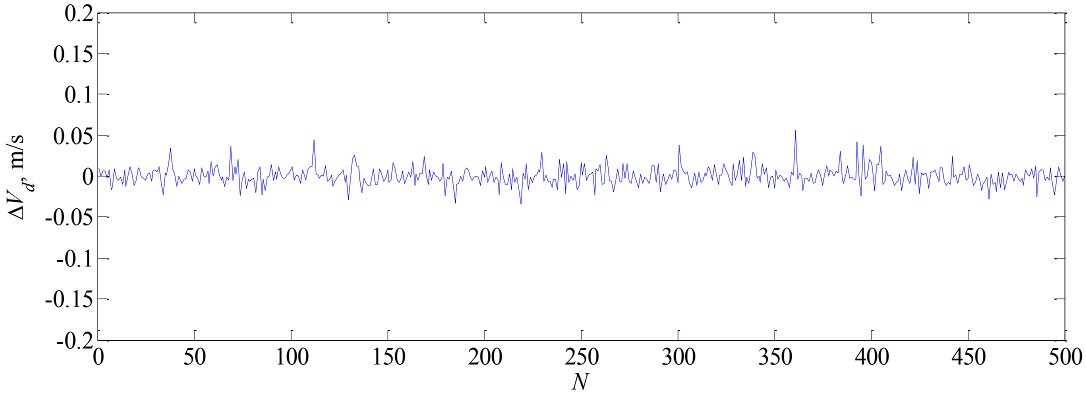

(a)

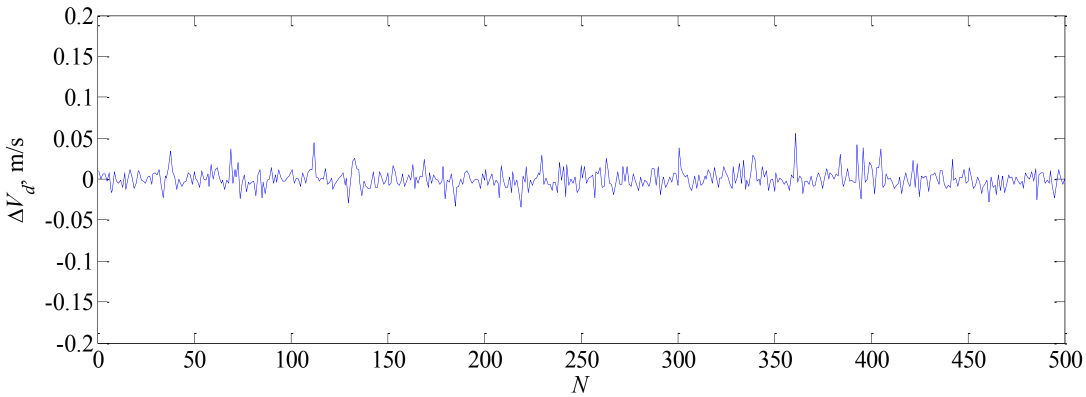

(b)

Figure Ap. 4 Velocity differences in the overlap region, ΔV_d, at points (a) 4, (b) 5.

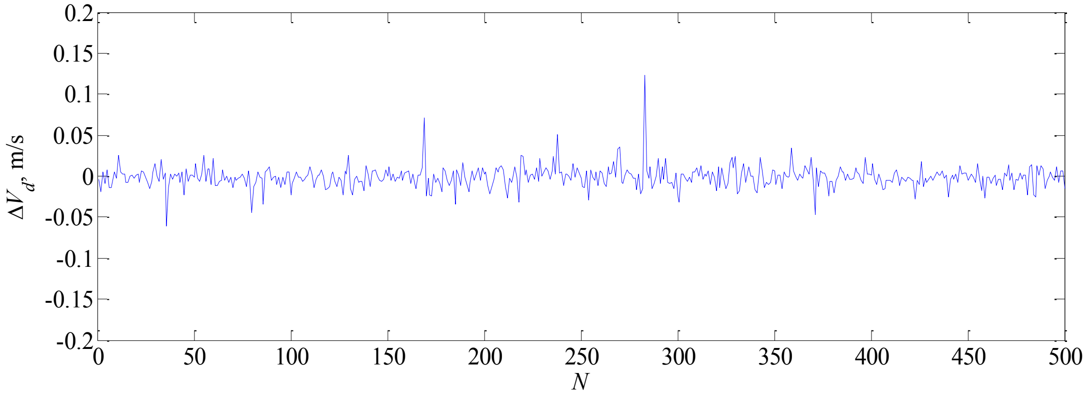

(a)

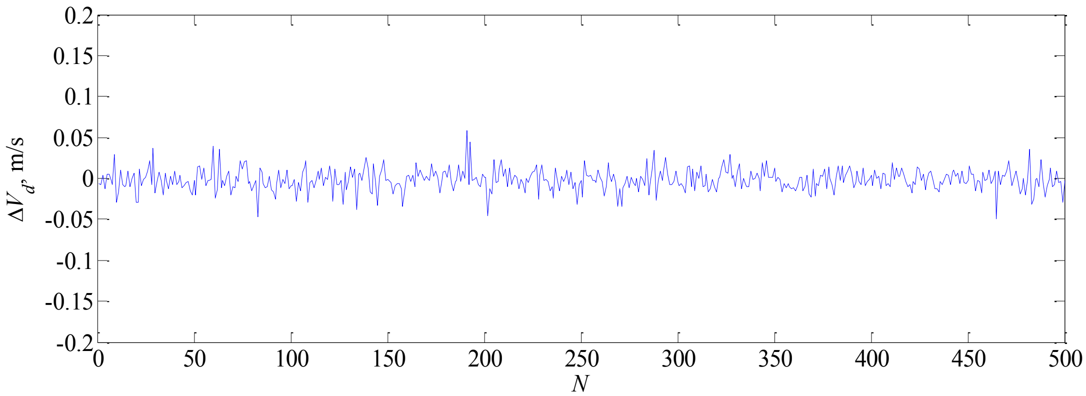

(b)

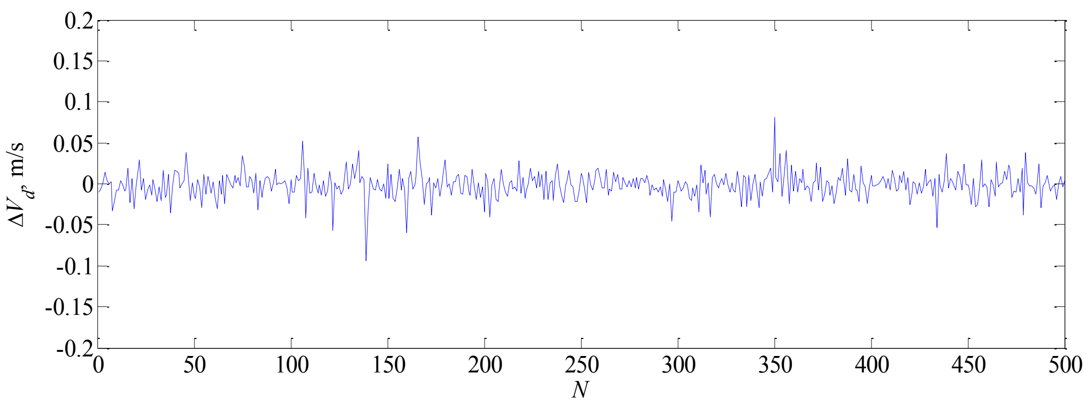

(c)

Figure Ap. 5 Velocity differences in the overlap region, ΔV_d, at points (a) 6, (b) 7, (c) 8.

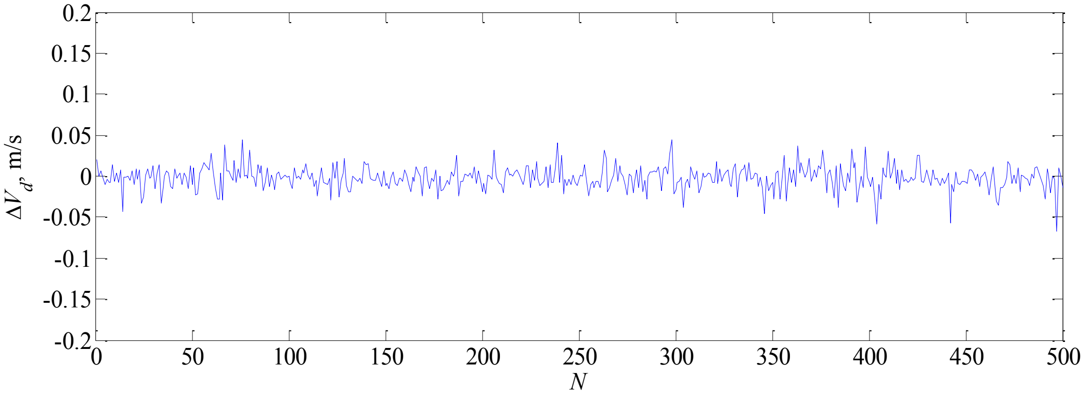

(a)

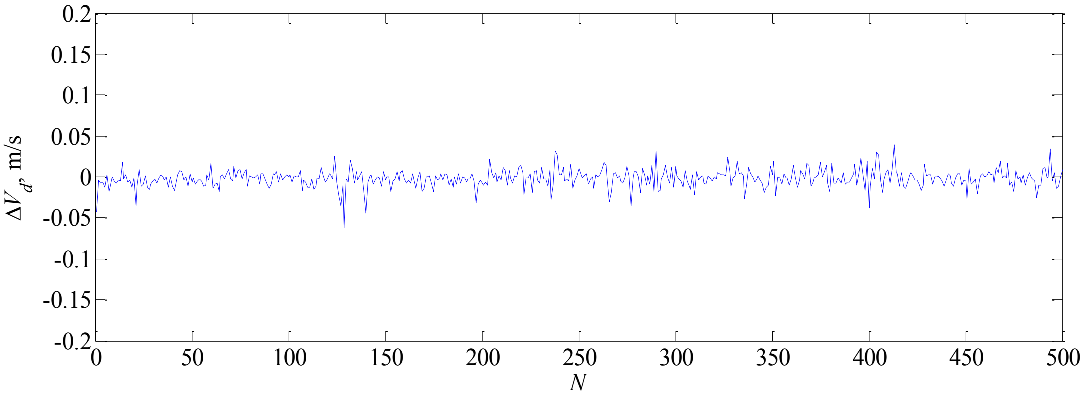

(b)

Figure Ap. 6 Velocity differences in the overlap region, ΔV_d, at points (a) 9 and (b) 10.

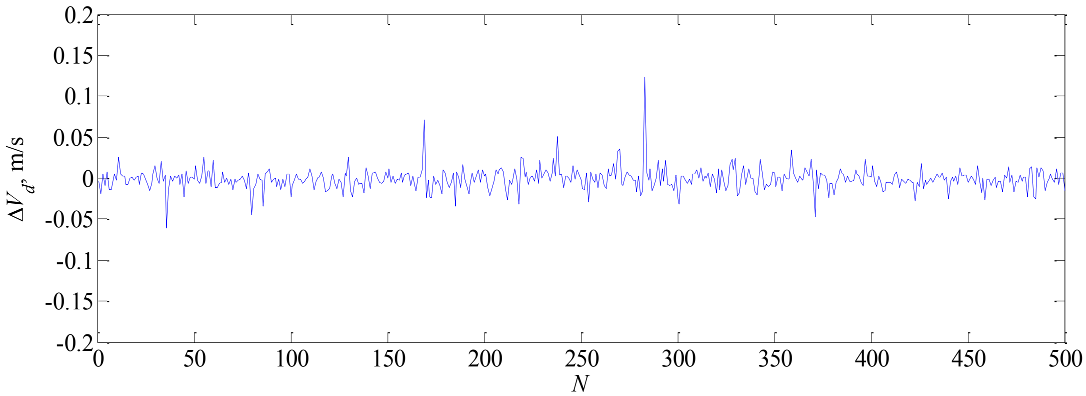

(a)

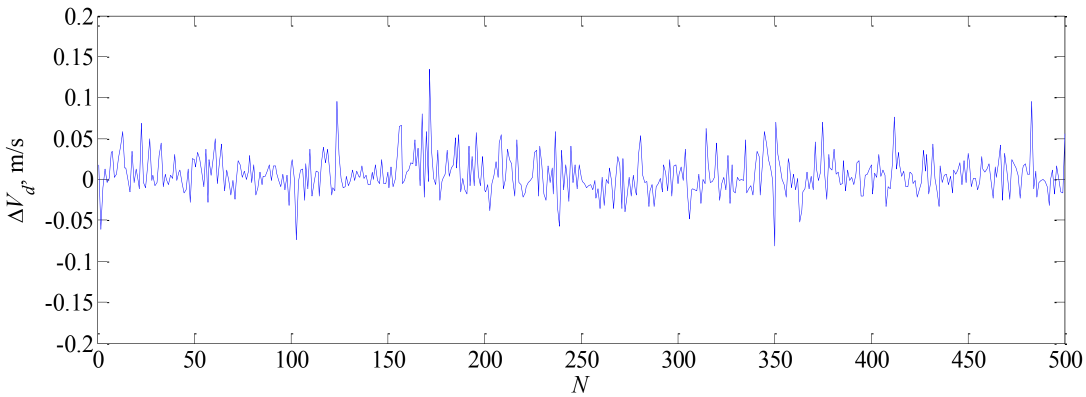

(b)

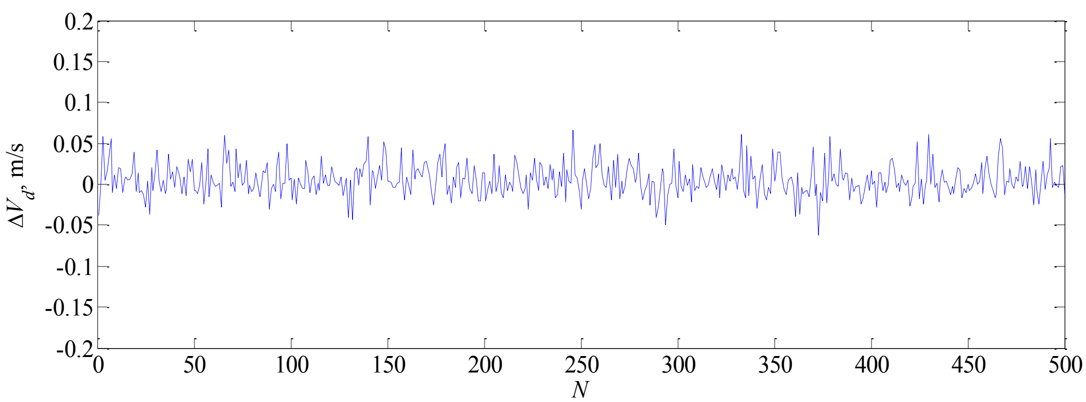

(c)

Figure Ap. 7 Velocity differences in the overlap region, ΔV_d, at points (a) 11, (b) 12 and (c) 13.

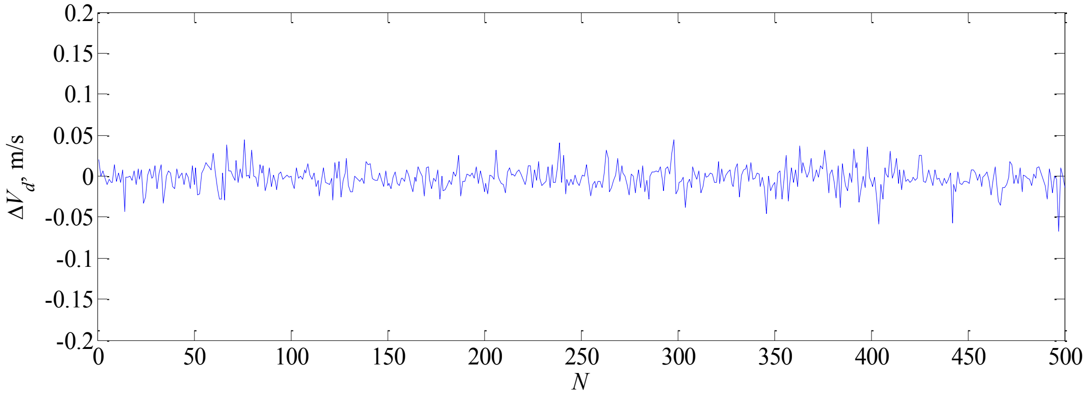

(a)

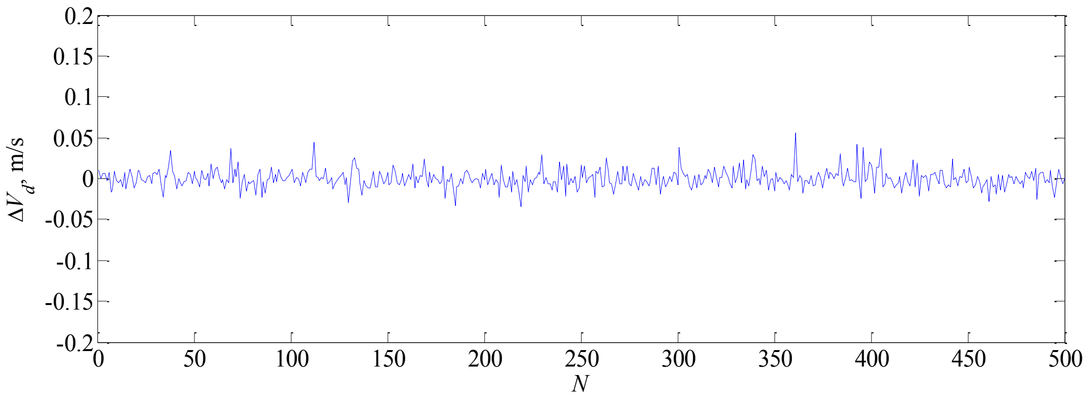

(b)

Figure Ap. 8 Velocity differences in the overlap region, ΔV_d, at points (a) 14 and (b) 15.

Appendix B

The quadrant analysis of instantaneous flow fields captured at $2\Delta t$ before the single-detachment flow fields are plotted in Figure Ap. 9 and Figure Ap. 10 for Y=0.0303H and Y=0.182H respectively.

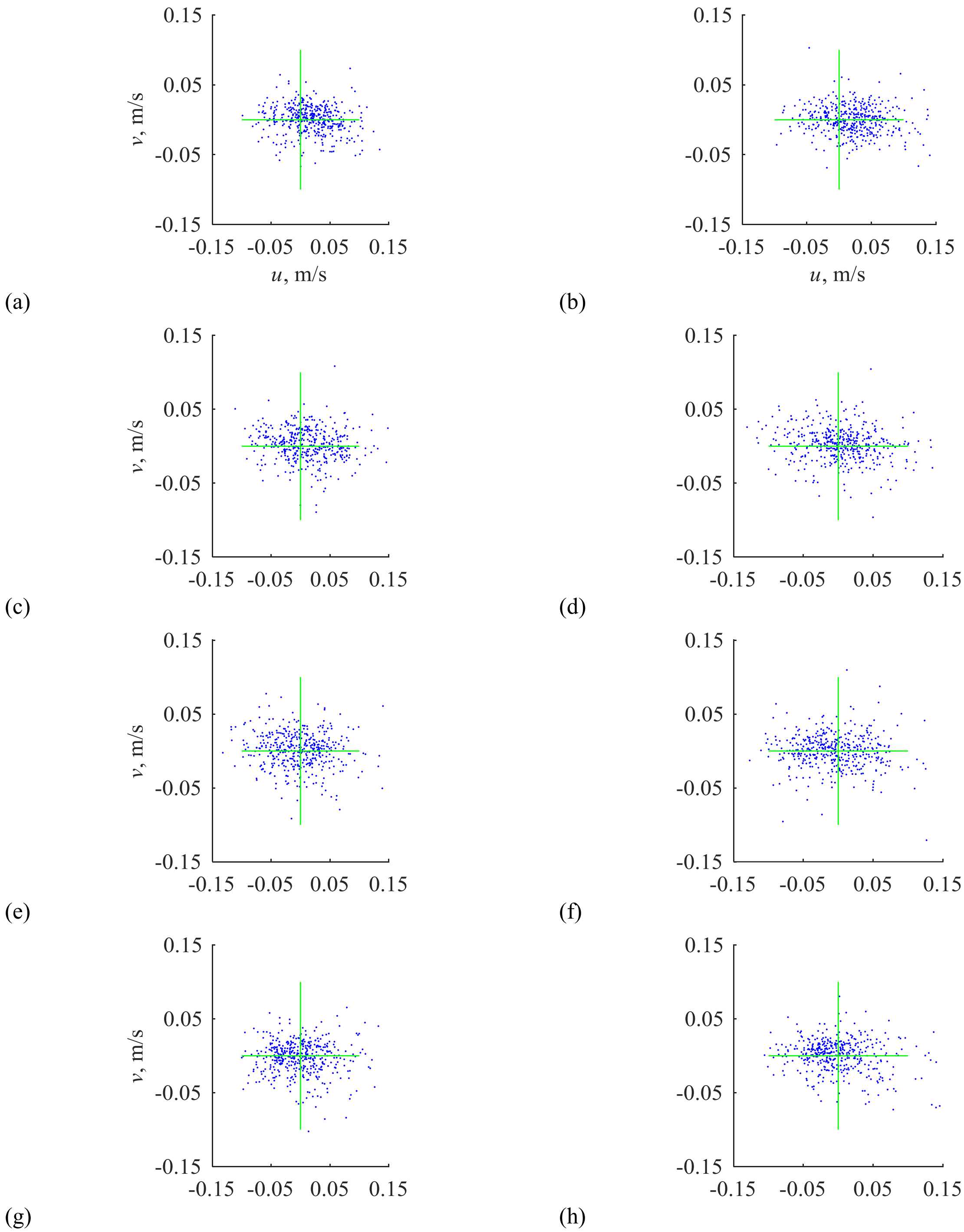

Figure Ap. 9 Quadrant analysis for the flow fields captured at $t_0-2\Delta t$ with respect to single-detachment flow fields at points 1 (a) to 8 (h) located at Y=0.0303H.

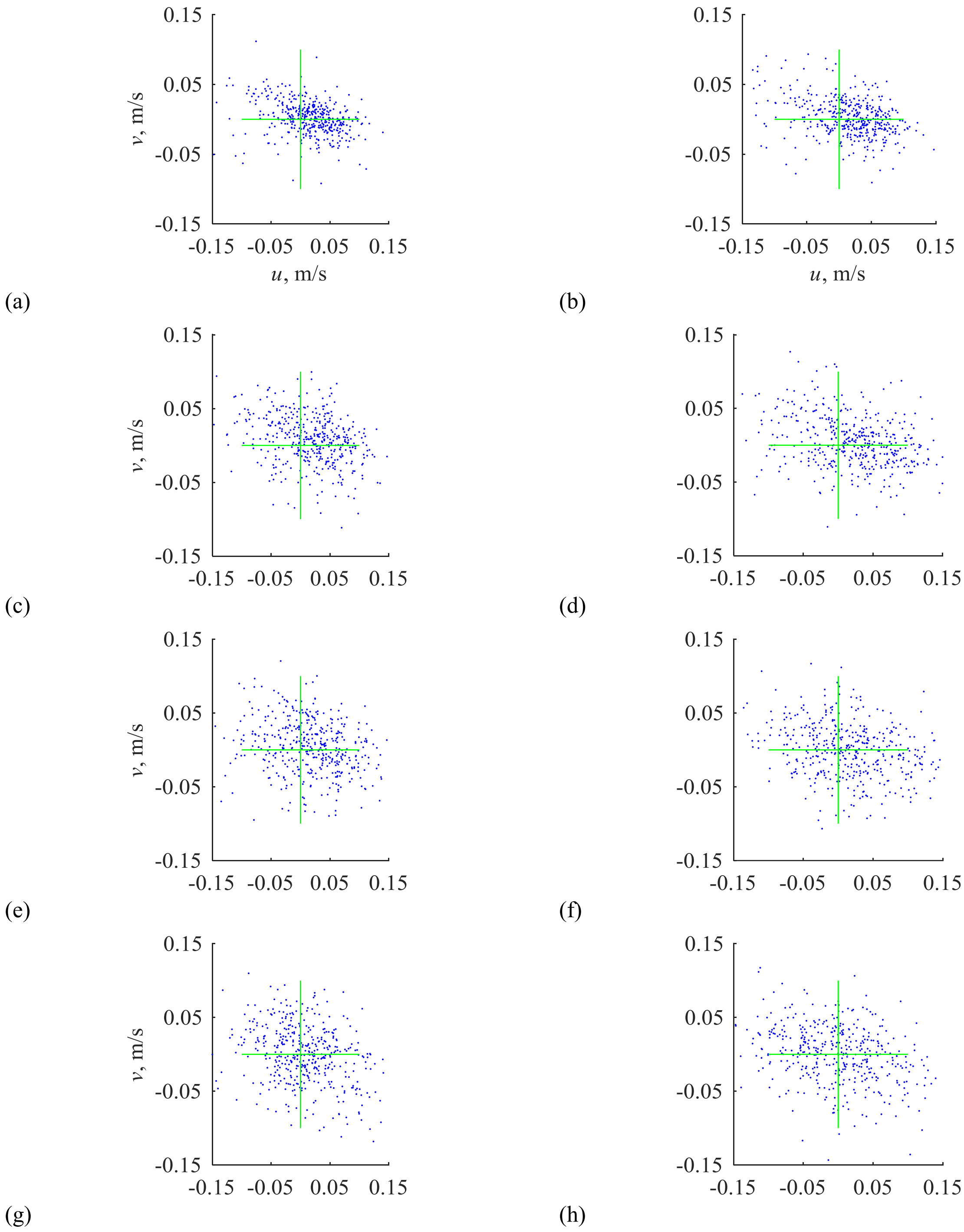

Figure Ap. 10 Quadrant analysis for the flow fields captured at $t_0-2\Delta t$ with respect to single-detachment flow fields at points 9 (a) to 16 (h) located at Y=0.182H.